UNIVERSITY OF CALIFORNIA,
IRVINE

Laser diagnostics for high pressure combustion

DISSERTATION

submitted in partial satisfaction of the requirements
for the degree of

DOCTOR OF PHILOSOPHY

in Mechanical and Aerospace Engineering

by

David Escofet-Martín

Dissertation Committee:
Professor Derek Dunn-Rankin, Chair
Associate Professor Jacob Brouwer
Professor Shaul Mukamel

2017

DEDICATION

To my family, my mom Anna Martín Muro, my father Jordi Escofet Salvador and my brother Miquel Escofet Martín without their support this would not have been possible.

TABLE OF CONTENTS

LIST OF FIGURES

LIST OF TABLES

ACKNOWLEDGMENTS

I would like to express my sincere gratitude to my advisor Professor Derek Dunn-Rankin to provide me with opportunities that would not have been possible in any other environment and I am very thankful for his unconditional trust and support throughout this journey.

I would like to thank Professor Shaul Mukamel for opening my mind in non-linear spectroscopy and being a member of my committee.

I would like to thank Professor Jack Brouwer, Gamero Castaño, and William Sirignano for serving on committees during my degree program.

I would like to thank my labmates Ali Ziaee, Jesse Tinajero, Vinicius Sauer, Jin Dang, Marco Minniti, Navid Saeidi, Claudia Lopez, Michela Vicariotto, Adriana Llado, Andre Nodem, Ferran Marti, Michael Bryant, Valentina Ricchuiti, Jeff Botimer, Jesus Tapia, Laia Torregrosa, and Joan Santacana for interesting discussions and sharing enjoyable times inside and outside the lab. I would also like to thank in particular my labmates and coworkers Rosa Padilla for our experiences during the counterflow experiments, Chaobo Yang for not only being the main contributor for the simulation code used in Chapter 8 and coworker for the experimental results but for the enlightening discussions in non-linear spectroscopy and finally Yu-Chien (Alice) Chien for the experiences during the impinging flame experiments and learnings that will last all my life long.

I would like to thank the visting students that have helped me in this work Pierre Lemarie, Jordan Bibault, Gaetan Crouzy, Gaetan Ruscade, and Alex Torredemer.

I would like to thank the Balsells fellowship and the Keck foundation for providing the monetary support of this work.

And finally, I would like to thank my family for moral support throughout all the journey.

Curriculum Vitae

David Escofet-Martin

Education

2013–2017 **Doctoral degree**, *University of California Irvine*, Irvine, United States of America.
"High pressure laser diagnostics for combustion".

2012–2013 **Master's degree in Mechanical and Aerospace Engineering**, *University of California Irvine*, Irvine, United States of America, 3.87/4.
Fluid Mechanics Major.

2007–2011 **Bachelor's degree in Mechanical Engienering**, *Politechnique University of Catalonia ETSEIAT*, Terrassa, Spain, 7.6/10. Final project "Laser spectroscopy techniques in combustion: 2D OH planar laser induced fluorescence (PLIF), 10/10".

Doctoral thesis

title High pressure laser diagnostics for combustion.

supervisors Derek Dunn-Rankin.

description Laser diagnostics have been a staple for experimental combustion research as a modern tool to evaluate high temperature reacting flow environments and to contribute to the fundamental knowledge needed for improving our current combustion systems in a non-intrusive way; they also represent a key tool for validating computational models. The specific techniques involving OH planar laser induced fluorescence (PLIF), two-line OH PLIF thermometry, two-photon CO and CARS are all demonstrated at atmospheric pressure and high pressure using a non-premixed coflow impinging jet as study flame; the implications and potential challenges of using these diagnostics at high pressure are discussed in detail.

Publications

Refereed publications

- Chien, Y. C., Escofet-Martin, D., & Dunn-Rankin, D. (2016). CO emission from an impinging non-premixed flame. *Combustion and Flame*, 174, 16-24.

Conference Papers full papers, presenter underlined

- Escofet-Martin, D., Chien, Y.C., and Dunn-Rankin, D. (2014) "OH PLIF of an Impinging Flame," *Western States Section/The Combustion Institute Spring Meeting* paper 087DI-0032, California Institute of Technology, Pasadena, CA, March 24–25.
- Escofet-Martin, D., Chien, Y.-C., and Dunn-Rankin, D. (2015) "Two-Photon CO PLIF of Flames near a Quenching Plate," *9th U.S. National Combustion Meeting*, Cincinnati, OH, May 17–20.

7122 Palo Verde Rd – 92617 Irvine CA
+1 949-331-8783 • FAX • *descofet@uci.edu*

- Chien, Y.-C., Escofet-Martin, D., and Dunn-Rankin, D. (2015) "CO Emission from an Impinging Non- Premixed Flame under the Influence of an Electric Field," *9th U.S. National Combustion Meeting*, Cincinnati, OH, May 17–20.
- Escofet-Martin, D., Chien, Y.-C., and Dunn-Rankin, D. (2015) "Two-Line OH PLIF Temperature Measurements of Flames Near a Quenching Plate," *25th International Colloquium on the Dynamics of Explosions and Reactive Systems*, Leeds University, England, August 2–7.
- Chien, Y.-C., Escofet-Martin, D., and Dunn-Rankin, D. (2015) "Non-Premixed Impinging Flames and CO Release under the Influence of an Electric Field," *25th International Colloquium on the Dynamics of Explosions and Reactive Systems*, Leeds University, England, August 2–7.

Conference Papers-posters, presenter underlined

- Chien, Y.-C., Escofet-Martin, D., and Dunn-Rankin, D. (2014) "Electric Field Effects on CO Emission from Non-Premixed Quenching Flames," Work-in-Progress Poster W1P011, *35th International Combustion Symposium*, San Francisco, CA, August 3–8.
- Escofet-Martin, D., Botimer, J., Dunn-Rankin, D., Taborek, P., and Karnani, S. (2014) "Laser Diagnostics on Methane Hydrates," Work-in-Progress Poster W4P029, *35th International Combustion Symposium*, San Francisco, CA, August 3–8.
- Chien, Y.C., Escofet-Martin, D., and Dunn-Rankin, D. (2015) "Electric field effects on CO emission from Non-Premixed Quenching Flames," Poster at the *Gordon Research Conference on Fundamental of Laser Diagnostics in Combustion*, Waterville Valley, NH, August 914.
- Escofet-Martin, D., Crouzy, G., and Dunn-Rankin, D. (2015) "High pressure broadband N2 CARS in a calibration vessel," Poster at the *Gordon Research Conference on Fundamental of Laser Diagnostics in Combustion*, Waterville Valley, NH, August 914.
- Escofet-Martin, D., Chien, Y.C., Dunn-Rankin, D.(2016) "Two-photon CO fluorescence thermometry and concentration" Work-in-Progress Poster W4P046, *36th International CombustionSymposium*, Seoul, Korea, August 1–5.

Acknowledgements in Refereed Publications

- Botimer, J., Dunn-Rankin, D., and Taborek, P. (2015) "Evidence for Immobile Transitional State of Water in Methane Clathrate Hydrates Grown from Surfactant Solutions," *Chemical Engineering Science, 142, 89–96.*
- Sauer, V.M. and Dunn-Rankin, D. (2016) "Impinging Nonpremixed Coflow Methane-Air Flames with Unity Lewis Number," 36th International Combustion Symposium, Seoul, Korea, July 31–August 5. Accepted for publication in the *Proceedings of the Combustion Institute*, 35, June.

Summer Schools

2015 **V school of combustion**, Sao Paulo, Brasil.

2014 **5th edition of Princeton-CEFRC-CI Summer School on Combustion**, *Princeton University*, Princeton, United States of America.

2013 **4th edition of Princeton-CEFRC-CI Summer School on Combustion**, *Princeton University*, Princeton, United States of America.

7122 Palo Verde Rd – 92617 Irvine CA
• ☎ *+1 949-331-8783* • FAX • ✉ *descofet@uci.edu*

Experience

2016 **Teaching assistant**, *University of California Irvine*, Irvine, United States of America.
Fall quarter MAE 107: Fluid thermal science laboratory.

2015 **Teaching assistant**, *University of California Irvine*, Irvine, United States of America.
Fall quarter MAE 107: Fluid thermal science laboratory.

2011 **Research Scholar**, *University of California Irvine*, Irvine, United States of America.
Senior Project.

2010 **Teaching assistant**, *Politechnique University of Catalonia*, Terrassa, Spain.
Calculus I.

Summers 2008 and 2009 **Internship as an Assistant Engineer**, *Hospital General of Catalonia*, Sant Cugat, Spain.
Control of the facilities of the Hospital.

Fellowships

2014 **Balsells fellowship**, *Catalonian Goverment*.

2013 **Balsells fellowship**, *Catalonian Goverment*.

2012 **Balsells fellowship**, *Catalonian Goverment*.

2010 **Enginycat fellowship**, *Catalonian Goverment*.

Languages

Spanish Native.

Catalan Native.

English Near-native.

Interests

Chess Catalonian master chess player, FIDE international rating: 2195.

7122 Palo Verde Rd – 92617 Irvine CA
• ☎ *+1 949-331-8783* • FAX • ✉ *descofet@uci.edu*

ABSTRACT OF THE DISSERTATION

Laser diagnostics for high pressure combustion

By

David Escofet-Martín

Doctor of Philosophy in Mechanical and Aerospace Engineering

University of California, Irvine, 2017

Professor Derek Dunn-Rankin, Chair, Chair

Laser diagnostics have been a staple for experimental combustion research as a modern tool to evaluate high temperature reacting flow environments and to contribute to the fundamental knowledge needed for improving our current combustion systems in a non-intrusive way; they also represent an essential tool for validating computational models. High pressure diagnostics are of particular importance due to the fact that the majority of practical combustion systems operate at high pressure, involving increased challenges in the measurements. The current work examines a variety of linear and non-linear light/matter interaction processes (Raman, fluorescence, and coherent anti-Stokes Raman spectroscopy or CARS) with the goal of measuring the temperature, pressure, and spatial distribution of important reacting flow species. The specific techniques involving OH planar laser induced fluorescence (PLIF), two-line OH PLIF thermometry, two-photon CO PLIF, nanosecond vibrational CARS and hybrid femtosecond/picosecond rotational CARS are all demonstrated at atmospheric pressure using a non-premixed coflow impinging jet as a study flame and examined in detail under high pressure conditions (up to 12 bar) as a coflow flame and in a calibration high pressure vessel; the implications of pressure are discussed in detail in the linear and non-linear techniques. The high pressure experimental data set shows soot laser induced incandescence (LII) as a source of interference for high pressure LIF in non-premixed flames, good agreement with 3 different chemical mechanisms, in particular at high pressure, between an

OpenFOAM simulated fluorescence and the experimental pressure dependent data regarding both the spatial distribution of the OH molecule and the overall number of OH molecules interacting with the excitation source. Chirp is identified as a critical parameter when using a second harmonic bandwidth compressor in the hybrid fs/ps CARS configuration, and the chirped CARS signal depends strongly on probe delay in N_2 experiments. High quality high pressure data can be achieved once chirp influence has been quantified accurately. Together the combination of diagnostics studied provide insights into high pressure laser diagnostics challenges beyond what is currently available.

Chapter 1

Introduction

Carbon fuels remain as the number one US energy source, comprising $> 80\%$ of the energy consumption [1]. Despite the various challenges that arise from the use of carbon based fuels: such as long term sustainability, air quality, climate change, and dependent market economies, they remain as the primary source of energy, and predictions show that they will continue to be dominant in the upcoming decades [2]. Gas turbines, automobiles and jet aircraft all have one thing in common, high pressure combustion of carbon-based fuels in the range of $2 - 100$ *bar* because thermodynamic efficiency and specific energy production both are enhanced under high pressure conditions. These attributes produce systems with improved fuel efficiency, reduced emissions of combustion generated pollutants, including CO_2, which is a significant contributor to global warming. Despite the modern trend towards higher pressure, the bulk of combustion research is made at atmospheric pressure conditions where experimental conditions can be controlled more easily, and data analysis can be obtained more reliably, although extrapolating atmospheric pressure results for higher pressure conditions could produce prediction errors. In addition, high pressure experimental data is very much needed, in particular, to validate models, which due to experimental costs of high pressure experiments are a focus of attention when developing new high pressure technology.

Optical diagnostics in general and laser diagnostics, in particular, are some of the tools that combustion researchers have used to understand the intricacies of combustion processes. Laser diagnostics, in particular, provide for specific applications unmatched spatial resolution, time resolution, and non-intrusiveness of the system studied; moreover, laser diagnostics in some situations, such as harsh environments, represent the only way to probe those systems. As for any technology, lasers have advanced notably in the last decade, providing researchers with new tools that allow access to experimental data that was previously not accessible, in particular regarding high frequency experiments and nonlinear techniques. Laser diagnostics for combustion is a concept that aims to combine the knowledge of multiple disciplines (chemistry, fluid mechanics, spectroscopy and laser technology) to extract useful information from combustion systems.

Fundamental combustion research uses simplified burner configurations to isolate particular problems and study them. For this purpose counterflow burners, shock tube experiments, flat flame burners and a long series of well thought out configurations have been developed. The LFA (Laser Flames & Aerosols) research group has been recently focusing on the coflow configuration. The coflow configuration presents one key advantage at high pressure conditions: the coflow flame is dominated by mass diffusion, which allows it to be operated at high pressures with spatial scales and heat release that don't scale with pressure.

The goal of this work is to provide diagnostics insights, in challenging configurations and conditions. The first part of the dissertation focuses upon the experimental challenges of laser diagnostics near to a surface thereby providing valuable insights concerning emissions and flame behavior for flame surface interactions.

Chapter 2 describes the main experimental apparatus that is used in the upcoming chapters.

Chapter 3 uses fluorescence, an absorption based method to study the temperature changes when the coflow burner interacts with a surface. Temperature is the most important pa-

rameter when studying combustion due to the high dependence of chemical processes on temperature. In this particular case the large temperature gradients in a small scale, characteristic of non-premixed diffusion flames represent the perfect scenario where spatially two dimensional resolved fluorescence thermometry can offer results that no other technique could provide. Furthermore OH is chosen as the interrogated molecule due to its important role in combustion chemistry.

Chapter 4 uses a two-photon fluorescence process, to study a molecule of particular interest in flame-wall interaction, CO is a significant combustion pollutant which sometimes can be utilized as a sign of incomplete oxidation of the carbon based fuel. The spatial scale for a boundary layer of the buoyant driven combustion products that interact with a horizontal cold surface is on the order of one mm [3], the combination of a small scale configuration and a complicated geometry produces a challenging configuration.

The second part of the dissertation focuses on high pressure effects in two of the most used techniques in combustion research: (1) OH fluorescence is the light/matter interaction from one of the most studied intermediate radicals in combustion, and (2) ramifications of coherent anti-Stokes Raman spectroscopy (CARS), both nanosecond N_2 broadband CARS, and the more novel rotational hybrid fs/ps CARS. Each has different behavior with collisions and pressure, from highly reduced signal in the fluorescence process to the collision-free or nearly pressure independent hybrid fs/ps CARS measurements with a small probe delay. The fluorescence measurements are carried out using the same UCI coflow burner, and the CARS measurements are performed in a high pressure calibration cell. One of the most important aspects for combustion is model validation, and this is particularly important at high pressure due to the elevated costs of high pressure experiments. A quantitative comparison between the experimental results and a numerical CFD simulation with OpenFOAM is performed using a very detailed spectroscopic model.

Chapter 5 shows OH fluorescence measurements for a particular coflow mass flow rate. The

modeling of some key players in high pressure fluorescence are described here: temperature dependence, overlap integral with Doppler and pressure broadening, and quenching effects. This set of data provides an experimental dataset that can be used to validate different transport and chemical models.

Chapter 6 describes the simulation details of experimental conditions from Chapter 5, the fluorescence model with three different reference chemical mechanisms (GRI, DRM and PAH [4]). The effects of the individual modeling corrections are calculated for each mechanism providing a quantitative comparison of the high pressure results for each pressure and mechanism. This information can be used to understand the relative effects that pressure has on the fluorescence signal. Furthermore, these characteristic values can be extrapolated to similar non-premixed systems.

Chapter 7 uses the commonly used broadband N_2 CARS setup in combustion, and the effects of pressure up to 10 *bar* in a calibration cell are discussed.

Chapter 8 uses a more novel hybrid fs/ps CARS (HCARS) approach and studies the effect of chirp through a semi classical model for HCARS signal simulation, and in particular the chirp characteristics of an essential molecule for combustion diagnostics such as N_2. Temperature and pressure measurements are studied both in the time domain and the frequency domain for different quantified chirp values.

Chapter 2

Experimental apparatus

The experimental apparatus description focuses on the modifications for high pressure combustion, and the introduction of 2 high pressure chambers, one of new design for combustion and one for high pressure experimentation and calibration [5]. The UCI coflow burner is modified for stability reasons at high pressure conditions, the calibration high pressure chamber is used for the CARS measurements, and a new high pressure facility is introduced to be used as the environment of the UCI coflow burner.

2.1 UCI coflow burner

The UCI coflow burner seen in Figure 2.1 has been utilized in the LFA group for many years [6, 7, 8]. The coflow burner is 14 cm tall with an outer $\varnothing$ 4 cm; the inner fuel tube is $\varnothing$ 2 mm with a coflow outer diameter of $\varnothing$ 25 mm. The Yale Laser Diagnostics Center provided the plans for this burner [9, 10]. The burner was redesigned for the use in high pressure conditions with three main modifications.

- The first is to accommodate a stainless steel metallic porous filter, both in the air and the fuel tubes. The porous filter has several purposes, to provide a better uniform profile and to induce a small pressure drop in the tip of the burner. This pressure drop reduces flow rate fluctuations in the flame (in between the mass flow meter and the needle valve there is a significant gas volume) since any small pressure oscillation from the chamber would propagate upstream and induce oscillations near the tip of the burner.

- The second change is to raise the tip of the metallic methane tube to facilitate the access of laser diagnostics in the burner without excessive light scattering from the burner surface.

- The third change is to add an o-ring between the fuel and the air chamber within the burner to prevent leaking.

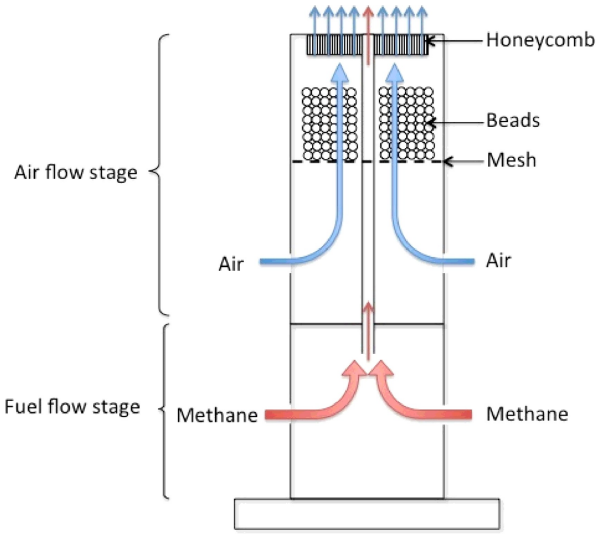

Figure 2.1: Burner diagram with no modifications.

The burner without modifications is used in Chapters 3 and 4 see Figure 2.1, the modified burner is used in Chapters 5 and 6.

2.2 High pressure calibration vessel

The main apparatus for testing and calibrating the CARS equipment is inherited from [5]; the initial design goal for the chamber was testing and developing high pressure nanosecond CARS. The chamber is rated for up to 104 bar and 478 K. The chamber is made of stainless steel and has a cylindrical shape with an outer $\varnothing$ 15 cm and a height of 16 cm. The gas compartment of the chamber has a $\varnothing$ 4 cm with an approximated length of 12 cm. The gas volume is 0.15 dm^3 and has optical access across 180°, the windows are made of quartz with a cylindrical shape ($\varnothing$ 4 cm by 2.5 cm). The chamber is designed to hold six cylindrical heaters distributed symmetrically around the chamber for temperature control. Each of the resistors has a total resistance of 17 Ω with a power of 850 $Watts$. In the current use, the number of heaters is reduced to four because they provide sufficient heat for the conditions used. The chamber temperature is controlled using 2 type K thermocouples, one to monitor the stainless steel temperature of the chamber, and one placed in the geometrical center of the gas compartment to measure the gas temperature. The pressure is monitored with a pressure transducer (Omega PX01C-2KVG), and the chamber is equipped with a high pressure relief valve, to prevent the chamber pressure to rise over 104 bar.

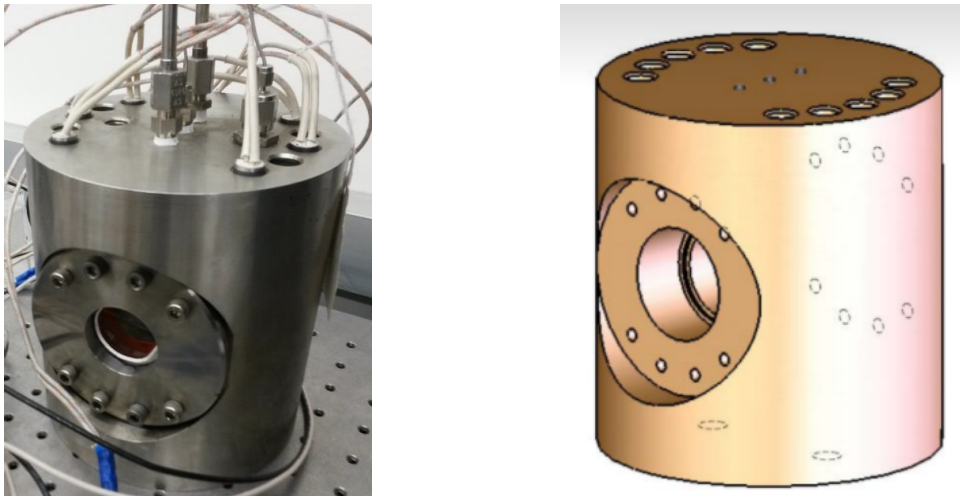

(a) Image. (b) CAD.

Figure 2.2: Calibration vessel ($\varnothing$ 15 cm $\times$ 16 cm).

The temperature control of the chamber is accomplished through a PD controller in Labview and a NI-DAQ board. The control is based on both thermocouples, the chamber pressure, the Van der Waals gas Law, and extensive calibration to account for the thermal inertia of the system. More detailed information on the temperature control can be found in [11, 12]. This chamber will be used in the experiments described in Chapters 7 and 8.

2.3 High pressure burning system

The high pressure system diagram can be seen in Figure 2.3. The main component is the high pressure chamber made of SS304 and designed to withstand over 200 bars of pressure. The chamber was built through a collaboration of Sunny Karnani and Royal Welding; see Figure 2.4. The most innovative design compared to similar high pressure chambers [13, 14] is the window mounting, allowing easier access to the inner chamber compartment. The inner dimensions of the chamber are approximately $\varnothing\ 0.26 \times 0.33\ m$ with a total of 17.5 dm^3 internal volume; the outer dimensions are $\varnothing\ 0.33 \times 0.51\ m$. The chamber is equipped with four sapphire windows that allow optical access to the chamber at angles of 90°, with very good transmissivity in the UV, these windows are placed in 4 view ports with a $\varnothing$ 7.6 cm.

The flow delivery system is inspired by [14, 15] and consists of 3 different lines, air, methane, and nitrogen. Each line is equipped with a regulator, flow meter, and needle valve. Connected to the pressure chamber a dome loaded back pressure regulator controls the chamber pressure. The dome loaded line is controlled with nitrogen as inert gas

Traditional rotameters are not suitable to operate on a broad range of pressures; because of dynamic range problems, the system is designed to run at a constant mass flow rate through a range of pressure (to keep the coflow flame at constant flame height). The rotameter style flow meter measurements are based on drag, and when keeping the mass flow rate

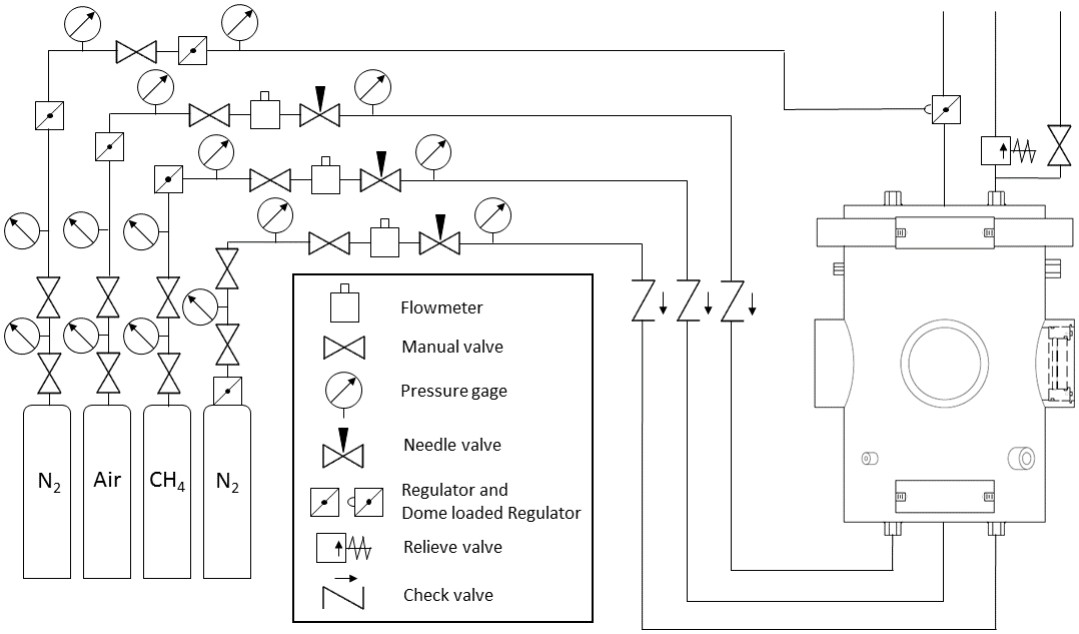

Figure 2.3: High pressure chamber diagram.

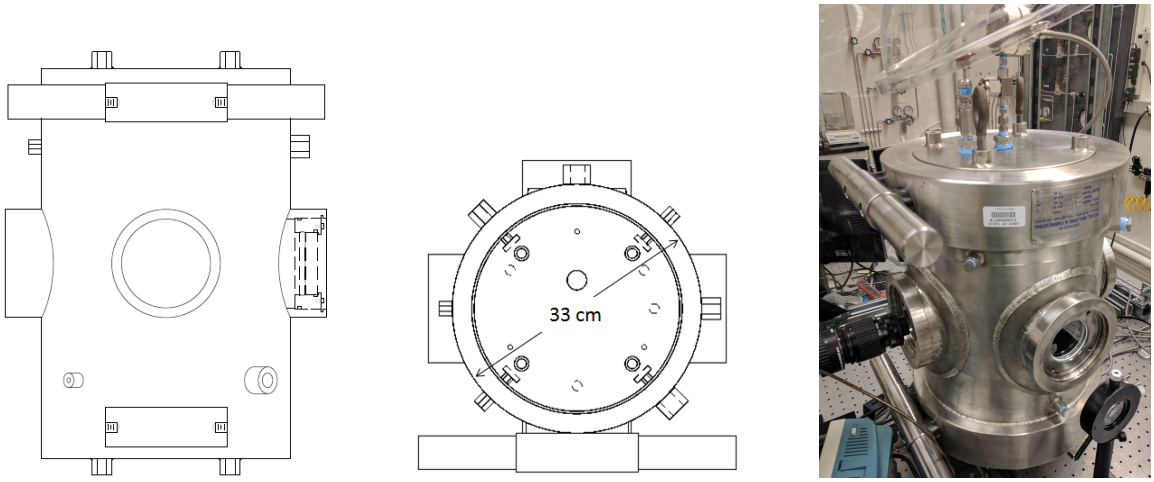

(a) Front view. (b) Top view. (c) Image.

Figure 2.4: High pressure chamber.

constant the drag has a pressure dependence, creating practical dynamic range problems. On the other hand, digital thermal mass flow meters are based on a ratio two temperature measurements, which have a dependence on convection and conduction which is independent of pressure. The flow meters used are from Bronkhorst, model (F-121M-AAD-22-V) and despite being calibrated at 100 *bars* it is necessary to recalibrate them due to real gas effects when they are used at an intermediate pressure; the calibration can be found in Appendix

A. Figure 2.5 shows the chamber and the control panel separated by a double layer of clear polycarbonate sheet (.5" × 48" × 48") that is mounted on the optical table, to protect the operator, while providing visual access to the experimental area. This chamber will be used for the measurements described in Chapter 5.

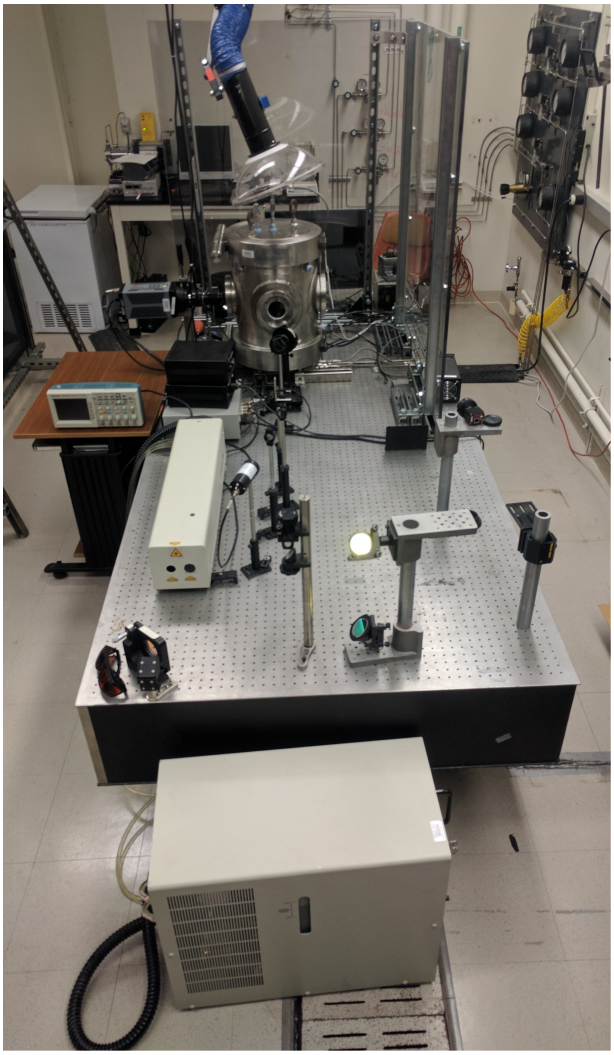

Figure 2.5: High pressure experiment layout.

Chapter 3

Two-line OH PLIF thermometry

Most of the results of this Chapter can be seen in [16] but they represent a crucial part of this dissertation work because OH and temperature are key quantities to understand diffusion flames. Several laser non-intrusive techniques are available for making measurements of these properties: among them are Rayleigh or Raman scattering, fluorescence based techniques, and CARS. Laser induced fluorescence can be used for flame thermometry as long as the fluorescent molecule can be excited through two different transitions. Fluorescence stands out as a valuable method because of the high signal-to-noise (SNR) ratio achievable through gating of the signals both in the time domain and frequency domain. Fortunately, some suitable fluorescing species are present naturally in flame conditions, such as NO and OH, although using them can be of limited applicability due to low concentration in some important areas of the flame. Unfortunately, seeding the flow with tracers, such as NO and Indium [17, 18], can be a difficult task, and it has an impact in the flame chemistry. Hence, this experiment focuses on two-line OH thermometry due to excellent signals and 2D imaging capabilities with high spatial resolution. As mentioned before, seeding is not necessary since OH is naturally present in the flame, particularly in the important high temperature regions. This chapter report on 2D temperature measurements of an atmospheric pressure

non-premixed coflow burner under the special conditions where the flame is impinging on a relatively cool wall that produces a quenching interaction.

3.1 Background

3.1.1 2-level model

To develop a basic understanding of the LIF process [19], it is helpful to build a 2-level energy model. A 2-level model is far from what occurs in a molecule, where many levels coexist, but the simplification helps describe the basic behavior of the light/molecule interaction when LIF is used. Explained very simply, as shown in Figure 3.1, the process starts with an absorption process that excites the molecules to change its electronic state.

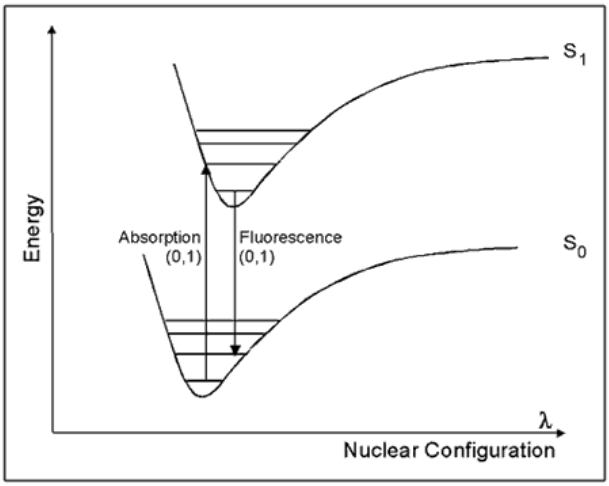

Figure 3.1: Example of fluorescence configuration.

N_1 and N_2 are the population in the states (1-ground state 2-excited state), Q is quenching, P is the predissociation rate constant, A stands for the spontaneous emission, b stands for

induced absorption or emission, and W_{21} is the photo-ionization rate constant.

$$\frac{\partial}{\partial t}N_1(t) = -N_1 b_{12} + N_2\left(b_{21} + A_{21} + Q_{21}\right) \tag{3.1}$$

$$\frac{\partial}{\partial t}N_2(t) = N_1 b_{12} - N_2\left(b_{21} + A_{21} + Q_{21} + P + W_{21}\right) \tag{3.2}$$

Assuming that we are working in a laser power regime where there is no predissociation and no photo-ionization:

$$P = 0 \tag{3.3}$$

$$W_{2i} = 0 \tag{3.4}$$

With this hypothesis and with the 2-level case, we further assume:

$$\frac{\partial}{\partial t}N_1(t) + \frac{\partial}{\partial t}N_2(t) = 0 \tag{3.5}$$

$$N_1(t) + N_2(t) = N_t \tag{3.6}$$

Solving the differential equation, and assuming that the population in the excited state is 0 at $t = 0$:

$$N_2(0) = 0 \tag{3.7}$$

$$\frac{\partial}{\partial t}N_2(t) = (N_t - N_2(t))b_{12} + A_{12} + Q_{12} \tag{3.8}$$

$$N_2(t) = \frac{b_{21}N_t}{b_{12} + b_{21} + A_{21} + Q_{21}} - \frac{b_{21}N_t \exp(-(b_{12} + b_{21} + A_{21} + Q_{21})t)}{b_{12} + b_{21} + A_{21} + Q_{21}} \tag{3.9}$$

The fluorescence signal is proportional to the collection efficiency of the optics, to N_2 and the spontaneous emission from the excited state to the ground state. Assuming a steady

state solution.

$$b_{ij} = \frac{(B_{ij} I_v)}{c} \tag{3.10}$$

$$I_{vsat} = \frac{(A_{21} + Q_{21})c}{B_{12} + B_{21}} \tag{3.11}$$

$$F = hvN_2 A_{21} \frac{\Omega}{4\pi} lAN_t \frac{B_{12}}{B_{21} + B_{12}} \frac{1}{1 + \frac{I^v_{sat}}{I_v}} \tag{3.12}$$

Where h is Planck's constant; v is the frequency of the emitted fluorescence; Ω is the collection solid angle; A is the focal area of the laser beam, and l is the axial extent of the beam from where the fluorescence is observed. Finally, the fluorescence signal is proportional to the number of molecules that are in the excited band, and solving for the internal energy distribution in any molecule allows to solve for the temperature of the molecules (assuming they are in thermal equilibrium and so the population in the different energy states are Boltzmann distributed).

Assuming linear regime $I_v \ll I^v_{sat}$

$$F = \frac{hv}{c} \frac{\Omega}{4\pi} lAN_t B_{12} I_v \frac{A_{21}}{A_{21} + Q_{21}} \tag{3.13}$$

It is possible to generalize equation 3.13 from a 2-level model to a more general case, by using the concept of quantum fluorescent yield $\Phi(T, J') = \frac{A_{21}}{A_{21}+Q_{21}}$ which represents the number of fluorescent molecules from the ones that went to the excited state. Furthermore:

$$I_v = I_l G \tag{3.14}$$

$$\eta = \frac{hv}{c} \frac{\Omega}{4\pi} lA \tag{3.15}$$

$$F = \eta I_l G(T, P) N_t(T) B_{12} \Phi(T, J') \tag{3.16}$$

I_l is the laser intensity, G is the overlap integral effects, η comprises several constants including collection efficiency, $N_t(T)$ is the population of the ground state and B_{12} is the stimulated

emission Einstein coefficient.

3.1.2 OH thermometry

The basis for two-line OH temperature PLIF has been described in the past [19, 20, 21], and only a brief description is given here. Starting from equation 3.16, and assuming equilibrium for the OH molecule $N_t \propto N(2J''+1)\exp\left(\frac{-E}{kT}\right)$. The linear LIF signal F is a function of:

$$F \propto \eta I N(2J''+1)\exp\left(\frac{-E}{kT}\right) BG(T,P)\Phi(T,J') \tag{3.17}$$

Where J'' is the rotational quantum number of the excited ground state and J' is the rotational quantum number of the excited upper electronic state. Assuming equal collection efficiencies due to using the same camera, camera filter and the same laser setup for two different transitions (1 and 2), we can obtain:

$$\frac{F_1}{F_2} = \frac{I_1}{I_2}\frac{(2J_1''+1)}{(2J_2''+1)}\exp\left(\frac{-(E_1-E_2)}{kT}\right)\frac{B_1}{B_2}\frac{G_1(T,P)}{G_2(T,P)}\frac{\Phi(T,J')}{\Phi(T,J')} \tag{3.18}$$

The ratio $\frac{F_1}{F_2}$ at every pixel of the camera is a function of several constants, temperature, laser intensity, both overlap integrals, and the ratio of both quantum fluorescent yields. The spectral overlap between laser profile and absorption line profile is assumed to be the same for both transitions, which is a source of a small systematic error, even though the laser profile is very similar for both transitions. Since we are working with the same laser setup in a narrow range of wavelength, Doppler and collisional effects depend on the rotational quantum number, but in the calculations, we assume that line broadening for the two transitions is similar. This assumption is not a significant source of error, and when necessary it is one of the easiest assumptions to relax to improve the measurements using a theoretical model to adjust the change in spectral absorption profile. The quantum fluorescence yield ratio is hard to determine because of the complex behavior of the collisions and energy exchange

through vibrational and rotational energy transfer (VET and RET) in the non-equilibrium upper electronic state. From a theoretical standpoint, the best approach to this problem is using two transitions that share a common upper state ($J_1' = J_2'$) [22]. In that way, the ratio of fluorescence yield would be unity. Unfortunately, this ideal situation is not possible because of the exponential dependence and the energy difference in the ground state (for the OH molecule), which makes this energy difference so small that the sensitivity of the temperature measurement becomes very low, reducing the signal to noise ratio of the measurement dramatically. The most common technique for finding the ratio is to do so experimentally by using an alternative calibration temperature measurement for a certain position of the flame and then using that measurement to calculate this ratio [23]. This last method has not been employed in this case because of the spatial resolution of the alternative method (e.g., thermocouple) would be far worse than the one offered from the OH two-line PLIF, compromising the calibration measurement due to averaging and the high gradients present in the non-premixed flame. For that reason, rapid rotational thermal stabilization in the upper electronic state [24] is presumed which leads to a ratio that is approximately one. This assumption produces a systematic error in the measurements, but again the error can be bounded as relatively small based on expected deviations from the unity fluorescence yield ratio.

The decision of the transition pair has taken into account several factors: transition strength, transition isolation from neighboring transitions, and maximum energy difference in the ground state with no interference from surrounding species. The line pair used is $R_1(3)$ with $R_1(10)$. Also, vignetting is known to be a problem for measurements close to a surface [25, 26]. However, the plate and the burner surface are much larger than the flame, the effects of vignetting are greatly reduced for each picture. A small lens aperture is used to lessen the impact in the images at lower impinging plate heights. Further comparison of relative intensity for different impingement plate heights will be affected by the vignetting that decreases the overall solid angle collected for the smallest plate heights.

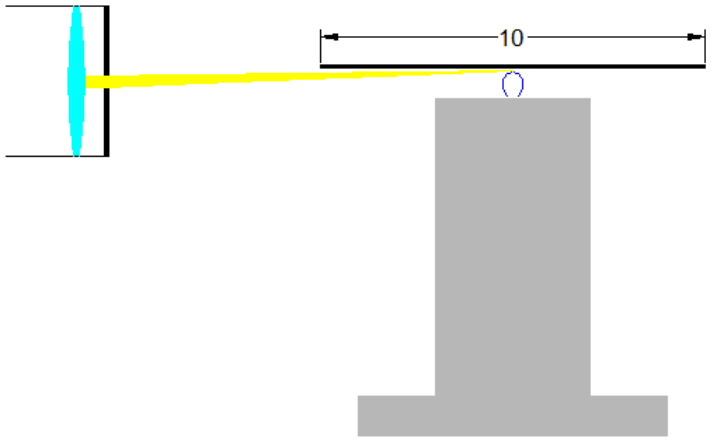

Figure 3.2: Collection optics $f\#\frac{1}{20}$ and $magnification = 2$ for $fl = 70\ mm$ (units in cm).

3.2 Experimental setup

The set up used for this specific realization of the technique can be seen in Figure 3.4 and includes a 10 Hz Surelite III Nd:YAG laser, followed by a Vista dye laser using (Rhodamine 590 dye dissolved in methanol) and a wavelength extender. The sheet forming optics comprise a spherical lens plus a cylindrical lens, forming a sheet with a height of 3 cm. The pulse energy was kept below 4 mJ where it could be experimentally observed that all the transitions used for the two-line OH PLIF are linear [27].

The linearity of the signal is checked by comparing the overall integrated signal of the fluorescence images from the camera with the average energy power from the laser used for the pictures. The fluorescing light is collected using an EM-ICCD PIMAX-4. The filter used (Semrock FF01-320/40-25) offers excellent transmission (70 %) to collect the light from the $A_2\Sigma^+ \leftarrow X\Pi_i$ $(0,0)$, $(1,1)$ transition. The images are taken using a 300 ns gate, which is long enough to collect the fully integrated signal of the fluorescence and short enough to suppress the background chemiluminescence. Absorption through the flame is negligible; due to the inner diameter of the burner being only 2 mm, there is not enough path length through OH to make absorption relevant. Two-hundred images are collected for every transition and position. After taking the fluorescence images for each transition, the

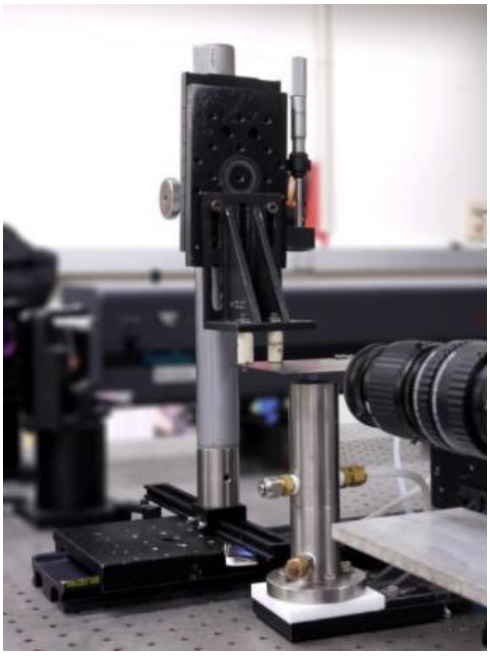

Figure 3.3: Translation stage for burner and plate.

flame is moved away, and replaced with a quartz dye cell with a diluted mixture of methanol with dye (Rhodamine560), in order to accurately correct for intensity variations across the laser sheet; this procedure is repeated for all the positions and transitions.

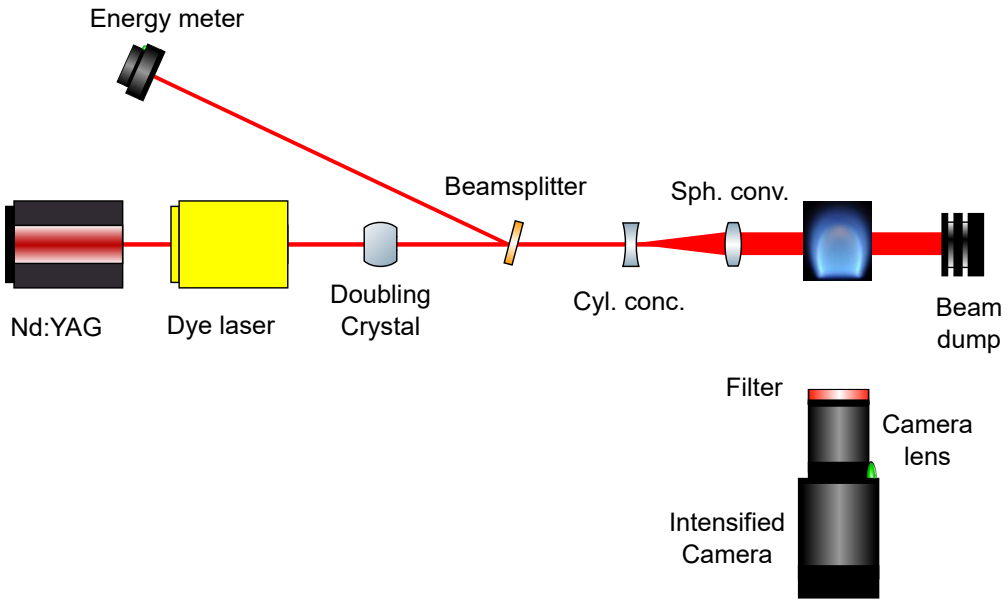

Figure 3.4: Experimental setup OH thermometry.

3.3 Image processing

Two-hundred images are averaged before ratioing to obtain a better signal to noise image. The averaged image is weighted with the laser intensity mapping obtained from the fluorescent dye mixture. The images are aligned one by one since the laser intensity mapping is taken for every transition, due to the nonlinear character of the doubling processes. After the energy correction, a temperature ratio is obtained for each pixel using Eq. 3.18. A threshold is set for the product of $I_1 \cdot I_2$ to only show temperatures when there is sufficient OH fluorescence signal from both transitions to make the measurements meaningful.

3.4 Results and discussion

Figure 3.5 shows the OH thermometry measurements as a function of plate to burner distance. The lower temperature limit is 1000 K because OH only is present in relevant concentrations at temperatures above 1000 K [21]. The peak temperature $T = 1650$ K is below the adiabatic methane flame temperature that is characteristic for diffusion flames, heat losses towards the burner and particularly the plate can explain this difference. The flame shows symmetry for all the conditions except for Figure 3.5c this is due to a combination of effects. The need of laser intensity corrections for each condition implies that the experimental setup is moved when rationing for each position and each transition. Manual alignment in increments of 1 pixel $pixelsize = 33$ μm is needed for each condition, interpolation is not suitable, meaning that in the most unfortunate situation fluorescence ratio can be misaligned by 1/2 pixel, this misalignment is reflected as an asymmetry in both sides of the temperature measurement. Summarizing, the potential sources of systematic errors include: an assumption of the same line broadening for both transitions $R_1(3)$ and $R_1(10)$, an assumption of similar quantum fluorescent yield, and nonlinear averaging due to small

movements in the flame position.

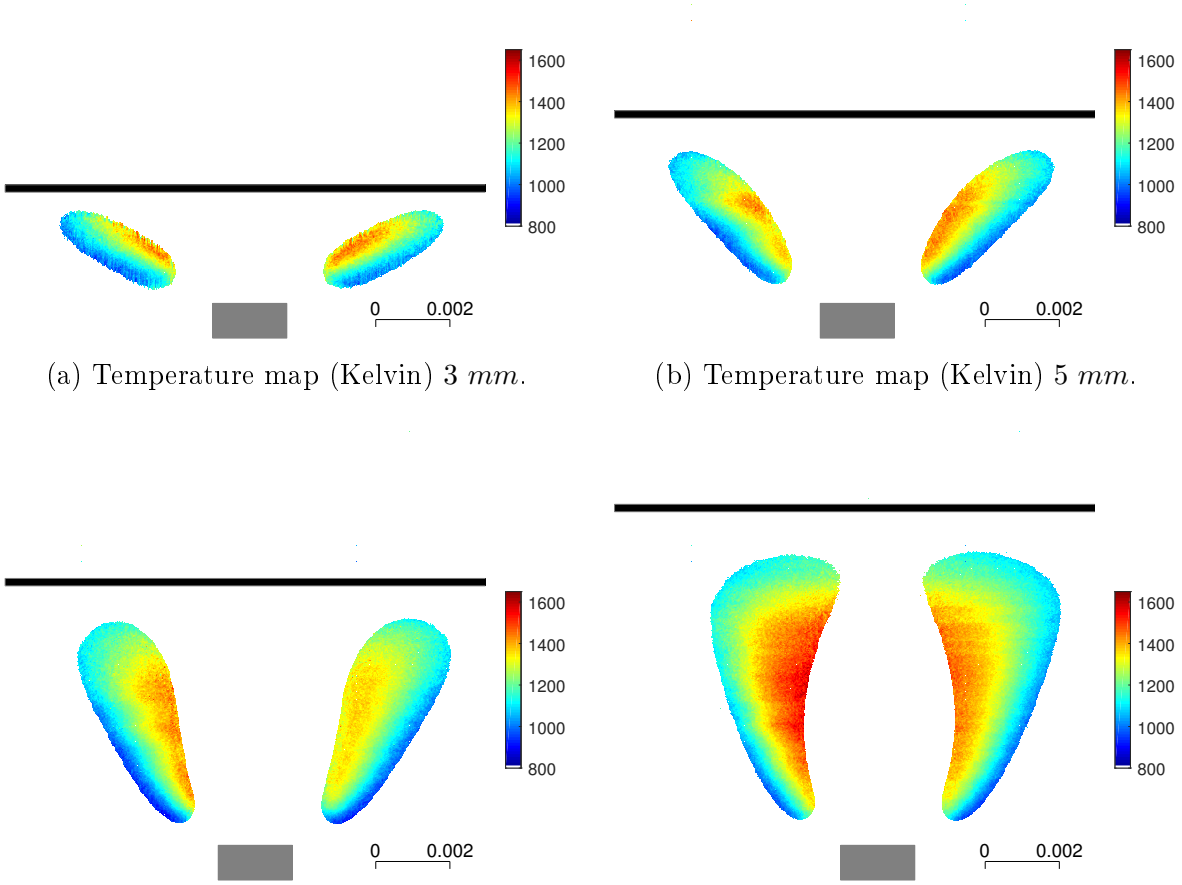

(a) Temperature map (Kelvin) 3 mm.

(b) Temperature map (Kelvin) 5 mm.

(c) Temperature map (Kelvin) 7 mm.

(d) Temperature map (Kelvin) 9 mm.

Figure 3.5: OH thermometry with different burner to plate distances.

3.5 Conclusions

Two-line OH PLIF thermometry measurements for a steady diffusion coflow flame are shown. The results are consistent with previous diagnostics applied in the same burner [6]; the hottest part of the flame coincides with the inner spatial gradient of the OH concentration.

The images also support the heat transfer studies shown in [28]. The peak temperature for

different conditions remains under 1650 K and is constant through all the heights of the plate relative to the burner. This finding is in agreement with previous experimental results of similar overall heat transfer to the plate despite different burner to plate heights. The areas displayed with temperature measurement, coincide with the regions with a higher number of OH molecules, the measurements confirm that a large effect of the impinging plate is to change the geometry of the flame, where the OH cloud is forced to open by the stagnating gas flow against the plate. The OH concentration profiles and the hot zones of the flame follow this geometry change.

Chapter 4

Two-photon CO PLIF

CO is a key pollutant to understand during the interaction between a small non-premixed coflow jet flame and an impingement surface downstream of the jet because there is evidence that the flame interaction with the surface (thermo-chemical and fluid mechanical) prevents the complete oxidation of CO to CO_2 by OH. Direct measurement of CO should help elucidate this phenomenon and clarify the relative roles of chemistry and flow in the interaction [16]. Several techniques are available for measuring CO: sampling, absorption, Raman spectroscopy, and laser induced fluorescence, among others. The technique chosen here is laser induced fluorescence due to the increased SNR versus Raman, the spatial specificity versus absorption, and the advantage of being non-intrusive versus sampling. There have been several works on 1D quantitative CO measurements under steady and unsteady conditions [25, 26, 29]; this chapter's focus is on 2D two-photon CO measurements, where the work in the literature is more limited [30, 31].

4.1 Background

The basis for two-photon CO fluorescence has been described extensively in the literature [32], and only a brief description is given here. The two-photon CO signal F depends on a broad range of parameters, and extrapolating from equation 3.16 is given by:

$$F \propto N F_{J''} W^{2v} \Phi(T, J') \tag{4.1}$$

$$\Phi(T, J') \propto \frac{A}{Q + A + P + \Gamma} \tag{4.2}$$

Where N is the total number of CO molecules in the volume; $F_{J''}$ is the fractional population of CO in the pumped ground state, which is a function of temperature; W^{2v} is the two-photon absorption rate coefficient, which is a function of the intensity squared as well as of the absorption cross section and the intensity of the laser profile; Q represents the quenching, which is a function of collisional partners, temperature, and pressure; A is the spontaneous emission from the excited state; P is predissociation, and Γ is the single-photon ionization rate coefficient, which is proportional to intensity. Although complex, many of these values can be determined, at least for relative conditions, permitting CO fluorescence to provide a clear qualitative spatial distribution of this important molecule.

4.2 Simulation

In order to find a more detailed behavior of the signal as a function of wavelength and temperature, a simulation of the Q branch of the $B_1\Sigma^+ \leftarrow X\Sigma^+$ transition for CO has been accomplished, following a procedure similar to that described in [33]. The rotational energies are calculated using the spectroscopic constants from [34, 35]. The line positions only include $\Delta J = 0$ in the Q branch, which is the strongest. For the line strength, the two-photon absorption cross-sections are taken from [36]. The excitation line shape is assumed to be

Gaussian with a FWHM of 0.8 cm^{-1}. The Honl-London factors for linear polarization are given by [37]. The transition line shape is calculated with a Voigt profile, combining the Doppler broadening and pressure broadening as described in Chapter 5. The population is assumed to follow a Boltzmann distribution, and the two photon cross section to be constant through all the rotational transitions. At high energy fluence, as studied in [38], the signal becomes dominated by the ionization effect, and in this regime, the signal becomes approximately linear with laser intensity; the ionization cross section is assumed to be constant over the range of wavelengths studied.

The wavelength chosen for the experiment is 230.034 nm; the wavelength is monitored and calibrated with a Xenon lamp and a 1 m spectrometer. This wavelength coincides with the high intensity region of Figure 4.1; and belongs to the transitions in the Q branch with a rotational quantum number around $J = 11$. As shown in Figure 4.2, the shift of populations in the lower level means that the fluorescence signal at 800 K is about 15 % higher with respect to the signal at 1200 K, and the signal at 1700 K is about 15 % lower than the signal at 1200 K. It is possible to use higher J value transitions to reduce this temperature dependence, but this comes at the expense of reduced signal strength. Our goal in this work is a planar measurement over a relatively large spatial area, and so we choose the higher signal intensity and accept the concomitant increase in correctable temperature dependence.

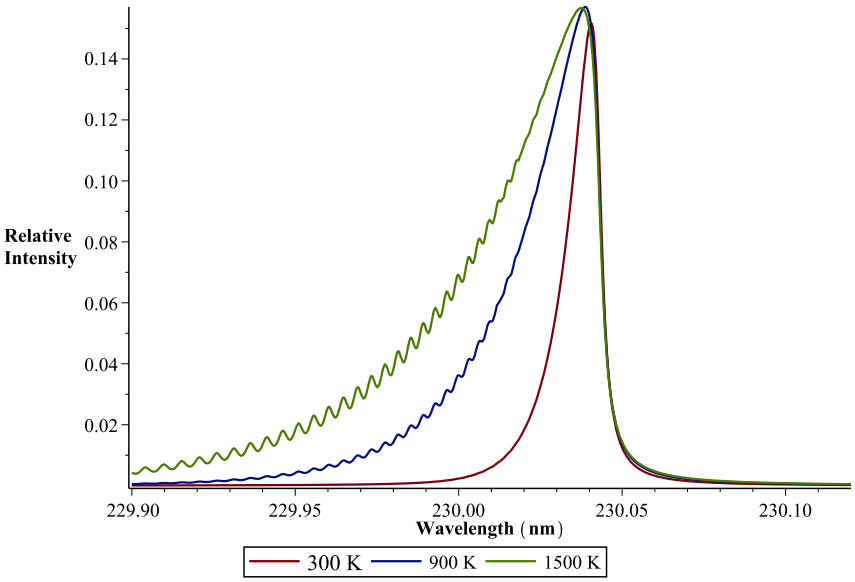

Figure 4.1: Simulated fluorescence excitation spectrum.

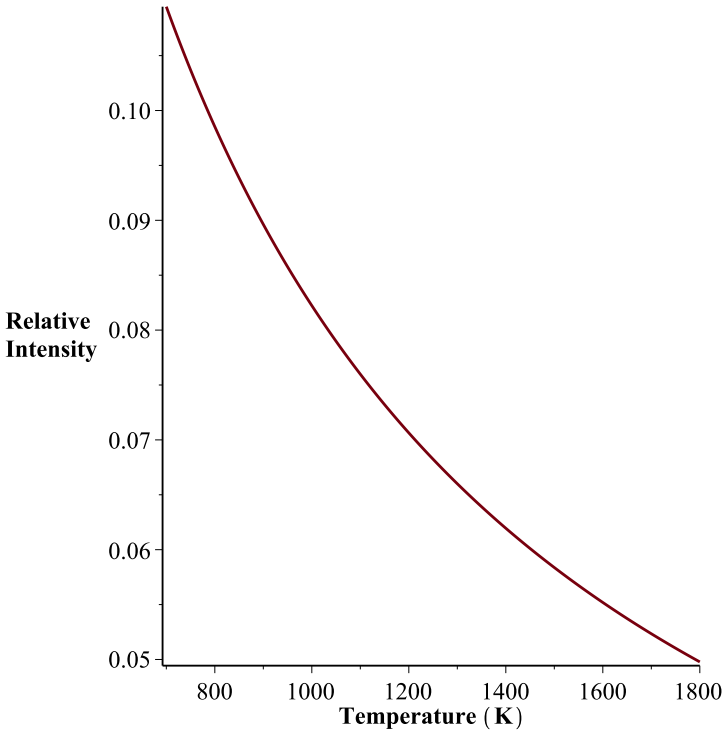

Figure 4.2: Simulated temperature dependence of the wavelength 230.034 nm.

4.3 Experimental setup

Figure 4.3 shows the apparatus used in the experiments. A Nd:YAG laser offering 850 mJ at 1064 nm, provided, after doubling and mixing, 250 mJ at 355 nm with 5 ns duration at (FWHM). The pumping energy at 355 nm goes into a dye laser (Vista) with Coumarin 460 diluted in methanol. After the laser energy at 460 nm is doubled and separated from the fundamental with a Pellin-Broca prism. The system is optimized for maximum output energy at 5 mJ per pulse. The laser beam is converted into a laser sheet using a quartz 100 mm focal length convex cylindrical lens that focuses the light into the burner, producing a laser sheet 4.5 mm tall. The lens has been chosen as a trade-off between the energy density of the flame and the Rayleigh range; both of them have to be maximized for a good signal. To correct the images for the intensity distribution of the laser sheet, a gas cell with CaF_2 windows and estimated concentration of CO around 300 ppm is used as a uniform sample target. The detection system used to take the images is an emICCD PI-MAX4 with a 75 mm lens and a filter centered at 486 nm with a 50% transmission window of 10 nm. The gate for the images is 100 ns.

Five positions are studied with the burner at different distances to the plate. The plate to burner distance is varied by moving the burner to keep the interrogated zone close to the plate. An average of 1000 frames is taken for each position for both the laser intensity profile and the fluorescence signal. A threshold value is given to limit the low end of the fluorescent images; in order to increase the SNR (signal to noise ratio), in Figures 4.4-4.8 a pattern is noticeable in the bottom of the laser sheet due to a combined effect of the threshold value and the low energy of the laser sheet. The corrections for the laser sheet are taken before and after the experiment to account for variations of the laser sheet through the experiment, as well as to correct for the non-linear doubling due to the rapid decay of the Coumarin 460 dye. An average of both is used to correct for the intensity variations through the laser sheet.

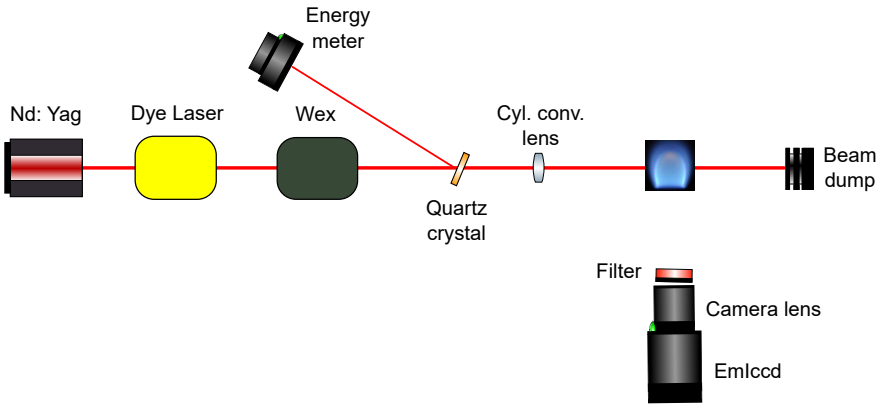

Figure 4.3: Experimental setup used for the 2D CO imaging experiments.

4.4 Photochemical effects

The cylindrical lens is selected to be 100 mm focal length to stay in the approximately linear regime of the CO fluorescence, that is, the regime where the CO ionization dominates. The beam waist is calculated to be about 50 μm in thickness, and the average power density is 0.5 GW/cm^2 approximately. The laser sheet limits the measurement region to the 4 mm closest to the plate. As mentioned earlier, the laser power density is high enough to ensure that ionization dominates the depopulation of the upper state, giving an approximately linear behavior with intensity for atmospheric pressure conditions. Several photochemical effects affect the fluorescence signal, including C_2 formation, CO ionization, CO_2 dissociation, and CO dissociation. The C_2 signal overlaps spatially, spectrally and temporally to some degree with the CO fluorescence signal. Using a long pass filter at 300 nm shows that the signal coming from C_2 is one order of magnitude higher than the CO signal (using 100 ns integration gate) for the studied flame. However, using a narrowband filter at 486 nm, and following similar procedures as described in [25], reduces the C_2 signal to a negligible level. CO dissociation is insignificant at the pressure and energy density values for the experiment. As described earlier, CO ionization is very important and dominates quenching in the depopulation of the excited state. The CO_2 dissociation has a strong dependence on temperature, and under 1400 K the process is weak enough that it has a relatively small

contribution. On the other hand, in the high temperature regions where CO_2 dissociation can be substantial, the CO concentration is high enough to keep the relative contribution of this dissociative interference small.

4.5 Results and discussion

Figures 4.4-4.8 show OH^* and two photon CO images for several plate to burner distances. The blue arrow of the CO two photon PLIF represents the area that is under the effects of laser emission. The main goal of this work is to relate the overall CO emissions with the burner to plate distance and investigate the measurements done in [6, 16], where the CO emissions increase by 3000% from an 11 mm separation to 3 mm. Because of this significant dependence on relatively small changes in burner to plate distance, showing the relative spatial distribution of CO can be key to understanding and preventing excessive CO release for impinging flames.

The most striking result from the CO images is the strong signal coming from the CO nearby the plate. This intensity can be understood by the boundary layer effect created by the plate. The plate temperature measured by an IR camera is found to be 500 K from the top. Because the plate is made of stainless steel (low thermal conductivity) and 2 mm thick, it is safe to assume that the temperature gradients in the direction of the plate thickness are small. Figure 4.2 shows a clear trend where the wavelength used excites rotational transitions that bias the fluorescence signal, increasing it when the CO molecules are "colder" due to the higher population at the low rotational levels, see Figure 4.2. This effect combined with the density effect, where the density scales inversely with temperature increases the number of molecules per unit volume, has a multiplying effect that produces high intensities close to the plate.

It is also important to point out that the radial qualitative signal distribution does not follow the intuitive concentration profile. This profile can also be explained with similar reasoning, where the diffused CO towards the core of the flame is colder and fluoresces more. In Figures 4.4 and 4.5 it can be seen how the thickness and the intensity of the CO signal coming from close to the plate are reduced due to the cylindrical geometry of the configuration. This work is expanded to also study the effects of an electric field in an impinging flame; those effects are out of the scope of this Chapter, but for completeness of the data set the results are shown in Appendix B. Vignetting can create different collection efficiencies for each pixel [25] and these efficiencies are determined by the geometrical configuration of the camera, the plate, and the burner. In this case, a higher f-number reduces the solid angle of the light collected; this solid angle is more homogeneous for each pixel, therefore limiting the effect of vignetting. A high f-number is used to reduce this effect.

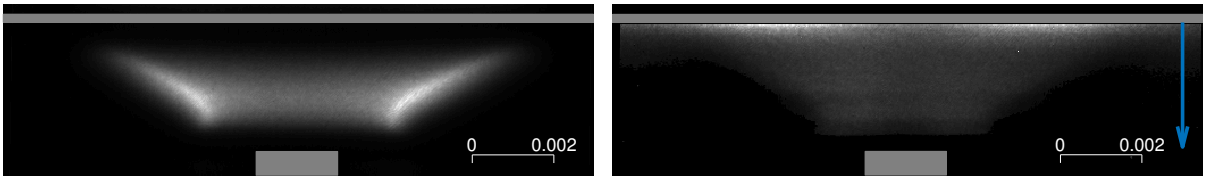

(a) CO^* chemiluminescence. (b) CO 2-photon PLIF.

Figure 4.4: 3 mm burner to plate OH^* and 2-photon CO PLIF.

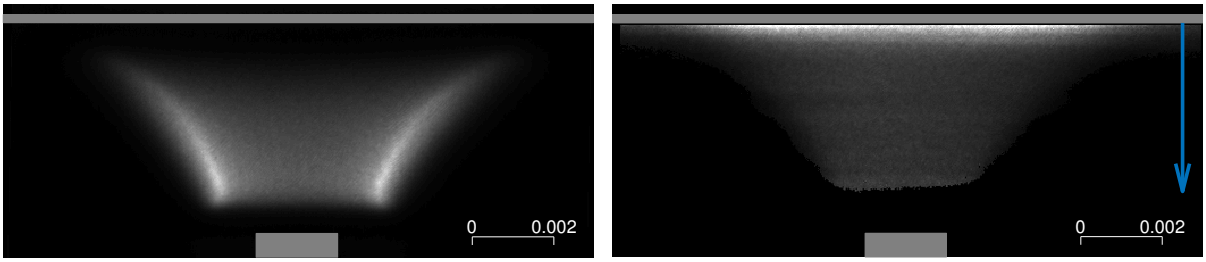

(a) CO^* chemiluminescence. (b) CO 2-photon PLIF.

Figure 4.5: 5 mm burner to plate OH^* and 2-photon CO PLIF.

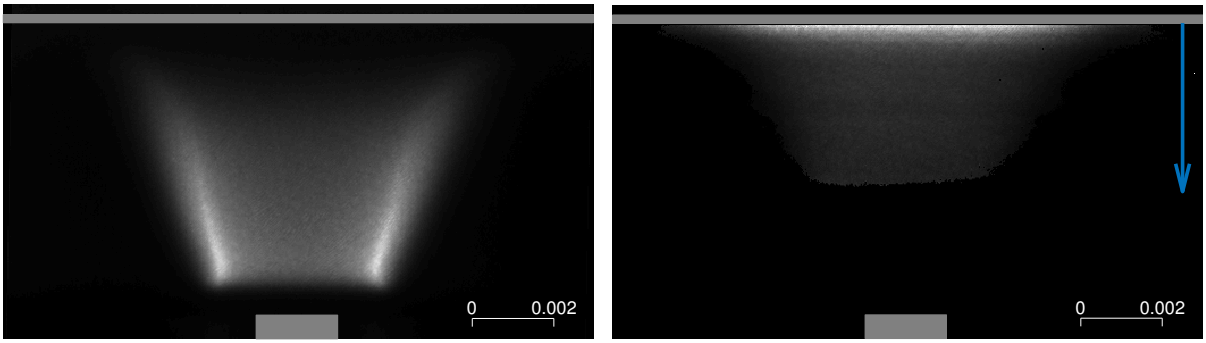

(a) CO^* chemiluminescence. (b) CO 2-photon PLIF.

Figure 4.6: 7 mm burner to plate OH^* and 2-photon CO PLIF.

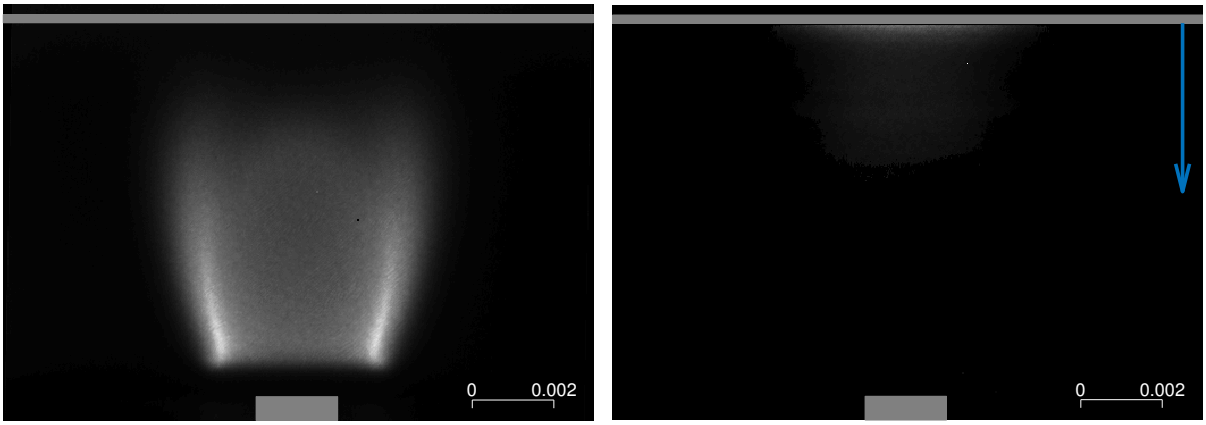

(a) CO^* chemiluminescence. (b) CO 2-photon PLIF.

Figure 4.7: 9 mm burner to plate OH^* and 2-photon CO PLIF.

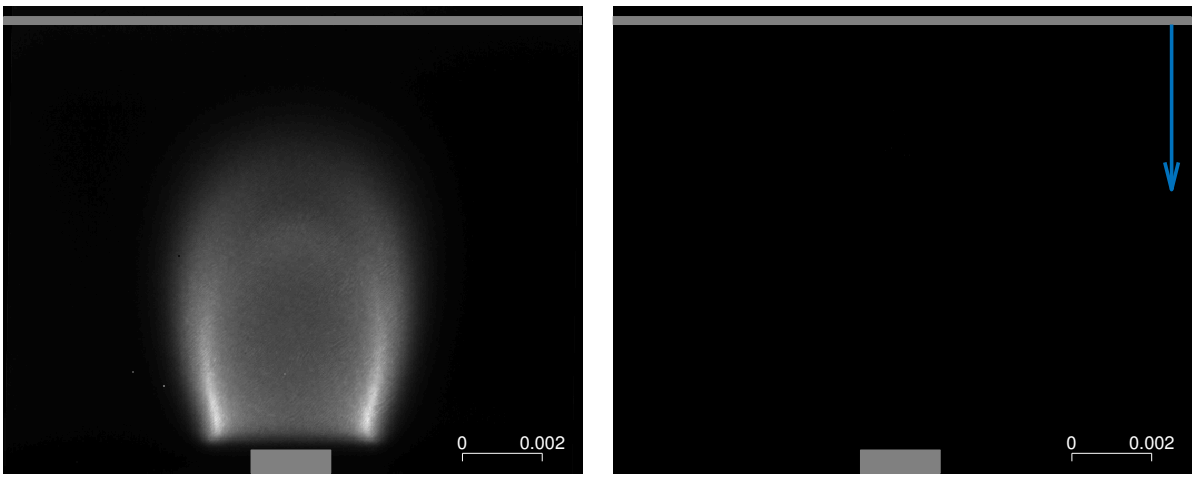

(a) CO^* chemiluminescence. (b) CO 2-photon PLIF.

Figure 4.8: 11 mm burner to plate OH^* and 2-photon CO PLIF.

4.6 Conclusions

Qualitative two-photon CO PLIF measurements in a non-premixed coflow impinging flame have been accomplished. The measurements provide experimental evidence of the mechanism for increased CO emission for impinging flames. OH is a significant oxidizer for CO to CO_2 oxidation, and the measurements show that the plate temperature and the boundary layer effect provides a physical path for the non-oxidized CO to release into the ambient without oxidizing, thereby increasing the CO emissions.

Chapter 5

OH fluorescence

Fluorescence and chemiluminescence are significant from a historical standpoint in combustion research. In this chapter fluorescence and chemiluminescence will be studied in detail for the OH molecule, which is a key reactant for diffusion flames. The use of OH and its electronically excited state OH^* have been described as heat release zone and reaction zone markers in several publications [39, 40]. These two pieces of information make OH PLIF and OH^* chemiluminescence a combination that can provide very beneficial information regarding the physical extent and progress of combustion processes. In the experimental configuration that will be described, the combination of semi-quantitative OH PLIF and OH^* imaging versus pressure will be discussed.

5.1 Background

Laser induced fluorescence (LIF) is one of the most robust optical techniques available as a combustion diagnostic. LIF is viewed as absorption, followed by some finite period of time, by spontaneous emission from the excited manifold. The term "manifold" is used since

it is possible to observe the fluorescence at a different wavelength than the one utilized for the excitation. For diagnostic purposes, the observed wavelength is spectrally shifted intentionally to avoid interference from Rayleigh scattering, spuriously scattered laser light from surfaces or Mie scattering from ambient dust. The absorption processes that occur in LIF have much larger cross sections than Raman effects in which the molecule is perturbed far from resonance. Therefore, the fluorescence signal is many orders of magnitude stronger than other laser induced phenomena that might be used for species detection.

There are several criteria which must be satisfied to perform quantitative fluorescence measurements on a given molecule. First, the emission spectrum must be known. This is not always easy because of the molecules, once excited, may dissociate prior to emission of a photon; this phenomenon is known as predissociation. If the photons are sufficiently energetic (or multiple photon processes are active), the molecule can also become ionized, which is known as photoionization. Also, the molecule must have an absorption wavelength accessible to a tunable laser source. Nowadays the spectral range covered by tunable dye lasers is roughly the wavelength interval from 200 nm to 1.5 μm. Through the use of multiphoton techniques, absorptions below 200 nm can also be accessed. Finally, the rate of fluorescence decay of the excited state must be known. These decay losses are due to collisional deactivation, photo-ionization, and/or predissociation. Moreover, if other molecules are present this rate may be increased considerably due to the collisions with the other molecules; this collisional loss is known as quenching.

5.2 Theoretical corrections

5.2.1 Broadening effects and overlap integral

The overlap integral effects are important because flames have large spatial temperature gradients, and the line shape and line-width can change, based on pressure (pressure broadening) and temperature (Doppler broadening). Hence the balance between Doppler dominated and pressure broadened transitions can change through the flame. The transitions are modeled following a Voigt profile that combines Gaussian and Lorentzian profiles [19].

The Doppler broadening follows a Gaussian line shape:

$$g_D(\nu) = \frac{c}{\nu_0}\sqrt{\frac{m}{2\pi kT}}\exp\left[-4\ln 2\frac{(\nu-\nu_0)^2}{\Delta\nu_D^2}\right] \tag{5.1}$$

Where c is the speed of light; ν_0 the transition center frequency; m the molecular mass of the absorbing molecule; k, Boltzmann's constant; $\Delta\nu_D$, the transition width (FWHM); and T, temperature. Where $\Delta\nu_D$ is:

$$\Delta\nu_D^2 = \frac{2\nu_0}{c}\sqrt{\frac{2\ln(2)kT}{m}} \tag{5.2}$$

The pressure broadening follows a Lorentzian line shape:

$$g_c(\nu) = \frac{\Delta\nu_c}{2\pi}\frac{1}{(\nu-\nu_0)^2+(\Delta\nu_c/2)^2} \tag{5.3}$$

The $\Delta\nu_c$ is the transition width (FWHM), both $\Delta\nu_c$ and $\Delta\nu_D$ are calculated from the local composition temperature and pressure from OpenFOAM simulations, see Chapter 6, of the flame for each mesh cell; the pressure broadening coefficients are obtained from [41] and [42]. There is no literature for oxygen, and for this particular case the same coefficient as nitrogen is assigned; as can be seen in [41] the trends in air and nitrogen are similar. Finally, the

combination of both broadening phenomena is given by:

$$g(\nu) = 2\sqrt{\frac{\ln 2}{\pi}}\frac{V(a,x)}{\Delta\nu_D} \tag{5.4}$$

$$V(a,x) = \frac{a}{\pi}\int_{-\infty}^{\infty}\frac{e^{-y^2}}{a^2+(x+y)^2}dy \tag{5.5}$$

$$a = \sqrt{\ln 2}\frac{\Delta\nu_c}{\Delta\nu_D} \tag{5.6}$$

$$x = 2\sqrt{\ln 2}\frac{(\nu-\nu_0)}{\Delta\nu_D} \tag{5.7}$$

The lineshape is then normalized for each simulation point:

$$\int_{-\infty}^{\infty} g(\nu)d\nu = 1 \tag{5.8}$$

The laser linewidth is estimated from the excitation scans to be a Gaussian with $(FWHM) = 0.15\ cm^{-1}$.

$$\phi(\nu) = \exp\left[-\frac{4\ln 2(\nu-\nu_0)^2}{(FWHM)^2}\right] \tag{5.9}$$

The overlap integral is calculated as:

$$overlapintegral = \int_{-\infty}^{\infty}\phi(\nu)\cdot g(\nu)d\nu \tag{5.10}$$

For an easier visualization of the results and relative effect in the fluorescence signal, all the images are normalized to the point with the higher value of the *overlapintegral* in the condition of 1.4 *bar*. To reduce the computational cost of the overlap integral, only the simulation points with OH mole fraction higher than 1% are considered. The simulated results that are seen in Figure 5.1 are in qualitative agreement with [43], as the overall values of the overlap integral decay as a function of pressure, due to the effects of pressure broadening. The relative effects at 1.4 *bar*, give higher values of the overlap integral at the

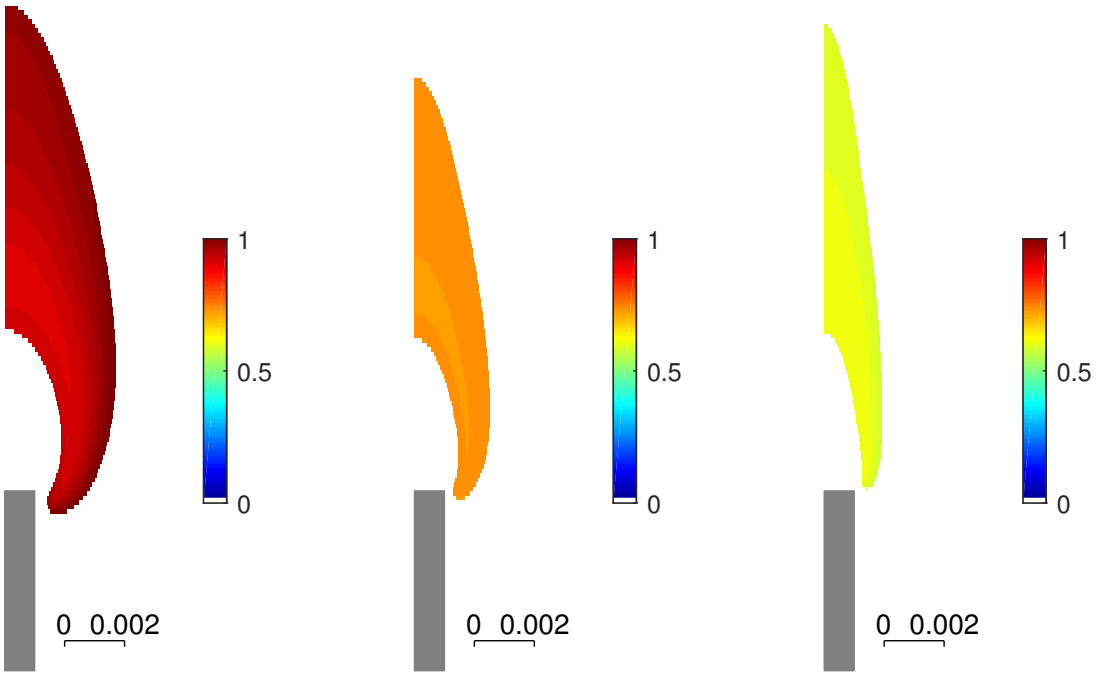

(a) 1.4 bar. (b) 3.3 bar. (c) 5.7 bar.

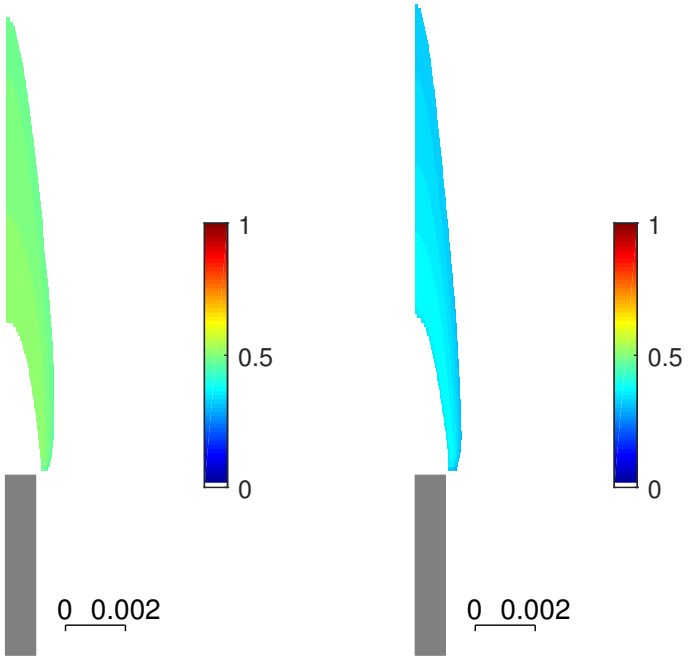

(d) 8.9 bar. (e) 11.1 bar.

Figure 5.1: Simulated overlap integral effects as a function of pressure.

cold OH regions and lower values in the hot regions because the shape is dominated by Doppler broadening. On the other hand at 11.1 *bar* this relative trend is the opposite due to the line shape being dominated by pressure broadening.

5.2.2 Quantum fluorescence yield

The determination of the quantum fluorescence yield is key to evaluate the fluorescence signal in a semi-quantitative manner. The spontaneous decay coefficient is calculated from the natural fluorescence lifetime of OH, which is about two orders of magnitude longer than the typical quenching lifetime at atmospheric pressure. $A_{J'J''} \approx 10^6\ s^{-1}$ and $Q_{J'J''} \approx 10^8\ s^{-1}$ so the correction effects from spontaneous decay are very small. The transient energy exchange in the upper electronic state complicates the modeling. The broadband detection used in this work ($320 \pm 20\ nm$) covers almost all the rotational lines and two vibrational transitions. This breadth allows the approximation of Q_{eff} as being collision independent of the molecule distribution in the upper excited state [44]. With this assumptions, the quenching becomes only a function of the density, temperature and collisional partners.

$$Q_{J'J''} = N_{tot} \cdot \sum_i \chi_i \sigma_i \upsilon_i \tag{5.11}$$

$$\upsilon_i = \left(\frac{8 k_b T}{\pi \mu_{i,m}} \right) \tag{5.12}$$

Where N_{tot} is the total number of molecules, σ_i is the quenching cross section of species i, χ_i are the mole fractions, υ_i is the relative velocity between OH and the collisional partner, k_b the Boltzmann constant and $\mu_{i,m}$ the reduced mass of species i and excited molecule m. The quenching cross sections and the coefficients are modeled following [45, 46]. The modeled quenching species include H_2O, CH_4, CO_2, O_2, H_2, and C_2. N_2 effects can be neglected since the relative quenching effect is very minimal compared to that of the molecules included.

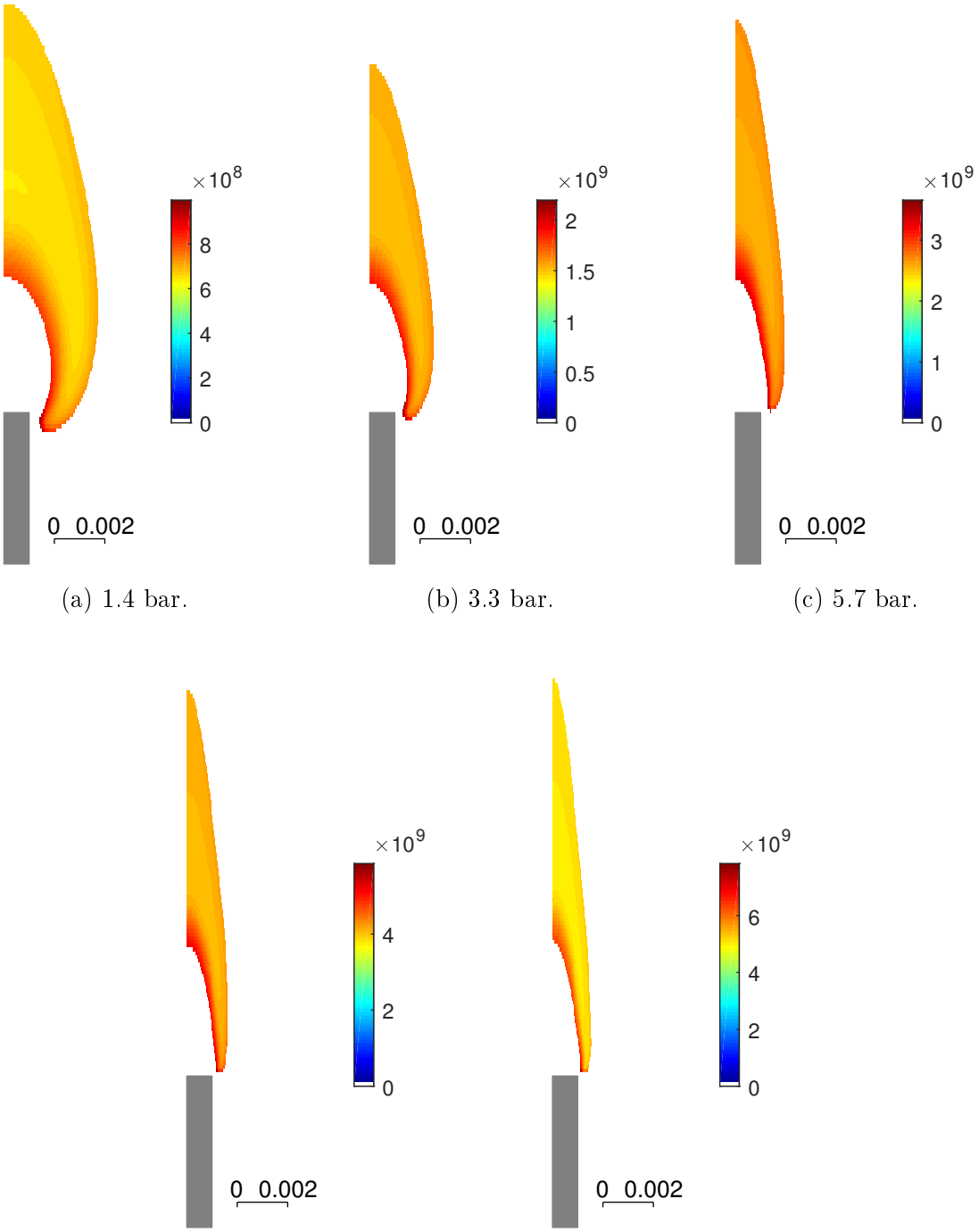

(a) 1.4 bar. (b) 3.3 bar. (c) 5.7 bar.

(d) 8.9 bar. (e) 11.1 bar.

Figure 5.2: Simulated quenching in (s^{-1}) as a function of pressure.

The simulations seen in Figure 5.2 are consistent with the literature [43]. As expected quenching is smaller in the high temperature zones due to the decreased $N_t \propto \frac{1}{T}$ despite the

increased relative speed between the collisional partners and OH molecules $\upsilon \propto \sqrt{T}$. The methane side of the non-premixed flame quenching is higher than the air side because CH_4 is a good quencher; on the other hand, on the air side O_2 is the dominant quencher, but it is present at a smaller mole fraction compared to CH_4 on the fuel side.

5.2.3 Temperature dependence

The transition selected from the $A_2\Sigma^+ \leftarrow X\Pi_i$ $(1,0)$ is the $Q_1(7)$. This transition has a relatively small temperature sensitivity over the range of temperatures where OH is present [47] (1000 K to peak flame temperature), and the Q branch is a good choice due to the line strength. Often other weaker branches such as the P branch are preferred to minimize the absorption effect through the flame at high pressures, but with such a small flame (methane tube i.d 2 mm) those effects are negligible compared to soot absorption which will become present at higher pressures. At high pressures, the quantum fluorescence yield is smaller, and the overlap integral is also reduced. To study this temperature sensitivity, the temperature dependence of the ground state OH is simulated [48]. The images shown evaluate Figure 5.3 in each point of the OpenFOAM simulation results; only considering cells with an OH mole fraction higher than 1%. Figure 5.4 shows the normalized temperature effect.

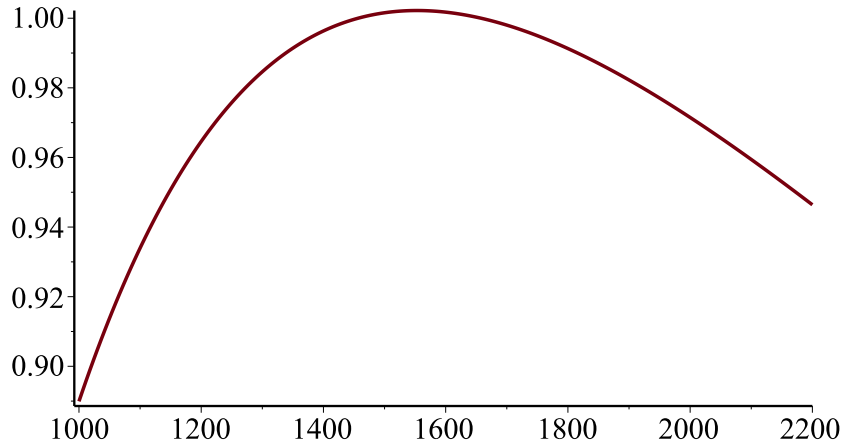

Figure 5.3: $Q_1(7)$ temperature dependence.

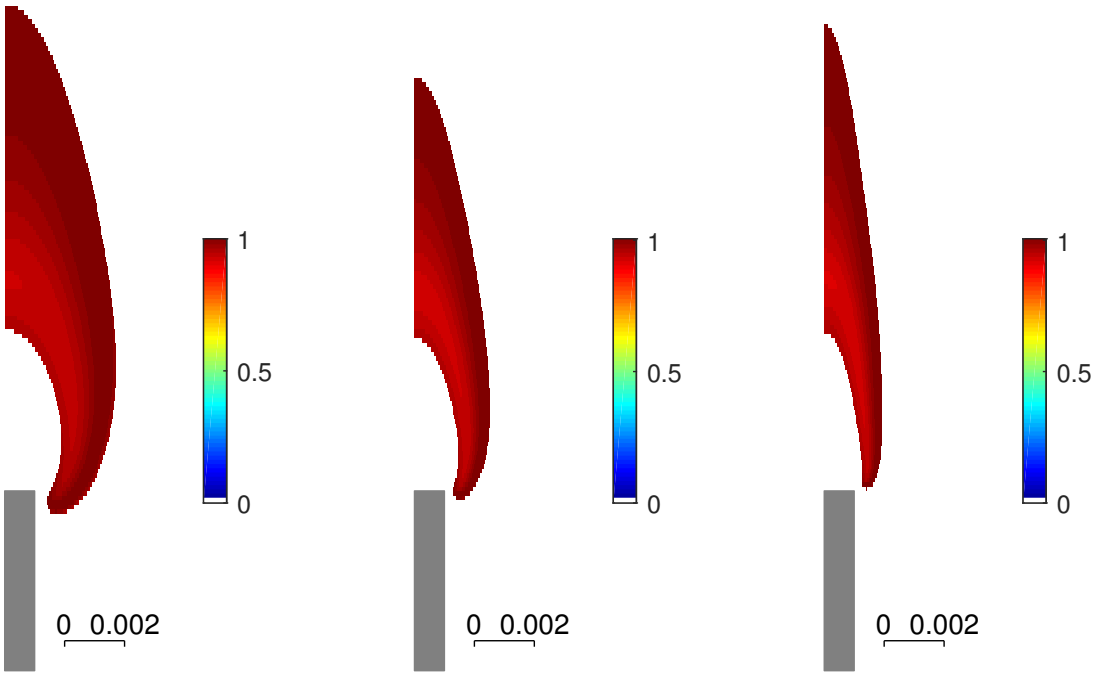

(a) 1.4 bar. (b) 3.3 bar. (c) 5.7 bar.

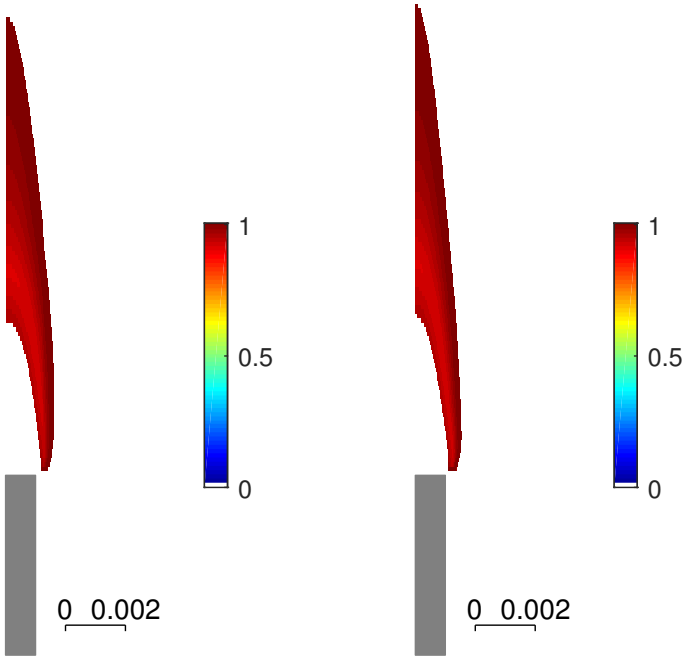

(d) 8.9 bar. (e) 11.1 bar.

Figure 5.4: Simulated normalized temperature dependence.

The qualitative trend through all the pictures is very similar. The hottest spots $T > 1900$ have a smaller fluorescence emission; as seen in Figure 5.3. This position corresponds to the OH cloud closer to the tube (inner gradient); farther from the inner tube the OH cloud cools down, and the relative fluorescence goes through the peak of the temperature dependence and then goes back down as the OH cloud cools down further from the tube. With the above described analysis tools and methods, it will be possible to quantitatively assess OH fluorescence from the OpenFOAM simulations and compare it with the experiments as is shown in Chapter 6.

5.3 Optical setup

The PLIF measurements are conducted by pumping OH at 283.2 nm $Q_1(7)$ in the $A_2\Sigma^+ \leftarrow X\Pi_i$ $(1,0)$ band and detecting fluorescence in the $A_2\Sigma^+ \leftarrow X\Pi_i$ $(0,0)$, $(1,1)$ band. The specific setup used includes a 10 Hz Surelite III Nd:YAG Laser, followed by a dye laser (Vista) and a doubling crystal. The sheet forming optics comprise a spherical plus a cylindrical lens forming a sheet with a height of 30 mm. The fluorescence light is collected using an EM-ICCD PIMAX-4 with a filter (Semrock FF01-320/40-25). The fluorescence images are recorded at a sampling rate of 10 Hz using a 30 ns gate, which is sufficient to collect the fully integrated signal of the fluorescence at high pressures while minimizing the effects of background chemiluminescence, natural soot luminescence and soot laser induced incandescence. 300 images are collected for each pressure with an on CCD accumulation of 20 exposures per image, and the background emission is subtracted from the raw fluorescence images. The soot luminescence is also corrected by off resonant excitation since soot luminescence from LII becomes important as the pressure increases. The excitation scan is performed scanning the dye laser at a speed of 0.005 $\frac{nm}{s}$ from 282 nm to 282.5 nm, with a total of 1000 images for each excitation scan. The background chemiluminescence is subtracted running the same

acquisition conditions for the camera with no laser excitation. The lifetime measurement for the Laser Induced Incandescence (LII) signal uses the same settings as the fluorescence collection but reducing the gate width to 20 ns to increase the time resolution of the plot. The detection delay is varied to observe the evolution of the signal.

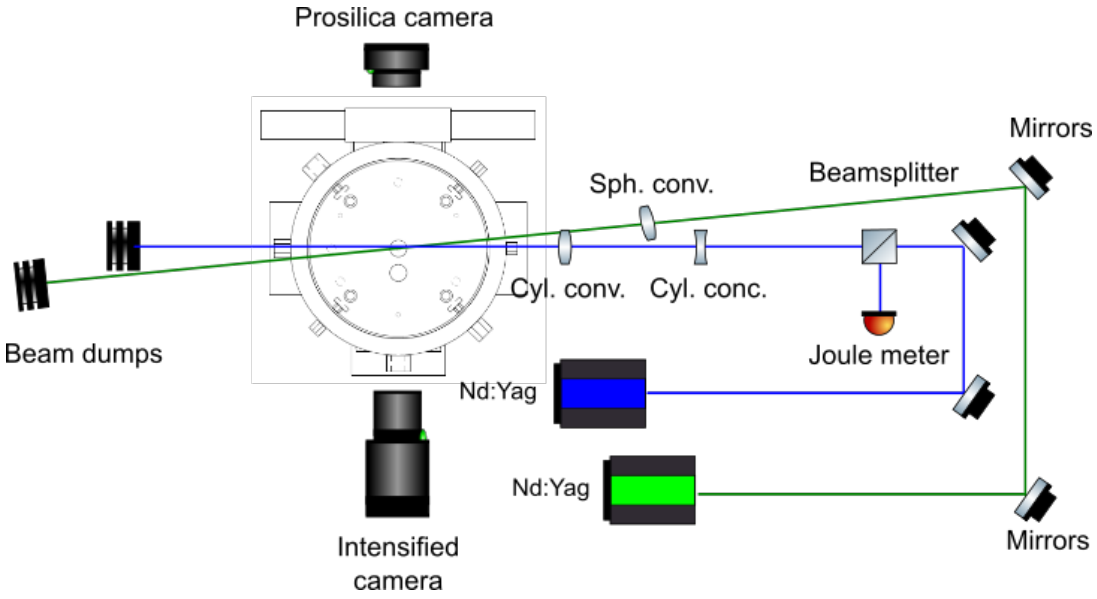

Figure 5.5: OH PLIF experimental setup.

The OH^* images are recorded with the same collection optics as the LIF apparatus, with an exposure of 50 ms; each picture represents a single frame. The CH^* images are collected with a Prosilica GC1380 camera with 20 ms exposure time. The filter used is centered at 430 nm (Edmund Optics NT62-139) [49].

5.4 Experimental procedure

The experimental procedure for each ambient pressure is the following. Set up the back pressure regulator to the target pressure, close air and methane lines and adjust the nitrogen flow to reach the desired pressure, once the desired pressure is reached, adjust the air, nitrogen flow rates to the desired value until steady state pressure is reached. Ignite the

flame using laser ignition, and wait until steady state pressure is reached again, and then readjust needle valves if needed in order to obtain the desired flow rate.

The ignition is performed through laser induced breakdown, with a Quanta ray INDI Nd:YAG doubled to 532 nm and focused using a spherical convex lens with a $fl = 25\ cm$. All the experiments are conducted under an excess flow of nitrogen in the environment to keep the global mixture inside the chamber outside of flammability limits.

With the current design, it is not possible to obtain a steady flame at pressures over 12 bar due to the buoyant instabilities, which produce an oscillatory vertical motion that complicates steady fluorescence measurements. A chimney might help to reduce the buoyancy effects, but this would complicate further the LIF measurements and the ignition procedure. The use of helium as an inert gas to suppress the buoyant instabilities is ineffective due to the low momentum of the coflow of air at high pressure, and the velocity distribution is affected by the buoyant forces in a helium environment that compromise the complete combustion of methane. The burner is operated at a constant mass flow rate equivalent to 15 $\frac{cm}{s}$ at standard temperature and pressure (STP) conditions both on the air and on the fuel side. For future work, it might be possible to invert the burner to use to our advantage buoyancy to obtain a stable high pressure coflow flame over 15 bar, but the current work provides significant pressure effect insights even though limited to the stable operating range below 12 bar.

5.5 Results and discussion

Figures 5.6, 5.9, 5.11 and 5.13, are normalized for visualization reasons. Figure 5.7 is not normalized and is meant to be representative of the overall visual flame changes with pressure. Figures 5.6 and 5.7 show images of OH^* and CH^* at different pressures, the flame height

is constant throughout the range of pressures in accordance with [14]. The flame height definition used is based on the lower gradient of the OH fluorescence signal through the axis of symmetry of the flame. Flame height is approximately constant since mixing is dominated by the ratio of axial convective velocity with radial diffusion and both effects balance each other.

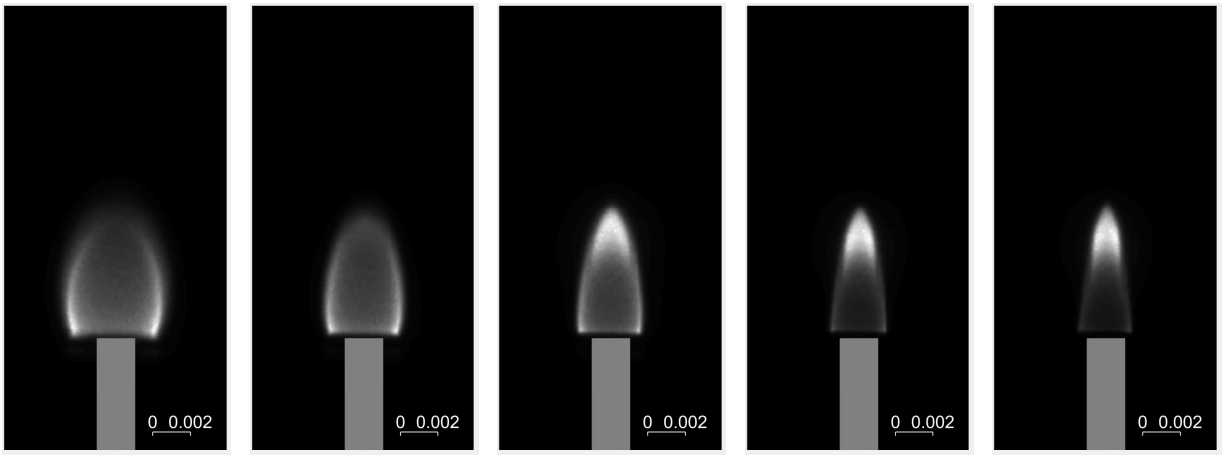

(a) 1.4 bar. (b) 3.3 bar. (c) 5.7 bar. (d) 8.9 bar. (e) 11.1 bar.

Figure 5.6: OH^* chemiluminescence.

(a) 1.4 bar. (b) 3.3 bar. (c) 5.7 bar. (d) 8.9 bar. (e) 11.1 bar.

Figure 5.7: CH^* chemiluminescence.

The total CH^* and OH^* chemiluminescence signals decay with pressure; this decay is influenced by chemistry effects and collisional quenching, and it is dominated by the latter. Figure 5.8 shows an integrated section of the OH^* chemiluminescence with a spatial filter to avoid soot luminescence interference. Comparing the fluorescence decay with the quenching increase suggests that the decay rate of the fluorescence signal is slower than the decay that would correspond to an exclusive quenching effect, further suggesting that chemical effects

increase the production rate of this excited species.

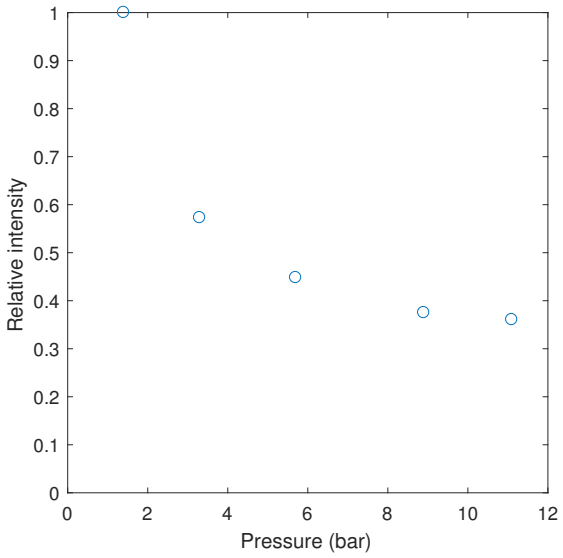

Figure 5.8: Integrated OH^* chemiluminescence.

Figure 5.9 shows OH PLIF at different pressures; the fluorescence signal decays as pressure increases, the thickness of the OH cloud decreases as a function of pressure, and the flame becomes thinner as the pressure increases. Figure 5.10a shows the overall fluorescence signal as a function of pressure. Peak fluorescence intensity decays due to collisional quenching, and pressure broadening dominates over the density increase effect. Figure 5.10b shows the total integrated fluorescence signal from the left and right sides of the flame; the left side is the first one interacting with the laser, the right hand side shows some absorption at the higher pressures (20% at 11.1 *bar*). This absorption can be observed when looking in detail at the images from Figure 5.9; projecting the intensity to the vertical axis reveals that the absorption effect comes from soot that later translates into a LII signal. The spatial soot distribution being predominantly in the inner core of the OH distribution suggests that the left side of the flame is unaffected by absorption effects.

The biggest difference between the high pressure LIF and low pressure LIF is the appearance of a LII signal that interferes both spatially and in frequency with the LIF signal. To further investigate this effect, a spatially resolved excitation scan is shown in Figure 5.12, which

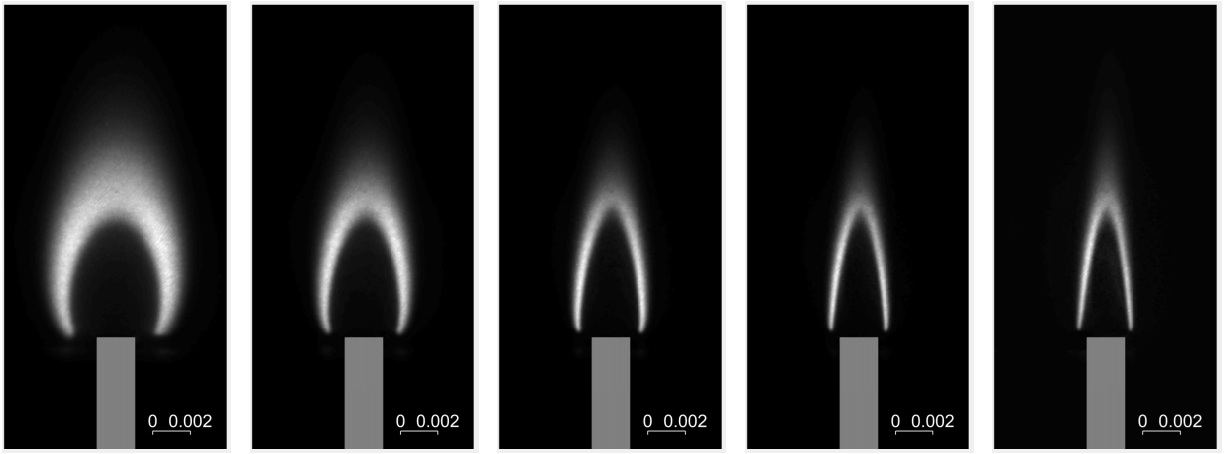

(a) 1.4 bar. (b) 3.3 bar. (c) 5.7 bar. (d) 8.9 bar. (e) 11.1 bar.

Figure 5.9: *OH* fluorescence.

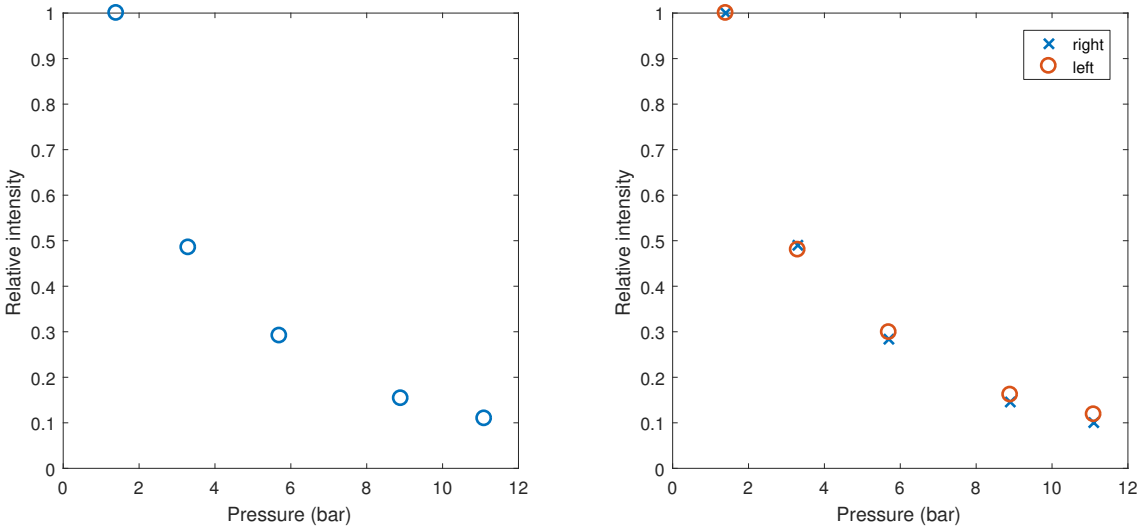

(a) Fluorescence signal vs pressure. (b) Fluorescence right vs left side.

Figure 5.10: *OH* fluorescence decay.

corresponds to the integrated areas shown in Figures 5.11a and 5.11b, respectively. The spectrum background from the excitation scan from Figure 5.11a increases over 100% from 1.4 *bar* to 11.1 *bar*. The background from the spatially filtered excitation scan from Figure 5.11b increases less. This effect hints at the presence of a spatially biased signal, that can be seen in Figure 5.13, which shows three different integrated images from the excitation scan. Figure 5.13a covers the wavelengths of the first gray zone shown in the excitation scan, Figure 5.13b covers the wavelengths in between the gray zones, including the rovibrational

transition $Q_1(7)$, and Figure 5.13c covers the second gray zone. The spatial distribution of Figure 5.13 shows contributions from LII. Figure 5.15 shows the decay time of the LII signal; the decay time matches previously measured lifetimes for similar pressures [50].

Figure 5.14 shows mole fractions for the hydroxyl radical, Acetylene and Pyrene, the simulation details can be found in Chapter 6. Acetylene is one of the key components for soot formation, and it is one of the most important molecules for soot growth. Pyrene to pyrene collisions has been used as soot inception [51]. The qualitative agreement of acetylene with the LII signal is better.

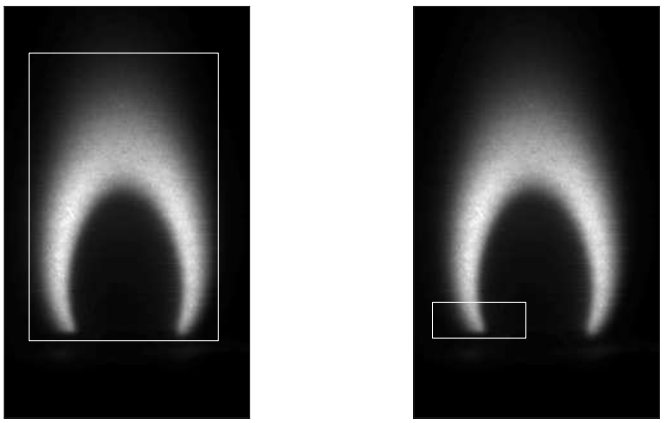

(a) (b)

Figure 5.11: Area integrated in excitation scan.

5.6 Conclusions

One aim of this experimental result is to better understand challenges of laser diagnostics at high pressure, as well as to obtain physical insights of high pressure combustion for non-premixed flames. For this purpose, OH Fluorescence, OH excitation scans, OH^* and CH^* measurements were presented for a non-premixed coflow flame at laminar conditions over a range of pressures from 1.4 bar to 11.1 bar. The OH^* measurements suggest an increase in the chemical reactions that produce OH^* as the pressure increases due to the signal decay being

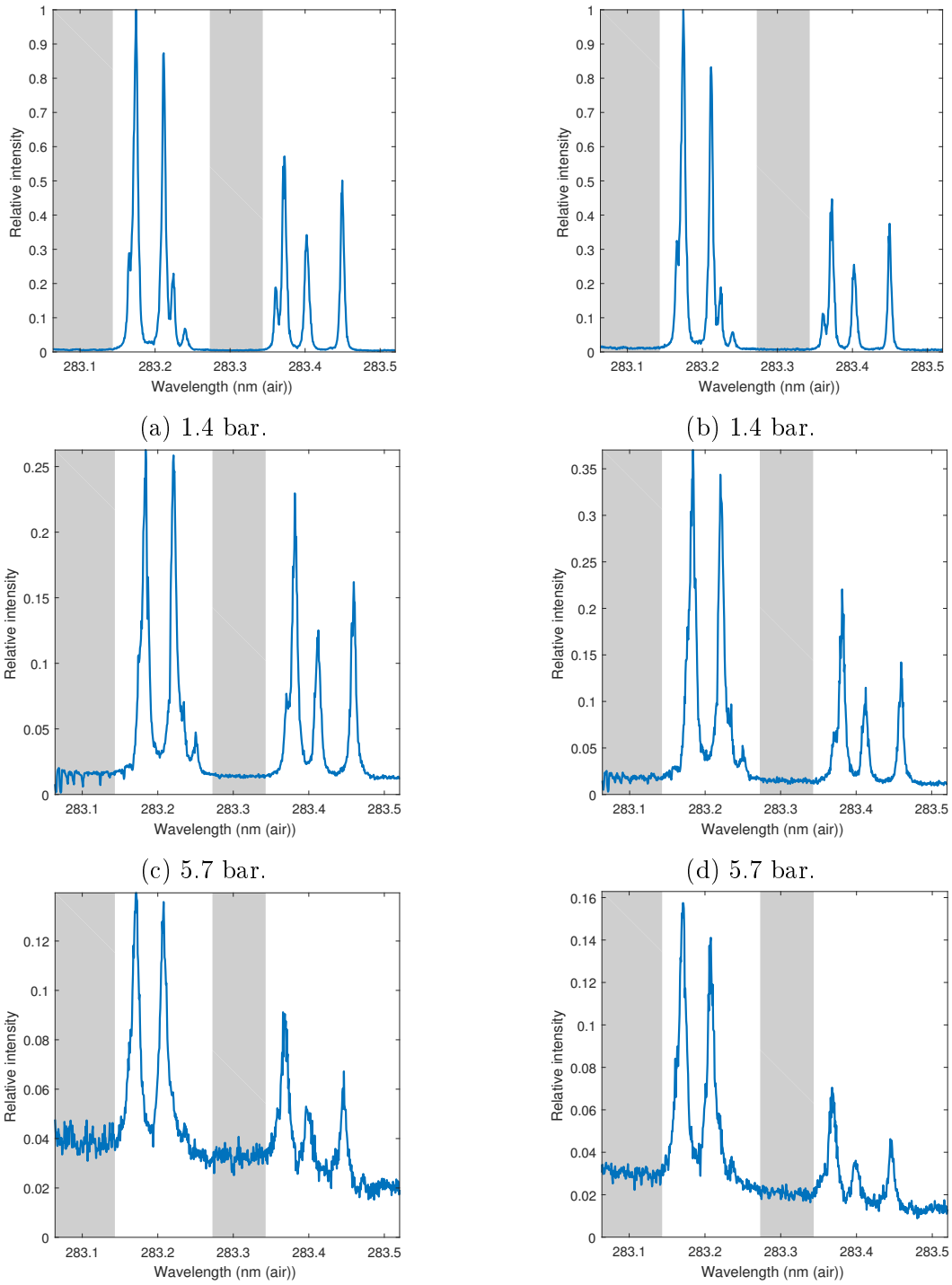

(a) 1.4 bar.

(b) 1.4 bar.

(c) 5.7 bar.

(d) 5.7 bar.

(e) 11.1 bar.

(f) 11.1 bar.

Figure 5.12: Excitation scan from Figure 5.11a left and from Figure 5.11b right.

smaller than the expected decay from quenching effects, as will be seen in Chapter 6. These measurements are the first ever OH PLIF high pressure measurements in a coflow diffusion

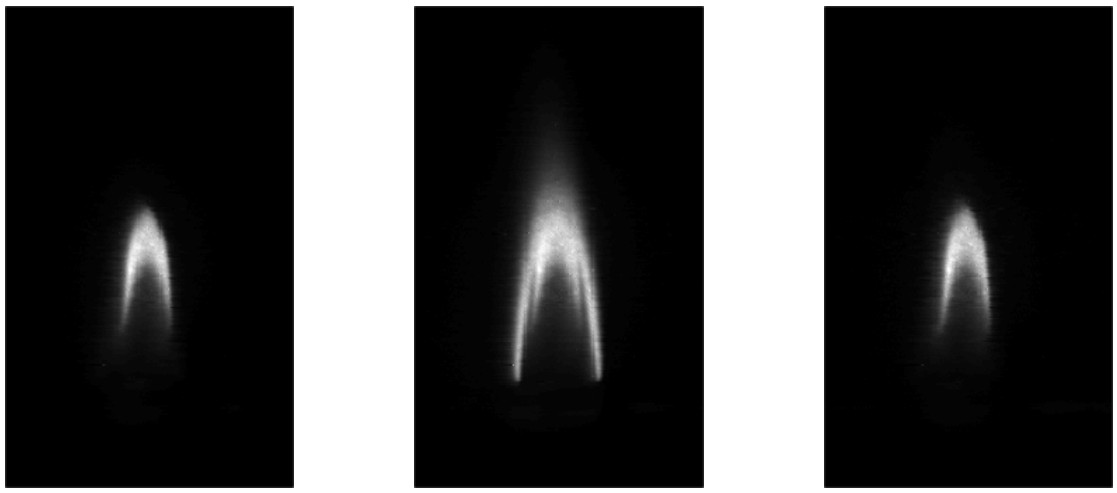

(a) Int. scan first gray zone. (b) Int. between gray zones. (c) Int. scan second gray zone.

Figure 5.13: Frequency filtered integrated scan at 8.9 bar.

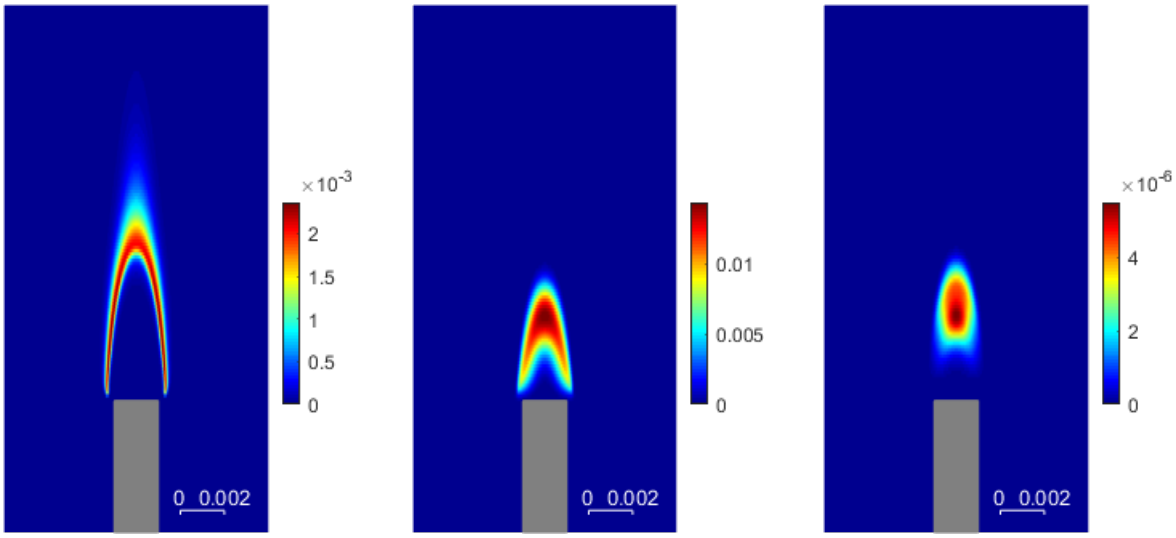

(a) OH. (b) Acetylene C_2H_2. (c) Pyrene $C_{16}H_{10}$.

Figure 5.14: Mole fraction simulations of OH, C_2H_2, $C_{16}H_{10}$ at 8.9 bar.

non-premixed flame and represent state of the art in signal to noise ratio achievable in non-premixed high pressure conditions. The fluorescence decay shows negligible contribution from OH absorption, but LII and soot absorption become very important. Extrapolating this results for a non-premixed system is complicated due to the residence time being an important factor in soot formation, but the results point out the importance of quantifying the soot contribution when doing OH measurements in high pressure non-premixed systems.

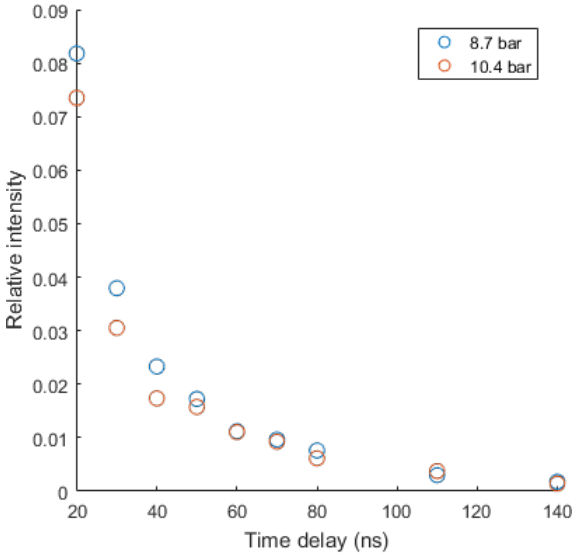

Figure 5.15: Time resolved LII decay.

The overall contribution can be reduced by reducing the laser power, which is complicated due to the reduced quantum fluorescence yield and overlap integral effects at higher pressures. The excitations scans show the SNR that would be associated with single shot measurements for PLIF at the higher pressures due to LII interference. The integrated frequency filtered scans provide information of the relative position of the LII signal to the OH fluorescence at high pressures, the soot burnout coincides with the OH fluorescence signal and goes beyond the high flame temperature region which corresponds to the inner core of the OH signal. Acetylene and Pyrene are known as significant soot markers and fail to represent the experimental profile found, although a more detailed soot formation model and soot transport model would be needed for direct comparison. All the measurements are consistent with previous publications from similar coflow flames although they do not report fluorescence measurements. The experimental data set offers an opportunity to compare chemical kinetic simulations and transport model with a high pressure dataset.

Chapter 6

OpenFOAM simulations of a high pressure non-premixed coflow flame

The goal of this chapter is to compare the results from Chapter 5 with a numerical CFD simulation. The OpenFOAM [52, 53] platform is used to simulate a laminar co-flow non-premixed flame at the pressure conditions used in the experiment. OpenFOAM is a free, open source CFD software, with the mission of offering a community supported long term reliable CFD code. OpenFOAM has been modified and used for combustion purposes in several works [54, 55]. This Chapter describes the fundamentals of OpenFOAM briefly and focuses on the modifications for this particular simulation.

6.1 Conservation equations

The conservation equations used in OpenFOAM are given here; a more detailed description and assumptions can be found in [52].

- Continuity and species continuity.

$$\frac{\partial \rho}{\partial t} + \vec{\nabla} \cdot (\rho \vec{u}) = 0 \tag{6.1}$$

$$\frac{\partial (\rho Y_k)}{\partial t} + \vec{\nabla} \cdot (\rho Y_k (\vec{u} + \vec{V_k})) = \dot{w}_k \tag{6.2}$$

- Momentum equation

$$\frac{\partial (\rho \vec{u})}{\partial t} + \vec{\nabla} \cdot (\rho \vec{u} \vec{u}) = -\vec{\nabla} p + \rho \vec{g} + \vec{\nabla} \cdot \vec{\tau} \tag{6.3}$$

- Energy equation

$$\frac{\partial (\rho h_s)}{\partial t} + \vec{\nabla} \cdot (\rho \vec{u} h_s) = \dot{w}_T + \frac{Dp}{Dt} + \dot{\nabla} \cdot (\lambda \vec{\nabla T}) \tag{6.4}$$

6.2 Transport properties

6.2.1 Viscosity

The transport properties in the chemical mechanisms use the Leonard-Jones parameters, to obtain viscosity and thermal conductivity for the different species. The current OpenFOAM 4.0 version lacks the implementation to use those values to calculate transport properties. The current ReactingFoam module uses the Sutherland model for a viscosity that is dependent on temperature.

$$\mu = \frac{A_s \sqrt{T}}{1 + \frac{Ts}{T}} \tag{6.5}$$

A Cantera interface with Python and Matlab is used to fit the different viscosity profiles from the Leonard Jones parameters. A fit to a nonlinear function (lsqcurvefit) is used with

the air coefficients as initial conditions ($A_s = 1.67212 \times 10^{-6}\ \frac{kg}{ms\sqrt{K}}$, $T_s = 170.672\ K$), for each species and each chemical mechanism. For the PAH mechanism described later, the transport data was not available, and the transport data from a previous iteration of the chemical model was used [51]. The fitted transport data for GRI-mech can be found in Appendix C. The mixture viscosity properties are calculated by a mass fraction weighted average, instead of more accurate multicomponent calculations or Wilkes formula for the averaged viscosity. Nevertheless, the averaging method provides sufficiently accurate results.

6.2.2 Diffusion coefficients

The current OpenFOAM version does not allow to use binary diffusion coefficients, and an assumption has to be made to obtain mass diffusivities from the viscosity calculations. The default OpenFOAM configuration obtains the mass diffusivity from the assumption:

$$Sc = \frac{\mu}{\rho D} = 1 \tag{6.6}$$

To understand the assumption, for a non-premixed diffusion methane flame, the Schmidt number as a function of temperature is calculated for a methane-air diffusion coefficient (D) with air and methane as bath gas ($\mu\ \rho$). In Figure 6.1 the Schmidt number as a function of temperature in both the richest and leanest sides of the non-premixed flame is shown, and within the flame, the Schmidt number is not expected to have substantial variations from the values shown. Based on these determinations, a $Sc = 0.7$ is chosen as a better approximation for this particular fuel.

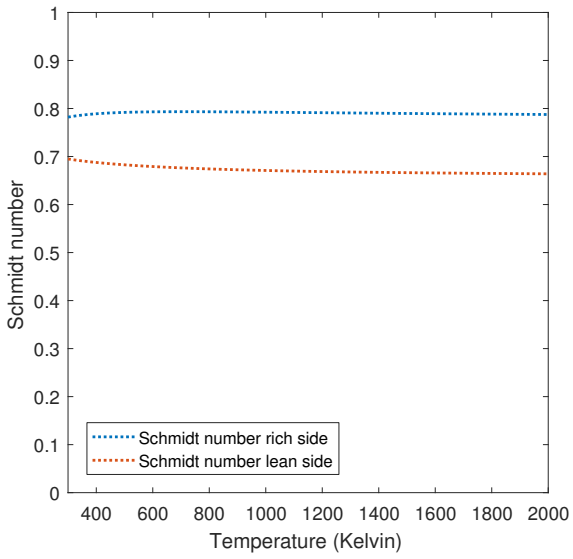

Figure 6.1: Schmidt number.

6.2.3 Thermal conductivity

From Champman-Enskog theory, it can be seen that viscosity and thermal conductivity depend similarly on the same collision integral; the thermal conductivity can be inferred from viscosity. The thermal conductivity is calculated with the modified Eucken formulation [56] which is appropriate when the viscosity is well known.

$$f_{Eu} = \frac{\lambda_0 M}{\eta_0 C_{V,m}} = 1.32 - 1.77 \left(\frac{R}{C_{V,m}} \right) \tag{6.7}$$

The previous equation is valid for diluted mixtures. In OpenFOAM equation 6.7 is applied for each species, and then the mass weighted average is used for the mixture properties.

6.2.4 Thermodynamic properties

The thermodynamic properties are included in each mechanism in the form of NASA polynomials which have the form [57]:

$$\frac{C_{p,k}(T)}{R_u} = \sum_{i=1}^{5} a_{i,k} T^{q_i} \tag{6.8}$$

The q_i values are 0, 1, 2, 3 and 4.

$$\frac{H_k(T)}{R_u T} = \frac{b_1}{T} + \frac{\int C_{p,k}(T) dT}{RT} \tag{6.9}$$

$$\frac{S_k(T)}{R_u} = b_2 + \int \left(\frac{C_{p,k}(T)}{RT} \right) dT \tag{6.10}$$

The values b_1 and b_2 are integration constants. These are also given in the tables.

6.3 Mesh and Boundary conditions

Figure 6.2 and Table 6.1 show the mesh blocks, mesh size, and number of cells; blocks 6, 7, and 8 have nonuniform spacing in the radial direction to reduce the computational time for a bigger cell size further from the flame sheet. The mesh size in the flame region has been chosen to be in the same order of magnitude as the resolution obtained in the experimental configuration. The overall dimensions are 2×4 cm, and the angle of the section is 5°. The time step and the mesh size has been selected to produce results that don't change when decreasing the time step to $\Delta t = 5$ μs, or doubling the number of cells in both the radial and axial direction. The procedure for each simulation has three steps.

- Step 1: Using as initial conditions the domain filled with (76% N_2 24% O_2 by mass), and the boundary conditions that are shown in Table 6.2, except with $T = 800$ K for

methane flow, methane tube, and air flow to ignite the flame. Each simulation is run until steady state is reached, with a single step mechanism, as described in section 6.4. An adjustable time step is used for this case:

$$\Delta t = 0.1 \frac{1}{\left(\frac{u_x}{\Delta x} + \frac{u_y}{\Delta y}\right)} \tag{6.11}$$

- Step 2: Using as initial conditions the steady state solution of step 1, and boundary conditions from Table 6.2, with the single step mechanism described in section 6.4 and fixed time step $\Delta t = 10\ \mu s$.
- Step 3: Using as initial conditions the steady state solution of step 2 with boundary conditions from Table 6.2, compute a solution with the desired more complete chemical mechanism with a fixed time step $\Delta t = 10\ \mu s$.

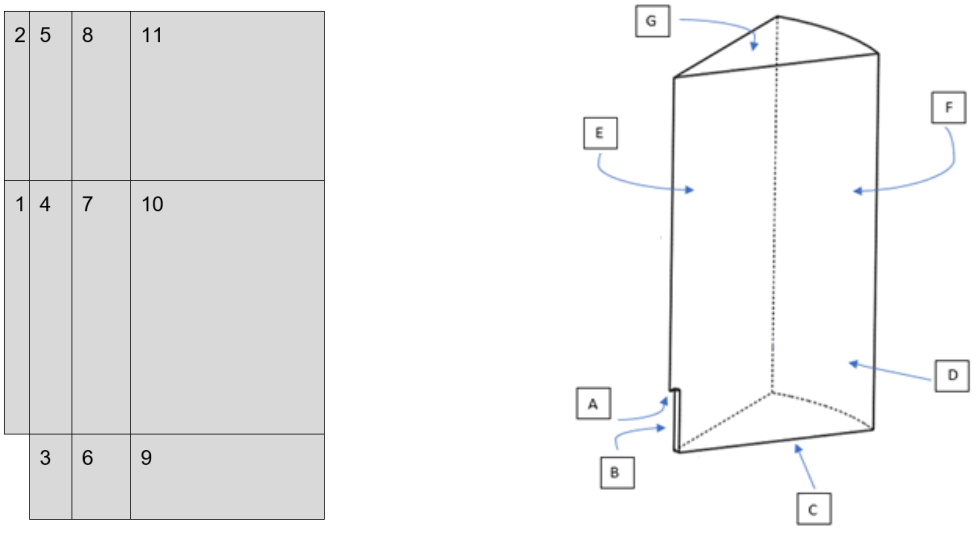

(a) Mesh sections.

(b) Face labels.

Figure 6.2: OpenFOAM mesh.

	Block dimensions (mm)	Number of cells	Cell dimensions (μm)
Block 1	1×18	3600 (30×120)	33.3×150
Block 2	1×12	1200 (30×40)	33.3×200 to 33.3×400
Block 3	6×6	7200 (180×40)	33.3×150
Block 4	6×18	21600 (180×120)	33.3×150
Block 5	6×12	7200 (180×40)	33.3×200 to 33.3×400
Block 6	3.8×18	1800 (45×40)	56.1×150 to 112.3×150
Block 7	3.8×18	5400 (45×40)	56.1×150 to 112.3×150
Block 8	3.8×12	1800 (45×40)	56.1×200 to 112.3×400
Block 9	9.2×6	2400 (60×40)	153.3×150
Block 10	9.2×18	7200 (60×120)	153.3×150
Block 11	9.2×12	2400 (60×40)	153.3×200 to 153.3×400

Table 6.1: Mesh dimensions.

	Mesh face	Velocity	Pessure	Temperature
Methane flow	1A	Fully developed $V_{avg} = 0.15\ \frac{m}{s}$	Zero gradient	Uniform $T = 310\ K$
Methane tube	3B	No-slip	Zero gradient	Uniform $T = 310\ K$
Air flow	3C & 6C	Top-hat $V = 0.15\ \frac{m}{s}$	Zero gradient	Uniform $T = 310\ K$
Burner rim	9C	No-slip	Zero gradient	Zero gradient
Side flow	9F, 10F & 11F	Zero gradient	Zero gradient	Zero gradient
Top flow	2G, 5G, 8G & 11G	Zero gradient	Uniform $P = 1\ bar$	Zero gradient

Table 6.2: Boundary conditions.

6.4 Chemical mechanisms

- GRI-Mech 3.0 & GRI-Mech 3.0 with excited species: The GRI-Mech 3.0 [58] is the reference mechanism for methane chemistry in combustion; it is a mechanism that includes 5 elements ($O,\ H,\ N,\ C$ & Ar) and has 325 reactions and 53 species. The mechanism has been optimized for methane combustion in the temperature range $1000\ K - 2500\ K$ and equivalence ratios from 0.1 to 5. The conditions studied here, non-premixed system and pressures above $P = 10\ bar$, are not far from the optimization range and being a detailed mechanism implies a better performance outside of the optimized span. The GRI-Mech with excited species is a slight variation from the one used in [10], using GRI-Mech 3.0 instead of 2.2.

- DRM-19 and DRM-22: are two sets of elementary reactions reduced from GRI-Mech [59], which were thought with the objective of developing a smaller set of reactions to reproduce closely the main combustion characteristics predicted by the full mechanism (GRI-Mech) to reduce computational time.

- PAH mechanism: A variation of the kinetic mechanism (93 species and 729 reactions) found in [4] is used here [60], that was developed to predict the formation of poly-aromatic hydrocarbons (PAH) and the growth of up to five aromatic rings in C_1 and C_2 fuels such as methane and ethylene. The model is based on the $C_0 - C_2$ chemistry. This is the most up to date PAH formation mechanism and has been used as a basis for soot inception. This mechanism is specially important to represent the carbon sink that large PAH represent at high pressures in the non-premixed coflow flame.

6.5 Results and discussion

To evaluate the contribution of each parameter, including the number of OH molecules interacting with the laser, temperature, quenching, and overlap integral, the following values are calculated for each pressure, based on the theoretical description from Chapter 5.

$$OH\ mol. = \sum_{cells} \frac{P_{cell}}{T_{cell}} \chi_{OH} \tag{6.12}$$

$$Temperature\ eff. = \frac{1}{OH\ mol.} \sum_{cells} T_{eff} \cdot \frac{P_{cell}}{T_{cell}} \chi_{OH} \tag{6.13}$$

$$Q_{inteff} = \frac{1}{OH\ mol.} \sum_{cells} Q_{eff} \cdot \frac{P_{cell}}{T_{cell}} \chi_{OH} \tag{6.14}$$

$$Overlap\ int. = \frac{1}{OH\ mol.} \sum_{cells} Overlap_{eff} \cdot \frac{P_{cell}}{T_{cell}} \chi_{OH} \tag{6.15}$$

$$Sim\ fluo. = \sum_{cells} \frac{P_{cell}}{T_{cell}} \left(\chi_{OH} T_{eff} Q_{eff} Overlap_{eff} \right) \tag{6.16}$$

$OH\ mol.$ is the number of molecules interacting with the laser sheet, $Temperature\ eff.$ represents the effects of temperature in the simulated fluorescence signal, Q_{inteff} is the quenching effects in the simulated fluorescence signal, $Overlap\ int.$ is the broadening effects in the simulated fluorescence signal, and $Sim\ fluo.$ is the overall fluorescence signal.

Figure 6.3, 6.4, and 6.5 compares the spatial distribution of the fluorescent OH with the simulated fluorescence using the GRI, DRM, and PAH mechanisms. The simulated and the experimental fluorescence have a good qualitative agreement. It is important to point out that the flame height is matched very well throughout all the pressures; this is due to the mass flow rate constant in all the cases, so while the diffusion coefficient decreases as pressure increases the convective axial velocity decreases at the same rate producing a constant flame height. The simulated model fails to reproduce several important details in the experimental results.

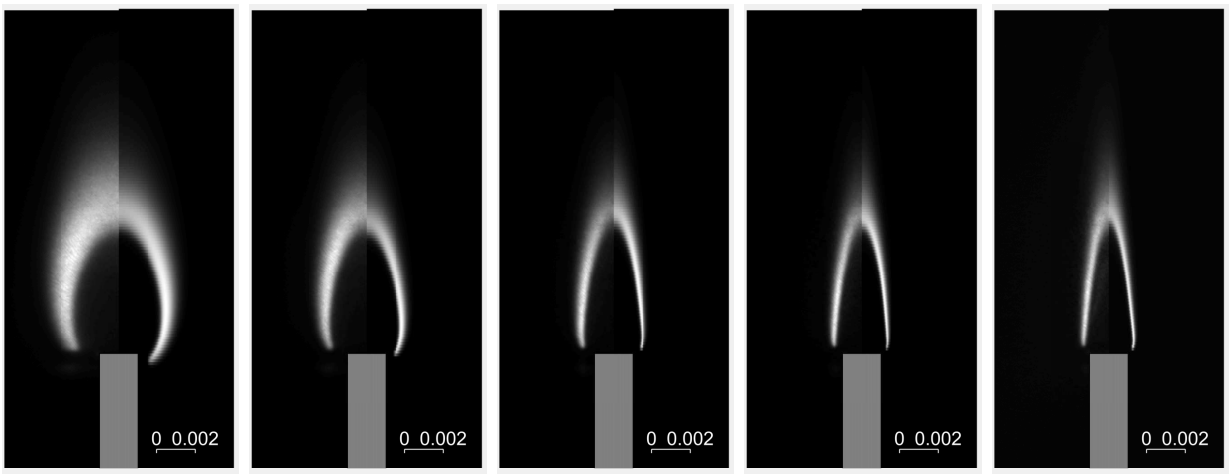

(a) 1.4 *bar*. (b) 3.3 *bar*. (c) 5.7 *bar*. (d) 8.9 *bar*. (e) 11.1 *bar*.

Figure 6.3: Experiment (left side) vs GRI-mech simulated fluorescence (right side).

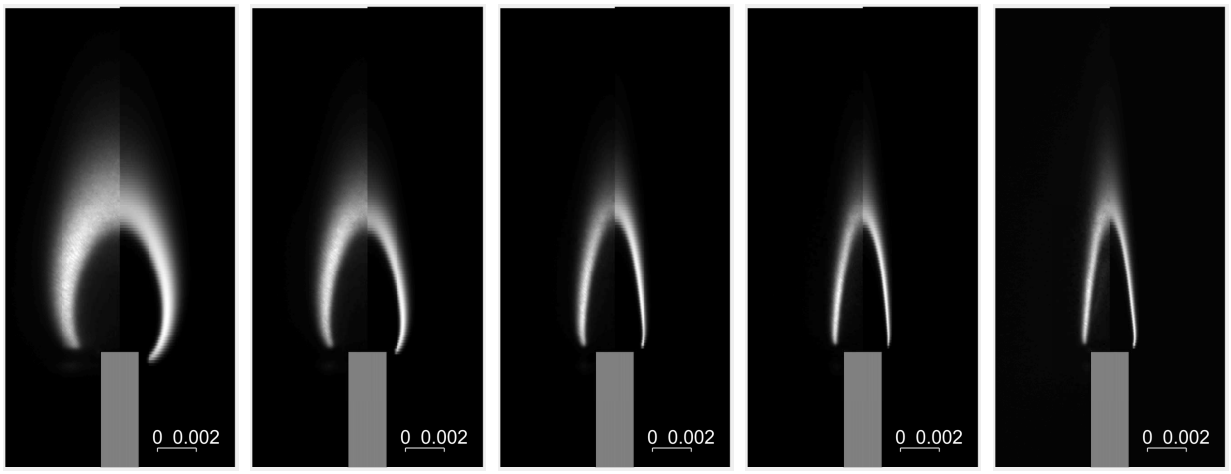

(a) 1.4 *bar*. (b) 3.3 *bar*. (c) 5.7 *bar*. (d) 8.9 *bar*. (e) 11.1 *bar*.

Figure 6.4: Experiment (left side) vs DRM simulated fluorescence (right side).

- The flame base in the 1.4 *bar* case is not predicted properly; this is probably due to difficulties in the modeling of low temperature chemistry for the flame initiation and near the burner wall (T_{burner} constant at all the pressures). On the other hand, the base of the flame lifts as the pressure increases, which is a phenomenon that is also seen in the experiment.

- The overall OH thickness is underpredicted by the simulation; this can also be seen in [61] in a counterflow configuration, which suggests that OH consumption rates might

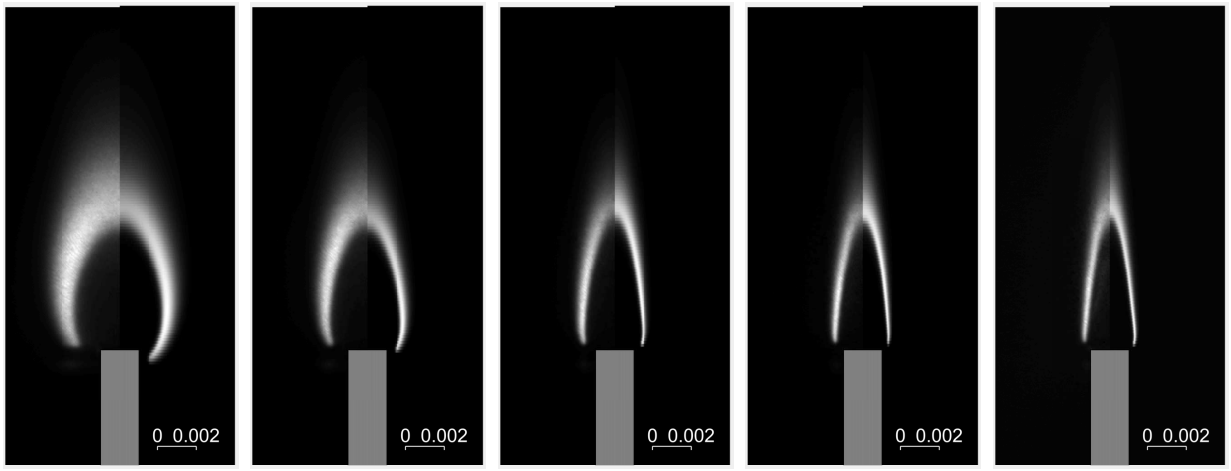

(a) 1.4 *bar*. (b) 3.3 *bar*. (c) 5.7 *bar*. (d) 8.9 *bar*. (e) 11.1 *bar*.

Figure 6.5: Experiment (left side) vs PAH-mech simulated fluorescence (right side).

be overestimated. The overall qualitative trend is again consistent, as the overall reaction layer thickness decreases with pressure, both in simulation and experiment. This pattern can be explained due to the smaller thickness of the mixing layer and the reduced OH diffusivity.

The three mechanisms share similar qualitative distributions with very subtle differences. The differences between the DRM and the GRI mechanisms are negligible, but the PAH mechanism has differences that become bigger as the pressure increases, at 11.1 *bar* the tip of the flame has a relatively higher intensity, and the flame thickness is greater.

Figure 6.6 shows an equivalent of OH molecules present at a given moment that are interacting with the laser sheet, see Equation 6.12. To retrieve the total number of OH molecules at a given moment, it would be necessary to add the symmetric convolution which would increase the number of molecules at lower pressures since the reaction zone stands further from the symmetry axis. There is no clear dependence of the OH molecules as a function of pressure. Both detailed chemical mechanisms agree quantitatively with a small difference at 11.1 *bar* where the DRM19 mechanism has a higher number of molecules. On the other hand, the skeletal mechanism over-predicts both of the detailed mechanisms by 14%-18%

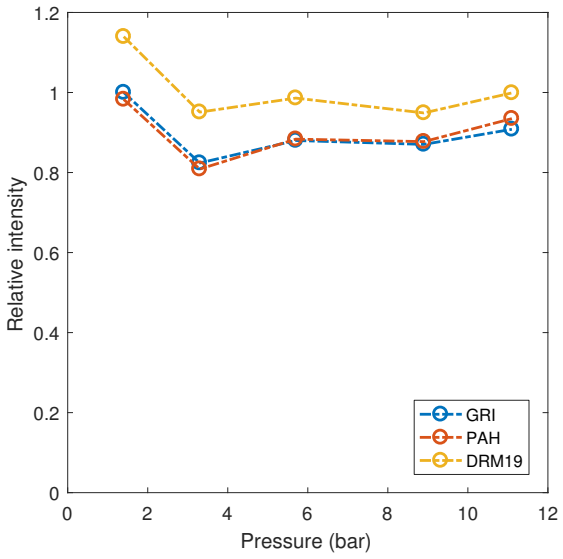

Figure 6.6: OH mol. mechanism comparison.

throughout all the pressures. The trend of the other mechanisms is also represented in the skeletal mechanism, which suggests that the pressure effects are captured in the skeletal mechanism but misses some key reactions that lead to the absolute disagreement. The OH distribution seems to be independent of the PAH production as the PAH mechanism, and the GRI-mech mimic the results up to 8.9 bar, with a small difference at 11.1 bar. This small difference suggests that the effects of soot formation on OH are relatively low for the OH chemistry, despite the fact that relatively high carbon to soot conversion rate (5%) have been reported in similar configurations at 10 bar [14].

Figure 6.7 shows the effects of the different corrections for each mechanism studied, see Equations (6.12)-(6.16) . The highest contribution is accomplished by the quenching correction, which as expected has an approximate dependence as $Q \propto \frac{1}{P}$. The second most important effect is the overlap integral. As the transitions broaden, the dependence on pressure becomes weaker. The temperature correction decreases slightly, as the average temperature where OH exists increases, as high pressure increases dissociation decreases, the energy not consumed for dissociation reactions increases the peak flame temperature.

Figure 6.8 compares the overall simulated fluorescence signal of the three different mech-

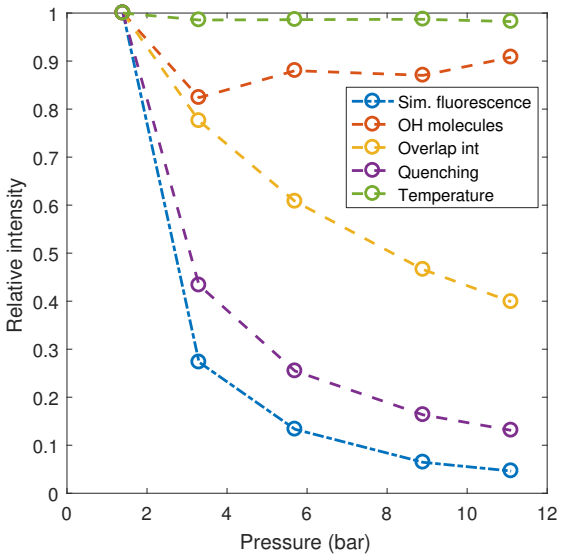

(a) GRI-mech fluorescece parameters.

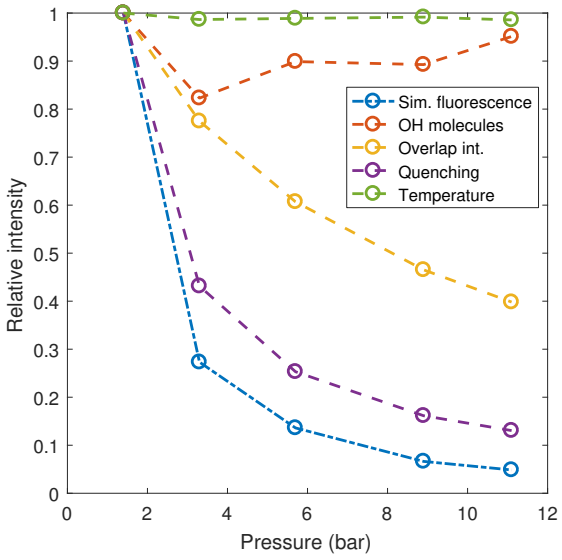

(b) PAH-mech fluorescece parameters.

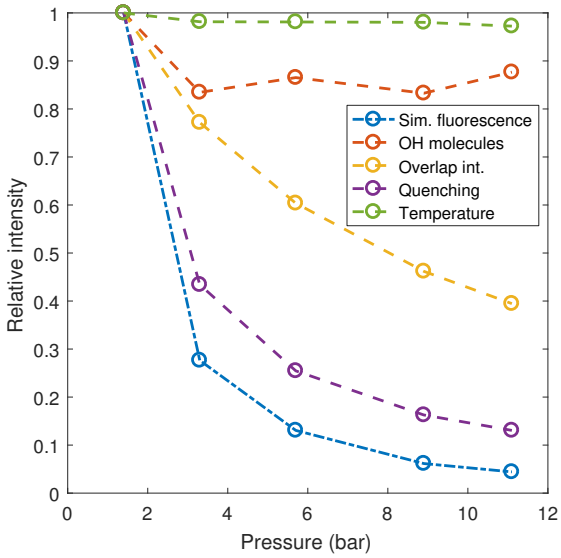

(c) DRM19-mech fluorescece parameters.

Figure 6.7: Mechanism fluorescence parameters.

anisms with the experimental results. The results are normalized to the highest pressure point; the assumptions such as steady state fluorescence are reached faster and are more accurate at higher pressures. The simulation and the experiment agree qualitatively in the decay. The match is good for 3.3 *bar*, 5.7 *bar*, 8.9 *bar* and 11.1 *bar*. Assuming that the normalization at 11.1 *bar* is accurate, there is a 100% discrepancy at 1.4 *bar*; this can be explained by a combination of effects. The choice of laser intensity is complicated due to

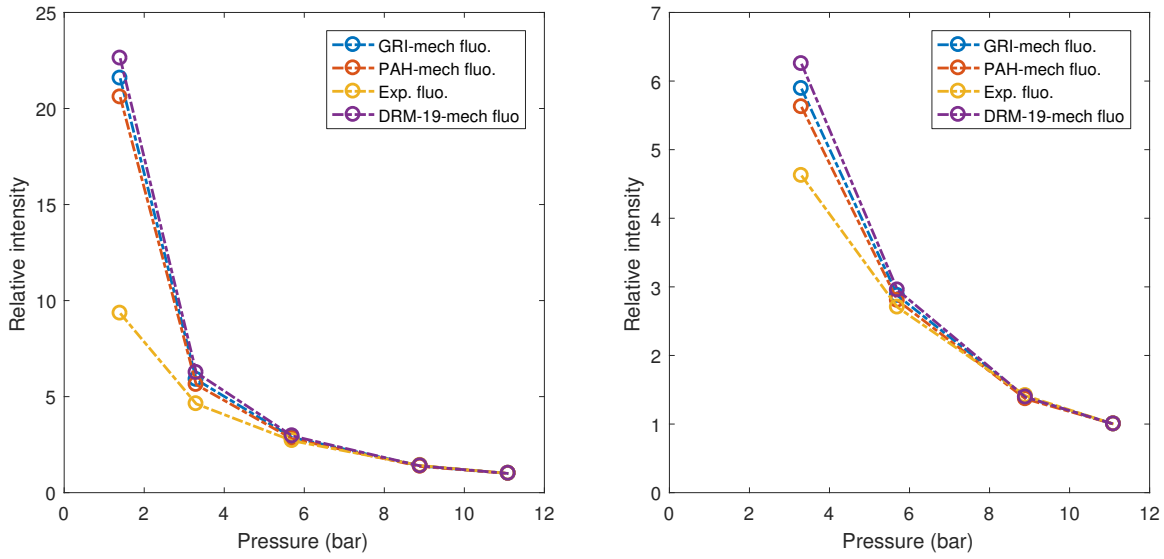

(a) All pressures. (b) Excluding (1.4 *bar*).

Figure 6.8: Integrated fluorescence vs integrated simulation fluorescence.

the dynamic range associated with a decay in the intensity by a factor of 20 throughout the pressures. In order to maximize SNR the laser intensity choice is a compromise to the linear dependence at the lowest pressure, and hence the fluorescence decay time for 1.4 *bar* is non-negligible in the nanosecond time scale. To maximize the filtering of the LII signal, it is important to minimize the gate window time, and this could affect the fluorescence collection efficiency. The mechanism that is closest to the experiment is the PAH mechanism that stands as the most updated which includes the contribution of PAH formation.

6.6 Conclusions

This Chapter aims to compare trends of the experimental OH fluorescence signal as pressure increases, with a numerical CFD simulation that matches the experimental conditions and allows comparison of different chemical mechanism and transport datasets. The simulated fluorescence and the experimental dataset is compared in 2 aspects.

- The spatial distribution of the OH molecule. The numerical simulation has an excellent agreement matching the OH layer position and the overall flame height; this flame height is mostly driven by the diffusion coefficients. The simulations fail to quantitatively match the thickness of the OH layer, transport, and chemical effects are convoluted, in the flame thickness calculation, on the other side, the overall flame heights are matched accurately, suggesting that the issue could be on the chemical mechanisms. The flame base is not matched, specifically, at low pressures, more accurate modeling of the boundary conditions could narrow the differences; also, low temperature chemistry is known to be challenging, especially when mixing is dominated by diffusion.

- The comparison in the trends of the number of OH molecules as pressure increases. All the mechanisms capture the same qualitative trend as the pressure increases, but the skeletal mechanism has a 20 % higher number of OH molecules compared with the detailed mechanisms. This result reflects that the number of OH molecules present in the studied flame does not strongly depend on pressure. Furthermore, pressure does not have a significant impact on the overall number of OH molecules that interact with the laser sheet. The comparison between the experimental results and the three simulations is good in the high pressure region, and the agreement is similar to the only similar study in a counterflow flame [43]. The use of a 2D configuration for quantitative evaluation is challenging, in particular for this case where the variation of OH is small to the corrections applied, although excellent agreement in the overall trends is observed.

Chapter 7

Nanosecond N_2 broadband coherent anti-Stokes Raman spectroscopy

Coherent anti-Stokes Raman spectroscopy (CARS) has been studied for the last decade in laser diagnostics for combustion [19]. CARS is a Raman based technique that generates a coherent signal at:

$$w_{as} = w_{pr} + w_p - w_s \tag{7.1}$$

The simplest experimental setup is the one involving one coherence $w_p - w_s$, and is the most commonly used in combustion, as follows:

$$w_1 = w_{pr} = w_p \tag{7.2}$$

$$w_2 = w_s \tag{7.3}$$

$$w_3 = 2w_1 - w_2 \tag{7.4}$$

The laser interacts with the medium through a third order nonlinear susceptibility giving rise to an oscillating polarization at w_3. Adjustment of the $w_1 - w_2$ to a particular Raman resonance permits different molecules to be examined. The nonlinear susceptibility is both temperature and number of molecules dependent on the relative population of the vibrational and rotational states. Therefore, temperature measurements are based on the spectral signature and concentrations are based on the overall intensity of the signal; in some particular regimes, the spectral line shape can be sensitive to concentration. There are several advantages of CARS versus other diagnostics presented here. One of the biggest advantages of CARS is the increased S/N ratio due to its coherent or laser-like signal, and the possibility of spatially separating the signal that we are looking for from isotropic background interferences. Another advantage is the signal dependence with intensity to the power of three; this permits a reasonable signal strength even with a small third order nonlinear susceptibility cross section, as will be seen in Chapter 8, the development of ultrafast lasers has further enhanced the use of this nonlinear intensity dependence.

7.1 Background

A classical derivation of the CARS signal as a function of the susceptibility is given here [19]. Beginning with the wave equation:

$$\nabla^2 \vec{E} + \frac{1}{c^2} \frac{\delta^2 \vec{E}}{\delta t^2} = -\mu_0 \frac{\delta^2 \vec{P}}{\delta t^2} \tag{7.5}$$

$\vec{E}$ is the electric field, c is the speed of light, μ_0 the free space permeability and $\vec{P}$ the polarization vector. Assuming a sinusoidal time dependence of the electronic wave of the form, $\exp^{-iw_j t}$:

$$\nabla^2 \vec{E}(w_j, \vec{r}) + \frac{w_j^2}{c^2} \vec{E}(w_j, \vec{r}) = -\mu_0 w_j^2 \vec{P}(w_j, \vec{r}) \tag{7.6}$$

Solving for the electric field, it is possible to find:

$$I_3 = \frac{w_3}{(n_1^2 \cdot n_2 \cdot n_3 \cdot c^4 \epsilon_0^2)} I_1^2 \cdot I_2 \cdot |\chi_{CARS}|^2 \cdot l^2 \cdot \left(\frac{\sin(\frac{\Delta k_l}{2})}{(\frac{\Delta k_l}{2})} \right)^2 \tag{7.7}$$

Where n_1, n_2, n_3 are the index of refraction at frequencies w_1, w_2, w_3; ϵ_0 is the vacuum permittivity, and l the probe volume length. The CARS signal is a function to the power of three with laser intensity, and function of the susceptibility to the power of two. The susceptibility is approximately linear with density. The maximization of the overall function leads to $\Delta k_l = 0$, the so-called phase matching condition and is defined as:

$$\Delta k_l = 2\Delta\vec{k}_1 - \Delta\vec{k}_2 - \Delta\vec{k}_3 \tag{7.8}$$

7.1.1 Phase matching

For combustion in order to obtain the highest spatial resolution, it is highly desirable to reduce beam overlap, and this can be accomplished by the BOXCARS configuration. The challenge of this configuration is that it increases experimental complexity and requires a specific spatial distribution of the laser beams to maximize the signal.

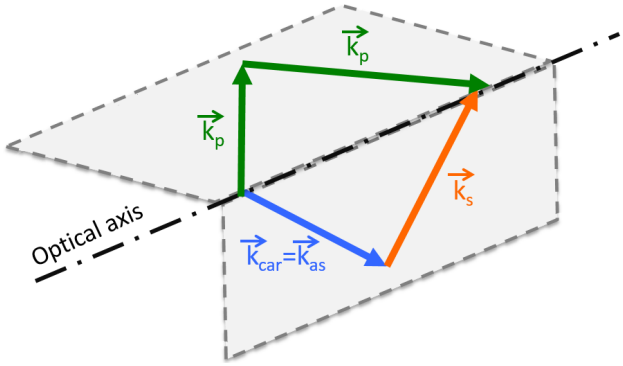

Figure 7.1: Phase matching.

This condition comes from the previous derivation.

$$0 = 2\Delta\vec{k}_1 - \Delta\vec{k}_2 - \Delta\vec{k}_3 \tag{7.9}$$

The simplest method to apply the condition is to project the k vectors into the x, y, and z directions and assume constant refractive index for different wavelengths. For clarity w_1 will be split in 1.1 and 1.2 to represent the pump and probe beams.

$$0 = w_1 \sin(\theta_{1.1}) - w_1 \sin(\theta_{1.2}) \tag{7.10}$$

Projection in the y axis:

$$0 = w_2 \sin(\theta_2) - w_3 \sin(\theta_3) \tag{7.11}$$

Projection in the z axis:

$$0 = w_2 \cos(\theta_2) - w_3 \cos(\theta_3) + w_1 \cos(\theta_{1.1}) - w_1 \cos(\theta_{1.2}) \tag{7.12}$$

We have four unknowns with three equations; from the x axis it is easy to see that $\theta_{1.1} = \theta_{1.2}$ and then the easiest way to solve the problem is fix these angles and find θ_2, θ_3 from the y and the z projection.

7.2 Experimental setup

The light source used is a Nd:YAG laser used to pump a custom made broadband dye laser with a diluted concentration of Rhodamine 640 for both the amplifying and the oscillating cells, a polarizer is placed before the amplifying cell to obtain polarized light after the

amplifying stage. A combination of convex plus concave lenses collimates the laser beam. For the pump beam, there is a delay stage to match the pump and Stokes beams temporally. After the energy conversion from a 150 mJ Nd:YAG laser at 532 nm, the energies at the probe volume are 15 mJ for pump and probe and 9 mJ for the Stokes beam. The three beams are focused using a 177 mm focal length lens and recollimated to another 177 mm focal length lens. The CARS signal is collected with a collimator into an optical fiber, then into a 1 m spectrometer in combination with a Pixis 2K camera (Princeton instruments).

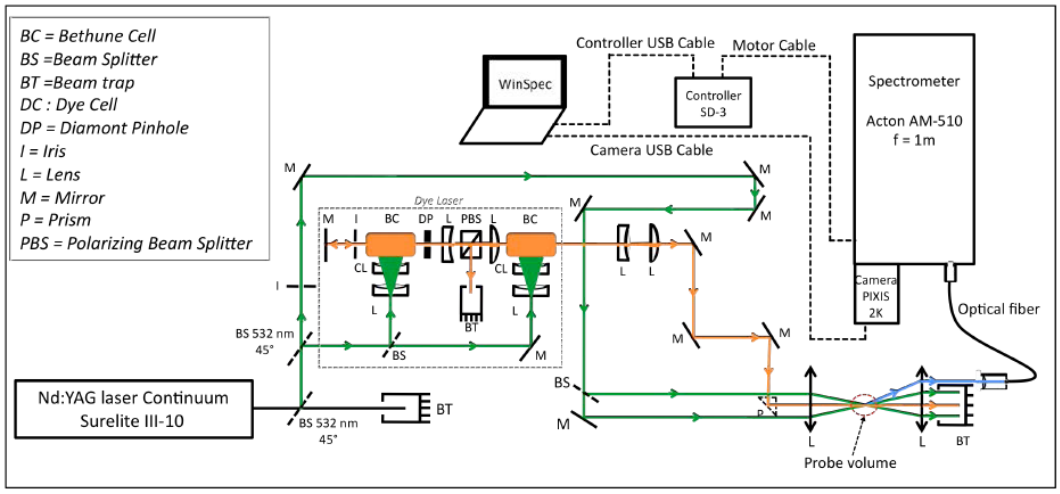

Figure 7.2: Experimental setup for N_2 broadband CARS.

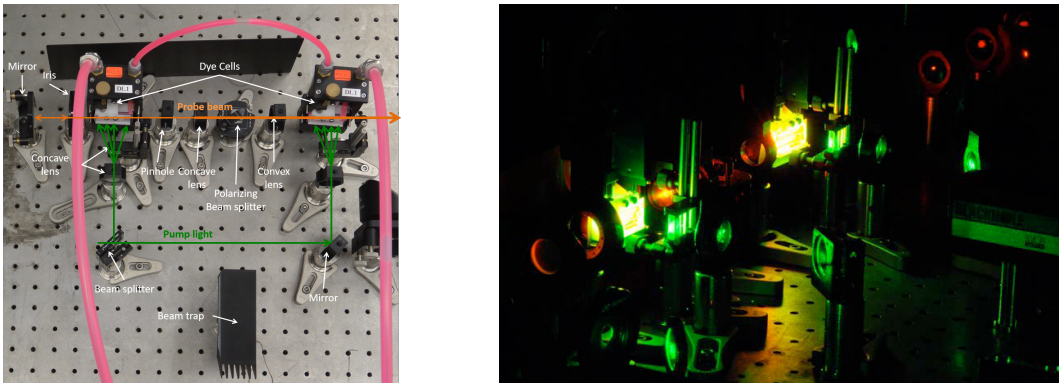

Figure 7.3: Broadband dye laser.

7.3 Results and discussion

Figure 7.4 shows the CARS spectrum of the first vibrational band of Nitrogen; there is no population of the upper vibrational state due to the low temperature, and the rotational lines are not resolved due to the instrument, pump and Stokes line-width. As can be seen in Figure 7.4b the instrument line-width dominates, and no broadening effects can be observed in the spectra for up to 9.5 *bar*. The CARS *signal* $\propto P^2$, and the integrated signal under the curve of Figure 7.4a follows this dependence, due to its susceptibility dependence, and the signal does not show any non-resonant contribution.

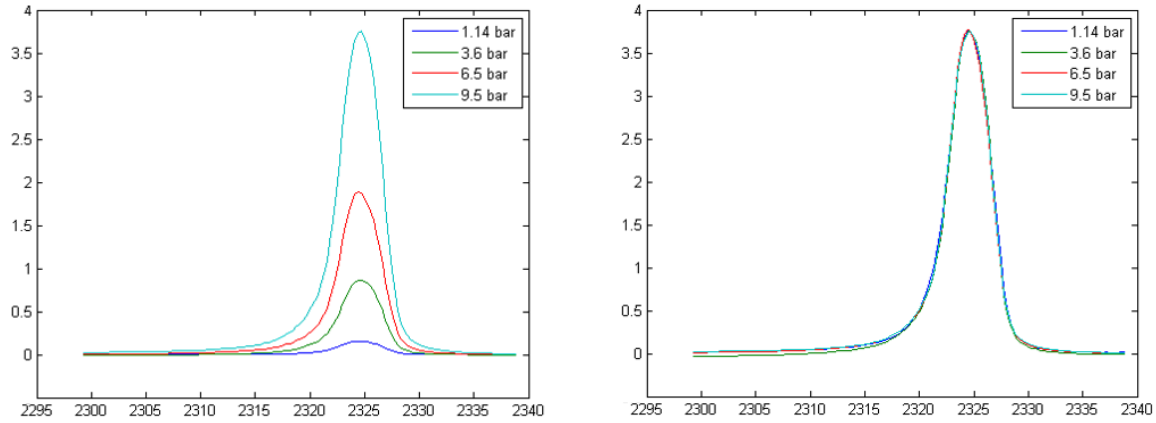

(a) Intensity vs $\nu(cm^{-1})$ (b) Normalized intensity vs $\nu(cm^{-1})$

Figure 7.4: 21°C CARS spectrum.

The measurements were repeated for 100°C and 200°C, but the change does not produce any qualitative change in the spectrum since rotational transitions are not resolved. Under high temperature conditions, laser induced breakdown occurred. This phenomenon was also seen in [5], and is probably due to decomposition of some chamber material which reduces the laser induced breakdown threshold, for example, the plastic o-ring sealing from the windows. The spectrum is fitted using CARSFIT [62]. CARSFIT uses a least squares method to fit the CARS spectrum. Table 7.1 reports some significant values found from the calibration fit, fixing the temperature.

Fitting variables	Value
Wavenumber expansion	1.00002
Probe line width (FWHM)	2.97 cm^{-1}
Pump line width (FWHM)	0.75 cm^{-1}

Table 7.1: CARSFIT parameters.

7.4 Conclusions

Temperature measurements at pressures of up to 9.5 *bar* are demonstrated in a calibration cell. Broadening effects are not observed due to the rotational transitions not being resolved at the temperatures studied. This preliminary study supports the use of nanosecond N_2 vibrational CARS at higher pressures. Understood limitations of nanosecond CARS such as increased non-resonant background contributions have to be studied individually due to the dependence on the collisional partners, and local environment.

Chapter 8

Hybrid fs/ps pure-rotational coherent anti-Stokes Raman scattering

Coherent anti-Stokes Raman scattering (CARS) is a powerful non-intrusive diagnostic tool of combustion science. This technique is widely used for temperature and species determination because of its high precision and robust applicability in harsh combustion environments [63, 64, 65, 66]. Limitations associated with traditional ns-CARS, include low repetition rate and interference from non-resonant background signals. Recently, the development of femtosecond CARS has made it possible to realize kilohertz measurement rates without the complication of a non-resonant background [67, 68, 69, 70]. To overcome the low spectral resolution offered by broadband femtosecond (fs) lasers, a hybrid combination of broadband excitation and picosecond (ps) narrow-band detection has been developed. Hybrid fs/ps pure-rotational CARS (HRCARS) has been successfully used for single-shot temperature and species measurements even under highly sooting hostile environments [71, 72, 73, 74]. 1D and 2D imaging with HRCARS for flame thermometry have also been reported [75, 76, 77]. The theoretical modeling of hybrid fs/ps pure-rotational CARS has been developed, and the effects of pressure, probe pulse shape, and chirp of pump/Stokes pulses are discussed

[72, 78, 79, 80, 81]. This chapter describes a HRCARS experiment of N_2 at room temperature using different probe chirps. Probe chirp effects on HRCARS are investigated by fitting the experimental spectra with an in-house developed model, and the effect caused by the probe pulse chirp is discussed.

8.1 Background

A brief description of the semi-classical theory employed to model HRCARS is given here, following the diagram shown in Figures 8.1. To prepare the rotational coherence, a broadband femtosecond laser is used to produce a pump (ω_1) and a Stokes (ω_2) pulse that covers several rotational states. After a delay T_2, the prepared coherence is probed by a picosecond narrowband probe laser pulse (ω_3). The third order polarization is given by [82]:

$$P^{(3)}_{Res}(t,T_1,T_2) = (\frac{i}{\hbar})^3 \int_0^\infty dt_3 \int_0^\infty dt_2 \int_0^\infty dt_1 [R(t_3,t_2,t_1) E_3(t-t_3) E_2^*(t+T_2-t_3-t_2) \\ E_1(t+T_1+T_2-t_3-t_2-t1) \exp[i(\omega_1-\omega_2+\omega_3)t_3] \exp[i(\omega_1-\omega_2)t_2] \exp[i(\omega_1)t_1]] \quad (8.1)$$

Where $E_1(t)$, $E_2(t)$ and $E_3(t)$ represent the electric field envelopes for pulses 1, 2 and 3, and $R(t_1,t_2,t_3)$ represents the third order response function. Following the derivation from [79], it is possible to simplify Eq. 8.1 for the specific experimental realization; in this case pulses 1, 2, and 3 are far from any direct electronic resonances, and it is safe to assume that during the intervals t_1 and t_3 the effective molecular dephasing is very small with respect to the dephasing during t_2. Hence, the only terms that will survive the (RWA) are those involving $(w_1 - w_2)$ and then evolving during t_2. Furthermore we will be set up so that $T_1 = 0$ experimentally, and under this assumption, is possible to simplify Eq. 8.1 to:

$$P^{(3)}_{Res}(t,T_2) = (\frac{i}{\hbar})^3 E_{probe}(t) \int_0^\infty dt_2 [R(t_2) E_2^*(t+T_2-t_2) E_1(t+T_2-t_2) \exp[i(\omega_1-\omega_2)t_2]] \quad (8.2)$$

The Raman response of N_2 is given by [83]:

$$R(t_2) = \sum_{v} \sum_{\Delta J=2} I_{v,JJ'}(t_2) \exp[(-i\Omega_{v,JJ'} - \Gamma_{v,JJ'})t_2] \tag{8.3}$$

Here the summation is taken over populated vibrational levels v and all the S-branch rotational transitions between J and J' ($\Delta J = 2$), which have the Raman frequencies $\Omega_{v,JJ'}$. The Raman linewidth $\Gamma_{v,JJ'}$ caused by collisional dephasing is negligible when the probe delay is smaller than the collisional lifetime, and the $N_2 - N_2$ Raman line-widths are added to the simulation using the tables found in [84]. Using these tables has been proved to be more effective than using traditional models such as MEG and ECS [85, 86]. $I_{v,JJ'}(t_2)$ are the corresponding Raman transition strengths. Both $\Gamma_{v,JJ'}$ and $I_{v,JJ'}(t_2)$ can be calculated with the constants recommended by Martinsson et al [87], and the Raman transition strength contains information from the Boltzmann distribution which is temperature sensitive. With a Fourier transform from Eq. (8.2) the CARS signal is finally given by:

$$I_{CARS}(\omega, T_2) \propto \mid P^{(3)}_{Res}(\omega, T_2) \mid^2 \tag{8.4}$$

In this case, the contribution from $P^{(3)}_{NR}(\omega, T_2)$ is also negligible due to the delay T_2 being sufficiently large to avoid any contribution from the non-resonant background, and this is one of the main advantages of this HCARS approach.

8.2 Chirp modeling

The structure of N_2 S-branch Raman transitions is shown in Figure 8.2. The rotational Raman signal exhibits a periodic structure in time caused by the molecular alignment introduced by the femtosecond pulse. At $t = 0$, the isotropic molecular ensemble is aligned to the linearly polarized direction of the femtosecond pulse. Therefore the rephasing angular

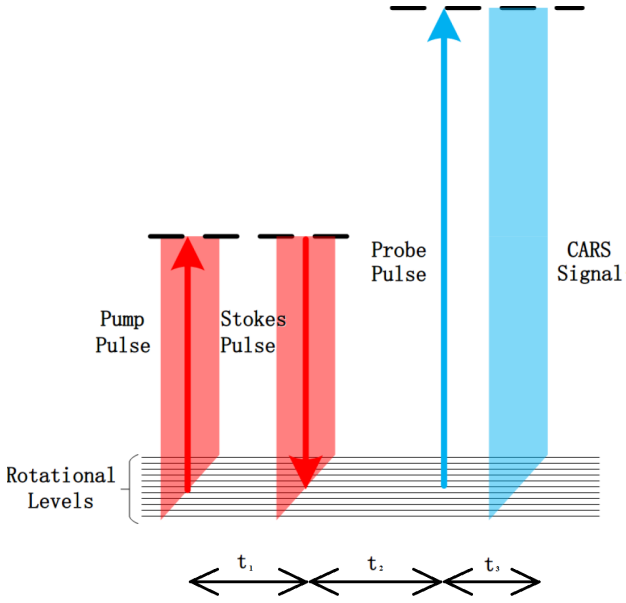

Figure 8.1: (HCARS) diagram.

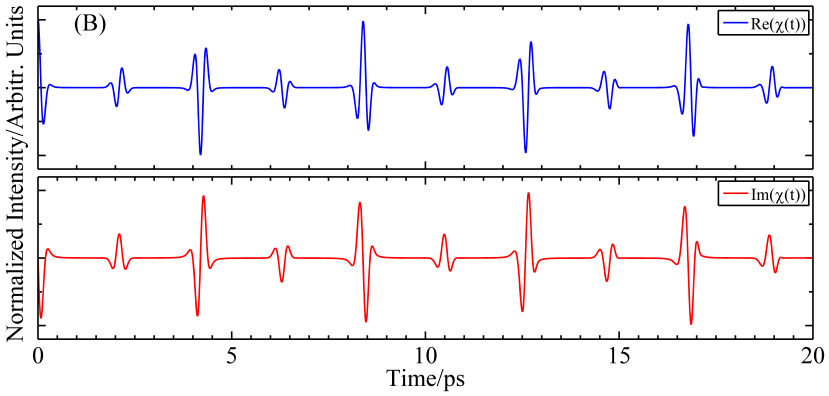

Figure 8.2: Real and imaginary susceptibility.

frequency of each rotational state J is given by $\Omega_J = (1/2)J(J+1)\Omega_1$, where $\Omega_1 = 4\pi B_0 c$ is the fundamental rephasing frequency [88]. The revival period of the molecular ensemble is given by $\tau_{full} = 2\pi/\Omega_1$. For N_2 ($B_0 = 1.998$ cm^{-1}). As shown in Figure 8.2 the period τ_{full} is equal to 8.38 ps. For S-branch pure-rotational Raman transitions, the Raman wavenumber in Eq. 8.5 is given by $\Omega_{v,JJ'} = \Omega_{J+2} - \Omega_J$, and during a complete recurrence the relative phase accumulation is $(4J+6)\pi = 0$. At the half recurrence, all transitions accumulate a relative phase of $(2J+3)\pi = \pi$. However, at the quarter recurrence, the accumulated relative

phase $(J + 3/2)\pi$ is $-\pi/2$ and $\pi/2$ for odd J and even J respectively. There is a similar but reverse situation at $3/4\ \tau_{full}$ [78]. This opposite phasing of odd and even J transitions results in a destructive interference between them. N_2 has a 2:1 in the ratio degeneracy factor for even and odd rotational states so this interference will distort the spectra of odd transitions when the probe pulse is chirped. Because of the previous effect, it is of particular significance to model accurately any magnitude of the probe pulse chirp and understand it in detail. A Gaussian probe pulse with linear chirp can be written as [89]:

$$E_{probe}(t_2) = A\exp[-\frac{(2\ln 2)t_2^2}{t_p^2}]\exp[-i\frac{(2\ln 2)\alpha t_2^2}{t_p^2} - i\omega_2 t_2] \tag{8.5}$$

$$t_p^2 = t_{p0}^2 \cdot (1 + \alpha^2) \tag{8.6}$$

$$\frac{d\omega}{dt} = \frac{2 \cdot (2\ln 2)\alpha}{t_p^2} \tag{8.7}$$

Where t_p is the FWHM of the probe pulse, α is the linear chirp term, ω_2 the carrier frequency, t_{0p} is the transform limited FWHM pulse duration in intensity, and $\frac{d\omega}{dt}$ is the chirp factor; which represents a more physical understanding of chirp and it will be expressed here in $\frac{cm^{-1}}{ps}$.

Using the index of refraction data from [90, 91], w_1 and w_2 could be assumed as FTL (Fourier transform limited) $t_{10} = 100\ fs$ going through a 25 mm quartz window. This would induce a linear chirp of 1104.02 $\frac{cm^{-1}}{ps}$, or an increase $\frac{t_1}{t_{10}} = 25\ \%$; on the other hand, the picosecond pulse going through the same medium $t_{30} = 3\ ps$ acquires a linear chirp of 0.063 $\frac{cm^{-1}}{ps}$, that only creates an increase of $\frac{t_1}{t_{10}} = 0.1\ \%$. The pulses can be seen in Figure 8.3.

In order to evaluate the effect of the probe chirp, the absolute values of residuals are summed along the frequency axis for each probe delay. This sum of absolute residuals (SAR) is then compared to the equivalent temperature change that would induce such an effect. Figure 8.4 shows a pure N_2 hybrid CARS for a $t_p = 3\ ps$ and $T_2 = 11.4\ ps$, with an instrument line-width of 0.65 cm^{-1}. Figure 8.4a shows the residual from a FTL pulse to a linear chirp

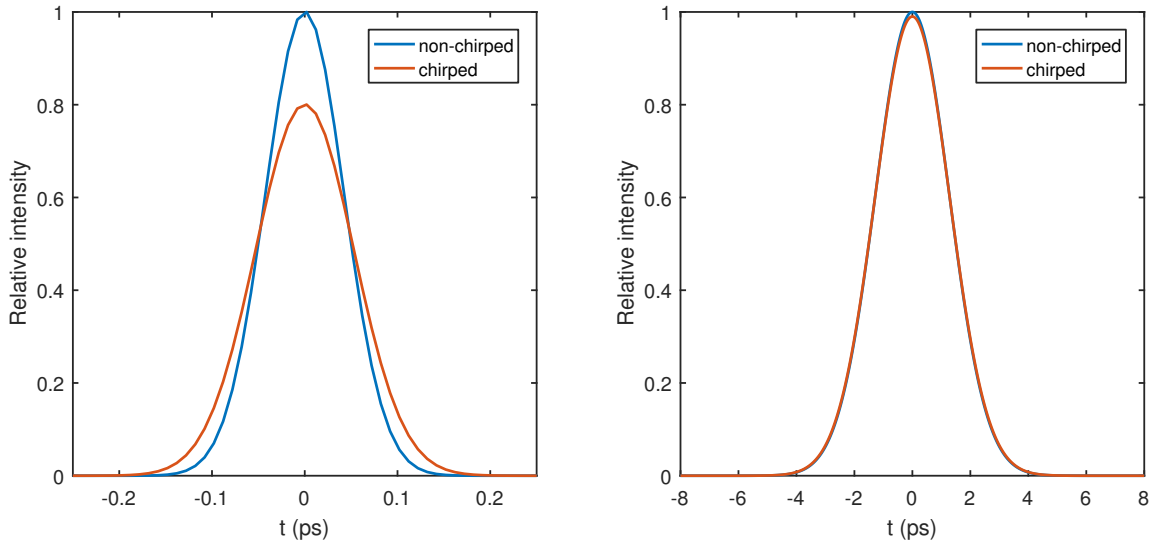

(a) 100 fs through 25mm fused silica. (b) 2 ps through 25mm fused silica.

Figure 8.3: Chirp effects of a 25 mm fused silica window.

of 1 $\frac{cm^{-1}}{ps}$ at $T = 300\ K$. Figure 8.4b shows the residual from a FTL pulse at $T = 300\ K$ to a $T = 346\ K$

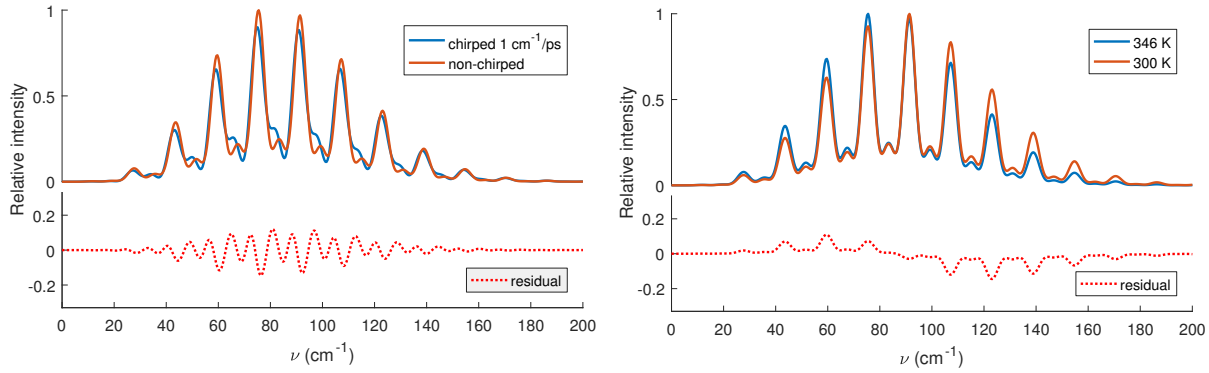

(a) Residual adding linear chirp of 1 $\frac{cm^{-1}}{ps}$. (b) Residual comparing 300 K to 346 K.

Figure 8.4: Matching SAR while changing linear chirp and temperature.

8.3 Experimental setup

In the HCARS experiment a commercial Ti:sapphire amplifier (Coherent Legend Elite Series) provides 100 fs pulses with 1 mJ per pulse at 1 kHz repetition rate. The femtosecond

laser is split by an 80:20 beam splitter, with 80% directed to a second harmonic bandwidth compressor (SHBC) and 20% to the Pump and Stokes pulses. Figure 8.5 shows the SHBC instrument which can generate 1 kHz picosecond pulses with an adjustable 7 cm^{-1} bandwidth at 400 nm. The SHBC is based on the effect reported by [92]. Opposite temporal chirps are introduced to two femtosecond pulses separately and then eliminated by the sum-frequency generation (SFG) process between them. The SHBC instrument is similar to the device reported by [93]. Two cylindrical lenses are used to collimate the beams diffracted by the grating. The lenses placed at $L_1 = f - d_1$ and $L_2 = f + d_2$ introduced positive and negative chirp to the laser respectively, see Figure 8.5. A detuning of d_1 and d_2 equal to each other produces two laser pulses with precisely conjugate chirps. The sum frequency of these two beams generates a narrowband picosecond laser. Unfortunately, because of the aberration caused by mirrors and lenses, it is hard to generate a completely chirp-free laser by SFG. In this SHBC instrument, by adjusting d_1 the residual chirp in the probe pulse can be changed continuously.

The energies obtained at the focal point of the pump and Stokes pulses are 100 μJ at 800 nm, and by the probe laser 50 μJ, with $\sim$ 7 cm^{-1} bandwidth at 400 nm. These beams are focused by a 170 mm spherical lens to achieve a folded BOXCARS phase matching configuration. The HCARS spectra around 400 nm was collected by a 1-meter spectrometer (AM-505) with an 1800 $lines/mm$ grating. The resolution of the PIXIS 2K used is 512×2048 with an approximate instrument line-width of 0.65 cm^{-1}. To maximize the signal level, the polarization direction of probe laser was controlled by a half-wave plate. For all the measurements, the experiments are conducted in the calibration cell described in Chapter 2.

During each set of experiments, a non-resonant HCARS signal of Argon was acquired first at several time delays. By finding the time delay with the maximum signal the initial timing of $t = 0$ was obtained, although this parameter was then fitted due to the errors associated with the finding of a maximum from a Gaussian like pulse. This signal from Argon is used

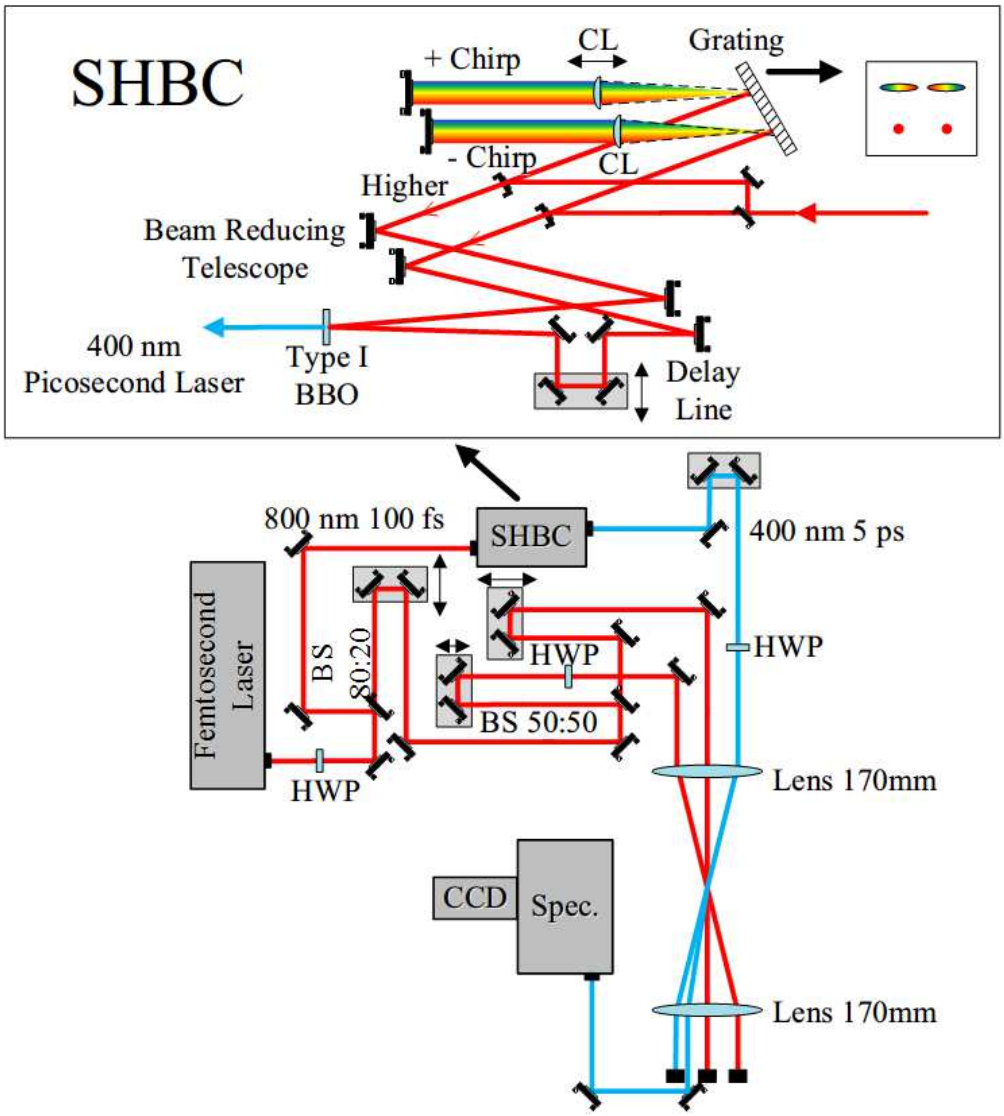

Figure 8.5: (HCARS) experimental setup.

as cross-correlation to measure the probe pulse shape $I(t)$. Because of the finite bandwidth of the pump and Stokes lasers, the non-resonant Argon HCARS signal is used to correct the measured HCARS profile. This term accounts for the convolution effects of $E_2^*(t + T_2 - t_2)$ and $E_1(t + T_2 - t_2)$ in Eq.8.2. The probe delay between the three pulses w_1, w_2 and w_3 is varied by adjusting a manual translation stage in the optical path of the probe laser. To fully depict the spectra in the recurrence period, the increment of the translation stage is set to 160 μm, which is equivalent to 1.067 ps ($\sim 1/8\tau_{full}$). The initial probe delay is set above the FWHM of the probe pulse to avoid contributions from non-resonant signal around 0 ps.

Each spectrum is fit with a least-squares optimization algorithm to fit the experimental data.

8.4 Results and discussion

8.4.1 Chirp effects

Figures 8.6 and 8.7 are showing different fits at different probe delays for two chirped pulses with $-0.95\ \frac{cm^{-1}}{ps}$ and $-1.4\ \frac{cm^{-1}}{ps}$. Figure 8.8 is for a condition that is slightly less chirped, with $-0.65\ \frac{cm^{-1}}{ps}$. It is important to note that the relative effect of a constant $\frac{cm^{-1}}{ps}$ chirp is higher for a longer pulse; since the equivalent FTL would have a smaller bandwidth, and also, it means a higher amount of absolute chirp. The method for fitting each of the delays is to free the parameters of: linear chirp, $T_2 = measured + \delta$, the stretch of the x and y axis, the shift of the y axis, and temperature. The initial guess for the minimum root square optimization is based on the measured T_2 with δ free, stretch parameters set to 1, shift set to 0 and the temperature measured by the thermocouple. This procedure is repeated for each time delay, and after that, an average value is found for all the parameters. The new average value is set for temperature, shift, and x stretch, y stretch, and δ are left free, δ being bounded to $\pm 0.1\ ps$, to account for experimental errors in the translation stage.

The most striking aspect of the spectra shown in Figure 8.6 are the time delays $T_2 = 6.11\ ps$ and $T_2 = 10.38\ ps$, and for Figure 8.7 the time delay $T_2 = 7.99\ ps$ and $T_2 = 12.26\ ps$. Both of those spectra correspond to delays of $T_2 \sim 8.4\ ps$ and $T_2 \sim 12.6\ ps$ to the short pulses (femtosecond pump and Stokes), the difference is attributable to experimental errors in the measured probe pulse shape (maximum measured intensity) and the absolute time of the femtosecond pulses. The delays $T_2 \sim 8.4\ ps$ and $T_2 \sim 12.6\ ps$ are characteristic because, as has been explained, this delay corresponds to the molecular alignment of nitrogen at a relative phase of 0 and π. At these specific delays, the pulse wings interact with the molecular

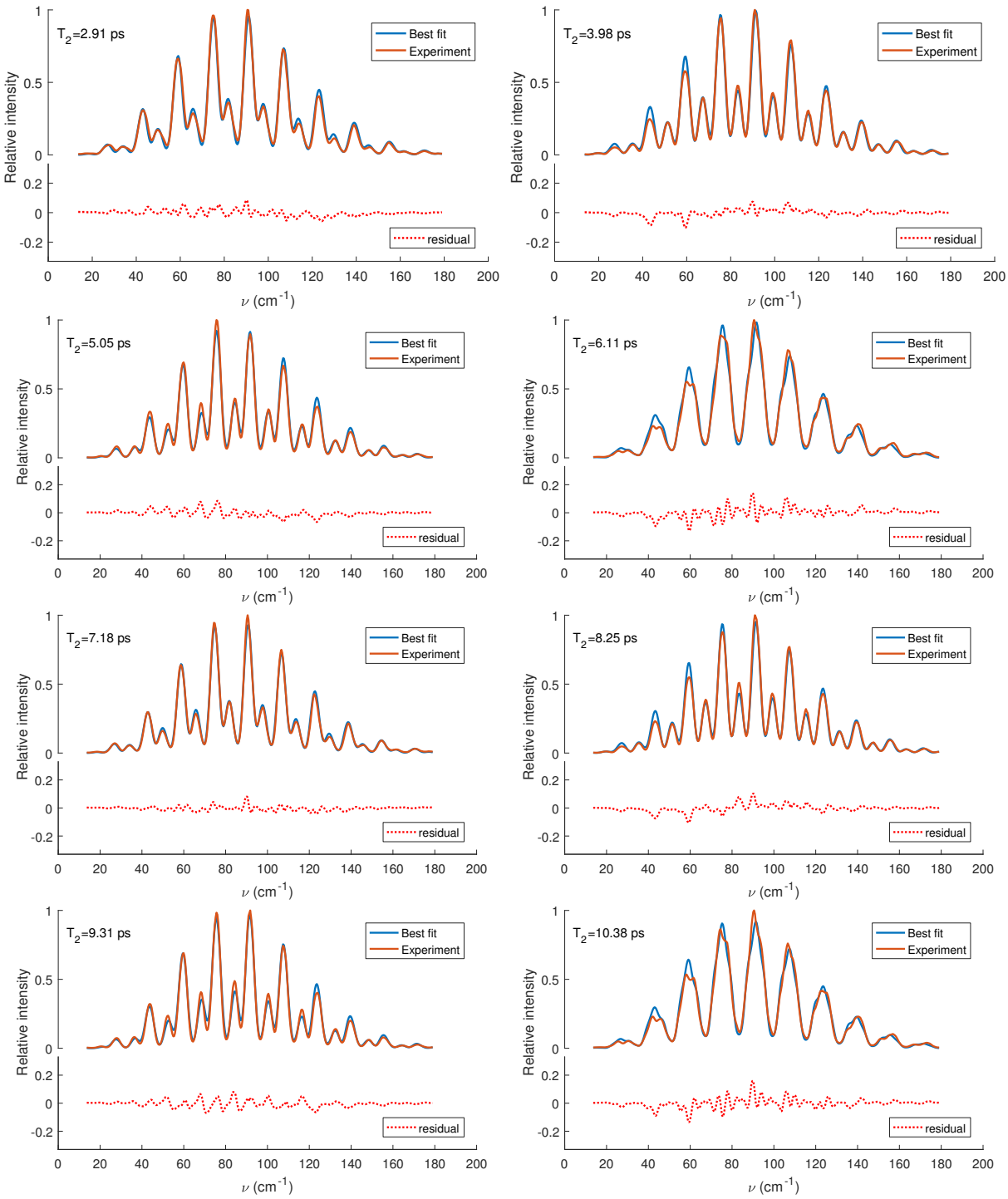

Figure 8.6: $-0.95\ \frac{cm^{-1}}{ps}$ FWHM 5.3 ps.

ensemble at opposite phases $+\pi/2$ and $-\pi/2$, as can be seen in Figure 8.2. This interaction combines chirp effects with destructive interference due to opposite phases with a Raman shift and creates uncommonly seen nitrogen spectra such as the one seen at T_2 for Figure

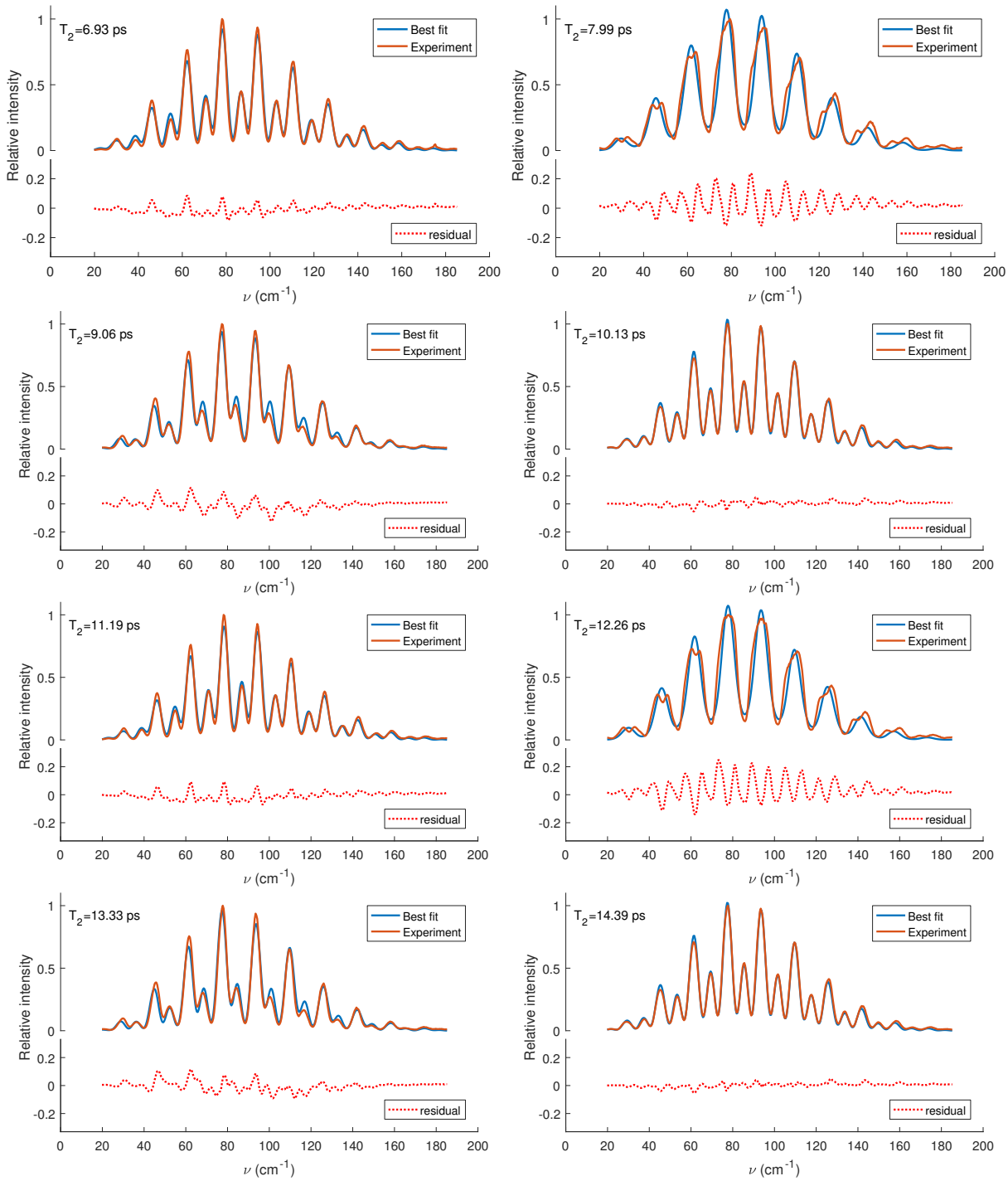

Figure 8.7: $-1.4\ \frac{cm^{-1}}{ps}$ FWHM 5.3 ps.

8.6. This interaction is susceptible to both chirp and probe pulse shape.

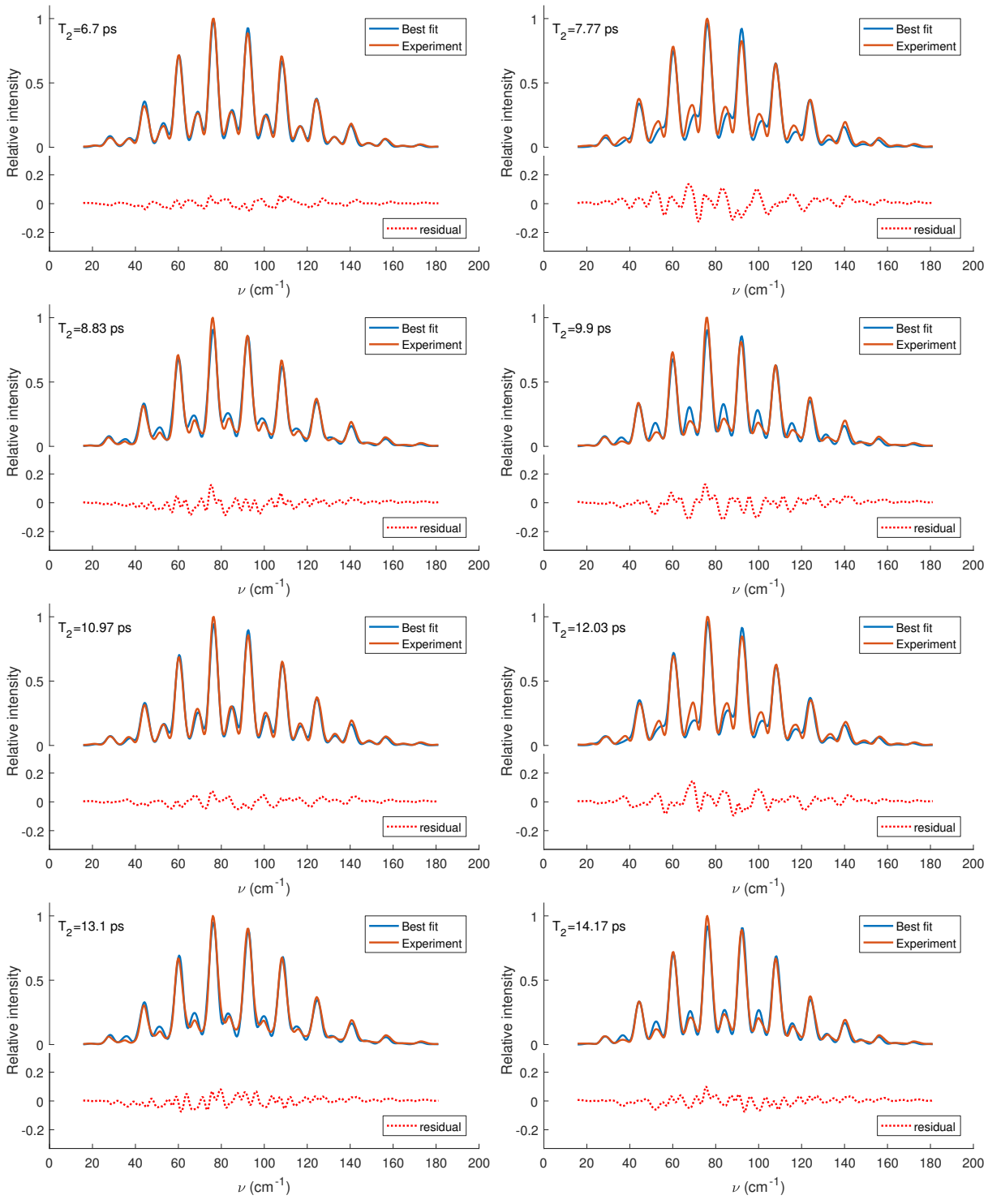

Figure 8.8: $-0.65\ \frac{cm^{-1}}{ps}$ FWHM 4 ps.

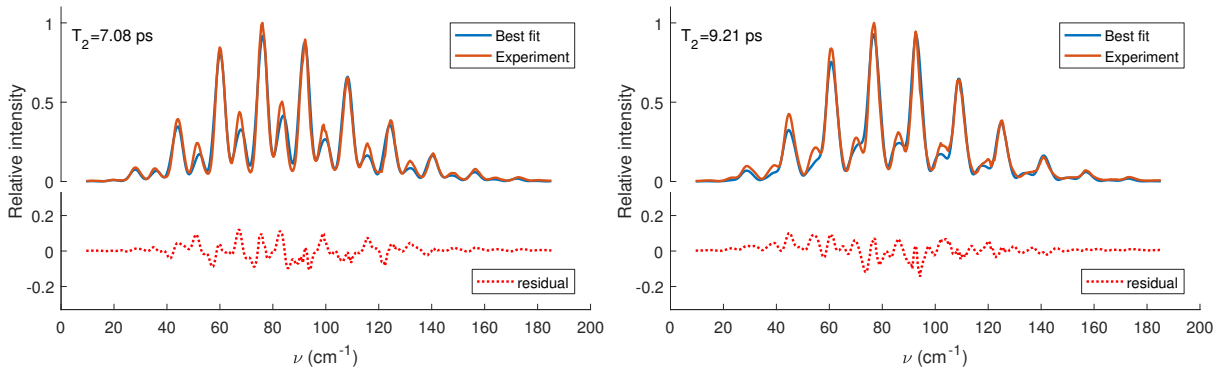

Figure 8.9: $-0.66\ \frac{cm^{-1}}{ps}$ FWHM 5.7 ps and measured $T = 298\ K$.

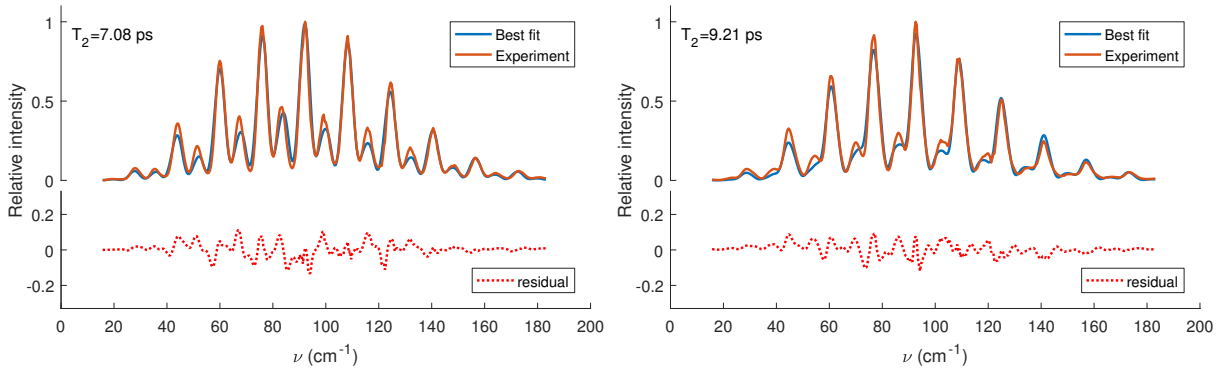

Figure 8.10: $-0.66\ \frac{cm^{-1}}{ps}$ FWHM 5.7 ps and measured $T = 398\ K$.

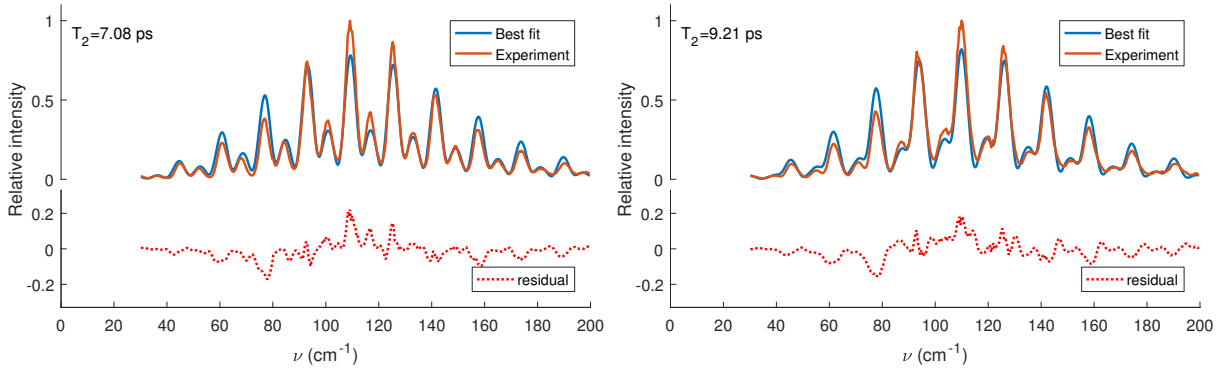

Figure 8.11: $-0.76\ \frac{cm^{-1}}{ps}$ FWHM 7.5 ps and measured $T = 498\ K$.

8.4.2 Temperature effects

Figures 8.9, 8.10 and 8.11 correspond to CARS spectra for the same probe pulse with FWHM 5.7 ps) for 3 different temperatures from 298 K to 498 K (from thermocouple measurements) to best fits ranging from 287 K to 505 K. The chirp fits at these 3 different temperatures

are ($-0.66\ \frac{cm^{-1}}{ps}$ $-0.66\ \frac{cm^{-1}}{ps}$ and $-0.76\ \frac{cm^{-1}}{ps}$)

The overall fitting procedure is the same as the one described before. The results show consistency in the chirp value for the three different temperature conditions, with a small increase in value for the highest temperature; this effect could be attributed to small changes in the probe pulse during the experiment, as well as possible high order chirp effects. The fit quality decreases with increasing temperature due to the bandwidth of the pump and Stokes, magnifying the experimental errors from the newly populated high J rotational transitions; this correction effect can be seen in Figure 8.12. Overall we can observe a qualitative shift in the experimental and theoretical spectra towards higher Raman transitions, through the use of spectral focusing [80] and shorter femtosecond pulses can help to reduce the bandwidth limitations from the femtosecond pulses.

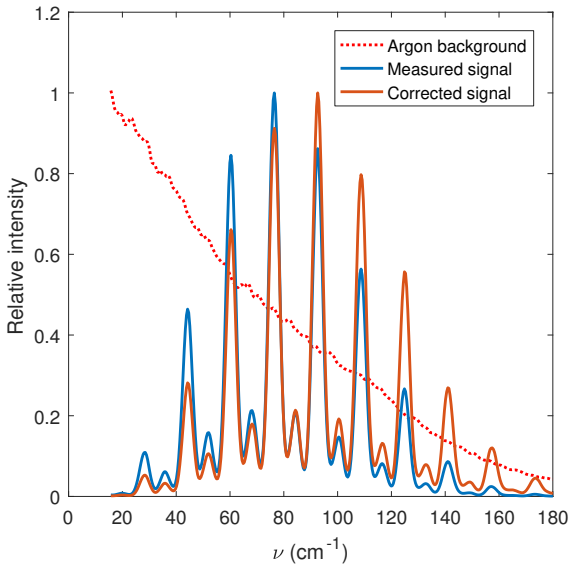

Figure 8.12: Argon background correction.

8.4.3 Pressure effects

Pressure based HCARS measurements are possible both in the time domain and frequency domain. However, the results shown here don't focus on quantitative measurements but

qualitative trends. Figures 8.13 and 8.14, correspond to spectra at different delays T_2 with the same relative position towards the full realignment period, with $\frac{3}{2}\tau_{full} \sim 12.6\ ps$ periods of separation. There are two important aspects: the first one is that given the conditions are the same temperature, the low J transitions have higher Raman line width, so they decay faster. For both pressures, there is a shift (due to normalization) of the intensity towards the high J Raman transitions. The second effect is that Raman linewidth scales linearly with pressure, so at the same time delay for the different pressures, there is also a shift towards Raman transitions with high J.

Figure 8.15 shows the decay in the intensity of the HCARS signal. The decay is computed by integrating the intensity for each delay and doing a linear fit of log (Intensity) vs. delay; the same procedure is applied for the simulation. The qualitative trend is consistent as pressure increases; the dephasing is faster, and the overall signal decays faster. The quantitative match between the experiment and simulation is not very good, but this effect has also been seen in similar BOXCARS configurations, where overall intensity is very strongly dependent on the spatial overlap between the three beams. That is if the alignment is not perfect it is easy to induce a change of spatial overlap as the picosecond beam is scanned.

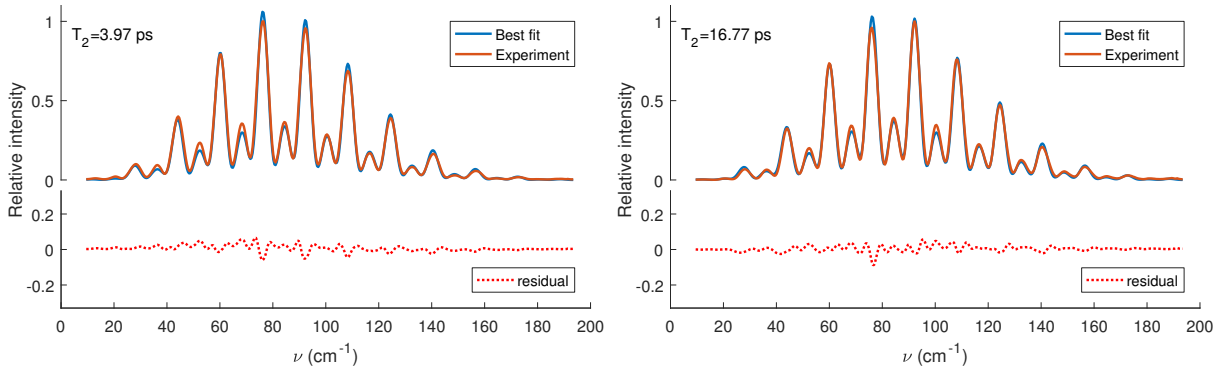

Figure 8.13: $-0.55\ \frac{cm^{-1}}{ps}$ FWHM 4.7 ps 30 psi.

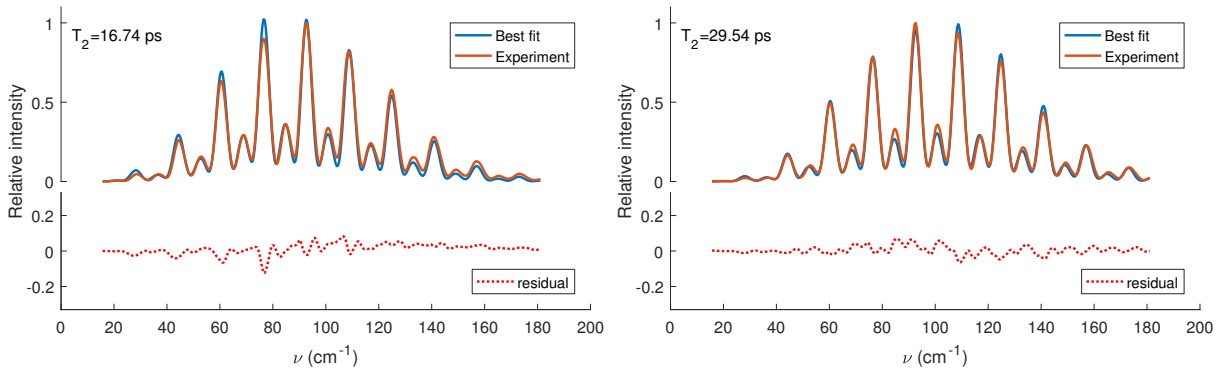

Figure 8.14: $-0.55\ \frac{cm^{-1}}{ps}$ FWHM 4.7 *ps* 95 *psi*.

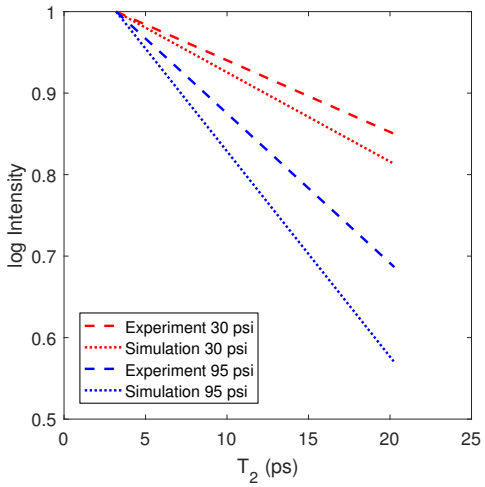

Figure 8.15: Pressure decay 30 *psi* and 95 *psi*.

8.5 Conclusions

The chirp effects can alter the ratio of odd and even transitions of pure N_2 significantly and induce a shift on them. This distortion is more significant at some particular probe delays, the physical mechanism that produces the uncommonly seen N_2 spectrum is understood and described. At these particular probe delays, the effects of chirp are more important. The use of sum frequency to generate picoseconds pulses ($3-4\ ps$) which are ideal for combustion applications (providing good spectral resolution and single shot thermometry capabilities), is particularly sensitive to induce unintentional chirp to the picosecond beam, and chirp has to be quantified to obtain good fits at all probe delays. The use of specific time delays can

help to reduce the sensitivity to chirp effects, in particular, the use of delays multiples of $\frac{\tau_{full}}{4} + \frac{\tau_{full}}{2}n$ reduces the sensitivity of the N_2 HCARS results.

Once the linear chirp is quantified it does not hinder the ability to provide reliable temperature or pressure measurements at any probe delay. The use of HCARS as a pressure measurement in the time domain remains challenging for the BOXCARS configuration due to beam overlap effects, on the other hand, frequency domain measurements are still useful with an accurate modeling of the Raman line width.

Chapter 9

Conclusions and future work

9.1 Conclusions

In this dissertation, a variety of linear and non-linear laser diagnostic techniques have been applied in challenging experimental configurations and under high pressure conditions. The work presented in the previous chapters can be summarized in 2 major areas.

- Two-line OH PLIF thermometry measurements and two-photon CO PLIF measurements in a non-premixed coflow impinging flame configurations with different plate to burner distances, were applied to advance the understanding of flame-wall interactions.
- OH PLIF at a range of pressures ($1 - 11.1$ bar), simulated OH fluorescence from a numerical CFD simulation, nanosecond N_2 vibrational CARS at a range of pressures ($1 - 9.5$ bar) and hybrid fs/ps CARS ($1 - 6.6$ bar) were investigated. This aims to provide an experimental dataset for high pressure combustion models and provide insights into practical challenges in high pressure combustion systems.

The two-line OH PLIF thermometry measurements show that the peak temperature and

the overall averaged OH temperature does not change with plate to burner distance. The results indicate that the wall effects influence the geometry of the OH cloud, as it is forced to open by the boundary layer of the plate. Two-photon CO PLIF measurements confirm the mechanism for increased CO emissions due to the thermo-chemical and fluid mechanical interaction between the plate and the flame. The thermal boundary layer does not allow for the presence of OH nearby the plate proximity, and diffused CO from the flame sheet to the methane core has a pathway to the environment without going through the OH reacting cloud, increasing the CO emissions as the plate is closer to the flame.

The OH PLIF signal is reduced with increasing pressure as the quenching reduces the quantum fluorescence yield and the overlap integral effects reduce the effective absorption of the transitions studied. LII measurements become necessary when pressure increases and for single shot fluorescence measurements. LII could particularly complicate measurements in non-steady conditions due to the need of LII signal subtraction and the time dependence of the LII signal. The OH^* measurements suggest an increase in the chemical reactions that produce OH^* as the pressure increases, the decay of the overall signal is lower than the expected decay from quenching effects. The integrated frequency filtered scans provide information of the relative position of the LII signal to the OH fluorescence at high pressures. The soot burnout coincides with the OH fluorescence signal and seems to go beyond the peak flame temperature region which corresponds to the inner core of the OH signal, they also provide information of the SNR expected as pressure increases for the different flame regions. The SNR decreases as pressure increases. The OpenFOAM numerical CFD simulation shows that the number of molecules interacting with the laser sheet does not increase despite the pressure increase, in part due to the reduced mass diffusion. The simulated fluorescence spatial distribution is in excellent agreement with the experiments regarding the OH cloud position and flame height and fails to match the flame base, in particular at lower pressures; the OH cloud thickness is systematically thinner in the simulations which suggest that either transport or OH consumption needs adjustment. Acetylene and Pyrene are known as

significant soot markers and fail to represent the experimental LII profile found. A more detailed soot formation model would be required to predict the LII signal. Quenching as expected is the highest influence factor in the fluorescence signal followed by the broadening effects. The three mechanisms studied show the same pressure dependence. The use of a 2D configuration for a semi-quantitative evaluation of the OH simulated fluorescence signal is challenging and novel. Nevertheless, remarkable agreement in the overall trend is observed, in particular at higher pressures.

Temperature measurements using nanosecond N_2 vibrational CARS at pressures up to 9.5 *bar* are demonstrated in a calibration cell. These measurements support the use of nanosecond N_2 vibrational CARS at higher pressures. Understood limitations of nanosecond CARS such as increased non-resonant background contributions have to be studied individually due to the dependence on the collisional partners, and local environment.

In hybrid fs/ps N_2 CARS chirp effects can alter the ratio of odd and even transitions significantly and induce a shift on them. This distortion is more significant at some particular probe delays $T_2 = \frac{\tau_{full}}{2}$, the physical mechanism that produces the uncommonly seen N_2 spectrum is understood and described. The use of sum frequency generation to produce picosecond pulses ($3-4\,ps$), is particularly sensitive to unintentional chirp to the picosecond beam, and even minimal amounts of chirp have to be quantified to obtain good fits at all probe delays. The use of specific time delays $\frac{\tau_{full}}{4} + \frac{\tau_{full}}{2}n$ can help to reduce the sensitivity to chirp effects. The results show that chirp does not hinder the ability to provide reliable temperature or pressure measurements at any probe delay. The use of hybrid CARS as a pressure measurement in the time domain remains challenging for the BOXCARS configuration due to beam overlap effects; on the other hand, frequency domain measurements are reliable for the BOXCARS setup.

9.2 Future work

The impinging flame experiments could benefit from varying more parameters. The use of a heated plate could help to provide more information about the thermo-chemical effects and the fluid mechanical interaction and study the CO emissions as a function of plate heating. Extending the study using diluted methane would approach the experimental configuration to practical systems. For the fluorescence measurements using a configuration that allowed investigation of the signal up to higher pressures which the chamber can sustain ($1-100\,bar$); for this the use of Helium as a bath gas in the chamber, and an inverted flame configuration would reduce the buoyant instabilities. The inverted flame configuration could allow studying chemistry effects and practical diagnostic challenges up to higher pressures. For the HCARS experiments, the current model is limited to nitrogen, and it would be good to validate it and extend it to oxygen to be used in a real flame configuration.

Bibliography

[1] U.S. Energy Information Administration. March 2017 Monthly Energy Review. Technical report, 2017.

[2] US Energy Information Administration - EIA. International Energy Outlook 2016. Technical report, 2016.

[3] Vinicius M Sauer and Derek Dunn-rankin. Impinging nonpremixed coflow methane – air flames with unity Lewis number. *Proceedings of the Combustion Institute*, 000:1–9, 2016.

[4] N. A. Slavinskaya and P. Frank. A modelling study of aromatic soot precursors formation in laminar methane and ethene flames. *Combustion and Flame*, 2009.

[5] Mike Gat Nahum, Garman John, Dunn-Rankin Derek, and Papac. Rocket Engine Boundary Layer Temperature Measurements Using Coherent Anti-Stokes Raman Spectroscopy (CARS). *SBIR Phase I Final Report*, pages 1–43, 2006.

[6] Yu-Chien Chien. *Electrical Aspects of Impinging Flames*. PhD thesis, 2014.

[7] Sunny Karnani. *Electric Field-Driven Flame Dynamics*. PhD thesis, 2011.

[8] Michael James Papac. *Electrical aspects of gaseous fuel flames for microgravity combustion and combustion control*. PhD thesis, 2005.

[9] Mitchell D Smooke, P. Lin, J. K. Lam, and M. B. Long. Computational and experimental study of a laminar axisymmetric methane-air diffusion flame. *Symposium (International) on Combustion*, 1991.

[10] K.T. Walsh, M.B. Long, M.a. Tanoff, and M.D. Smooke. Experimental and computational study of CH, CH*, and OH* in an axisymmetric laminar diffusion flame. *Symposium (International) on Combustion*, 1998.

[11] Gaetan Crouzy. Development and evaluation of a calibration test cell for CARS measurements. Technical report, 2015.

[12] Gaetan Ruscade. Instrumentation for high pressure combustion experiments. Technical Report July, 2016.

[13] Peter H. Joo, Jinlong Gao, Zhongshan Li, and Marcus Aldén. Experimental apparatus with full optical access for combustion experiments with laminar flames from a single circular nozzle at elevated pressures. *Review of Scientific Instruments*, 2015.

[14] Hyun I. Joo and Ömer L. Gülder. Soot formation and temperature field structure in co-flow laminar methane–air diffusion flames at pressures from 10 to 60 atm. *Proceedings of the Combustion Institute*, 32(1):769–775, 2009.

[15] Nasa Tn, Iruin M Miller, and G M Howard. High-pressure flame system for pollution studies with results for methane-air diffusion flames. Technical Report June, 1977.

[16] Yu-Chien Chien, David Escofet-Martin, and Derek Dunn-Rankin. CO emission from an impinging non-premixed flame. *Combustion and Flame*, 174:16–24, 2016.

[17] W. G. Bessler and C. Schulz. Quantitative multi-line NO-LIF temperature imaging. *Applied Physics B: Lasers and Optics*, 2004.

[18] J Nygren, J Engström, J Walewski, CF Kaminski, and M Aldén. Applications and evaluation of two-line atomic LIF thermometry in sooting. *Measurement Science and Technology*, 12(8), 2001.

[19] Alan C. Eckbreth. Laser Diagnostics for combustion temperature and species measurements. *Journal of Chemical Information and Modeling*, 1989.

[20] Katharina Kohse-Höinghaus and Jay Barker Jeffries. Applied combustion diagnostics. 2002.

[21] J M Seitzman, R K Hanson, P a Debarber, and C F Hess. Application of quantitative two-line OH planar laser-induced fluorescence for temporally resolved planar thermometry in reacting flows. *Applied optics*, 33(18):4000–4012, 1994.

[22] Robert Cattolica. OH rotational temperature from two-line laser-excited fluorescence. *Applied Optics*, 1981.

[23] J. M. Seitzman, R. K. Hanson, P. A. DeBarber, and C. F. Hess. Application of quantitative two-line OH planar laser-induced fluorescence for temporally resolved planar thermometry in reacting flows. *Applied Optics*, 1994.

[24] Robert Giezendanner-Thoben, Ulrich Meier, Wolfgang Meier, Johannes Heinze, and Manfred Aigner. Phase-locked two-line OH planar laser-induced fluorescence thermometry in a pulsating gas turbine model combustor at atmospheric pressure. *Applied optics*, 2005.

[25] Markus Mann, Christopher Jainski, Matthias Euler, Benjamin Böhm, and Andreas Dreizler. Transient flame–wall interactions: Experimental analysis using spectroscopic temperature and CO concentration measurements. *Combustion and Flame*, 161(9):2371–2386, sep 2014.

[26] Avinash Singh, Markus Mann, Thilo Kissel, Jan Brübach, and Andreas Dreizler. Simultaneous measurements of temperature and CO concentration in stagnation stabilized flames. *Flow, Turbulence and Combustion*, 90(4):723–739, 2013.

[27] J W Daily and E W Rothe. Effect of laser intensity and of lower-state rotational energy transfer upon temperature measurements made with laser-induced fluorescence. *Applied Physics B*, 68:131–140, 1999.

[28] David Escofet-Martin, Yu-Chien Chien, and Derek Dunn-Rankin. OH PLIF of an Impinging Flame. *WSCII Spring meeting*, 2014.

[29] B. B. Dally, A. R. Masri, R. S. Barlow, and G. J. Fiechtner. Two-photon laser-induced fluorescence measurement of CO in turbulent non-premixed bluff body flames. *Combustion and Flame*, 2003.

[30] N Georgiev and M Aldén. Two-dimensional imaging of flame species using two-photon laser induced fluorescence. *Applied Spectroscopy*, Vol. 51, N(8):1229–1237, 1997.

[31] M. Richter, Z. S. Li, and M. Aldén. Application of two-photon laser-induced fluorescence for single-shot visualization of carbon monoxide in a spark ignited engine. *Applied Spectroscopy*, 2007.

[32] Jurgen Haumann, Jerry M. Seitzman, and Ronald K. Hanson. Two-photon digital imaging of CO in combustion flows using planar laser-induced fluorescence. *Optics letters*, 11(12):776–778, 1986.

[33] Paul J. H. Tjossem and Kermit C. Smyth. Multiphoton excitation spectroscopy of the B ^{1} Σ $^+$ and C ^{1} Σ $^+$ Rydberg states of CO. *The Journal of Chemical Physics*, 91(4):2041–2048, 1989.

[34] T.D. Varberg and K.M. Evenson. Laser spectroscopy of carbon monoxide: a frequency reference for the far infrared. *IEEE Transactions on Instrumentation and Measurement*, 1993.

[35] C Amiot, J Y Roncin, and J Verges. First observation of the CO E^1 Π to B^1 Σ $^+$ and C^1 Σ $^+$ to B ^{1} Σ^+ band systems. Predissociation in the E^1 Π(v=0) level. *Journal of Physics B: Atomic and Molecular Physics*, 19(1):L19–L23, jan 1986.

[36] Michael D. di Rosa and Roger L. Farrow. Cross sections of photoionization and ac Stark shift measured from Doppler-free B <- X(0, 0) excitation spectra of CO. *Journal of the Optical Society of America B*, 1999.

[37] R.G. Bray and R.M. Hochstrasser. Two-photon absorption by rotating diatomic molecules. *Molecular Physics*, 1976.

[38] A. P. Nefedov, V. A. Sinelshchikov, A. D. Usachev, and A. V. Zobnin. Photochemical effect in two-photon laser-induced fluorescence detection of carbon monoxide in hydrocarbon flames. *Applied optics*, 37(33):7729–7736.

[39] Ronaid K Hanson, Jerry M Seitzman, and Phillip H Paul. Planar Laser-Fluorescence Imaging of Combustion Gases. *Applied Physics B*, 441454, 1990.

[40] R. Sadanandan, M. Stöhr, and W. Meier. Simultaneous OH-PLIF and PIV measurements in a gas turbine model combustor. *Applied Physics B*, 90(3-4):609–618, feb 2008.

[41] Soon Muk Hwang, Jun N. Kojima, Quang-Viet Nguyen, and Martin J. Rabinowitz. Measurement of collision broadening of the $P^1(5)$ line of (0,0) band of OH $A^2\Sigma^+ \leftarrow X^2\Pi$ transition at high temperatures. *Journal of Quantitative Spectroscopy and Radiative Transfer*, 109(16):2715–2724, nov 2008.

[42] E.C. Rea, A.Y. Chang, and R.K. Hanson. Collisional broadening of the $A^2\Sigma^+ \leftarrow X^2\Pi(0,0)$ band of OH by H_2O and CO_2 in atmospheric-pressure flames. *Journal of Quantitative Spectroscopy and Radiative Transfer*, 41(1):29–42, jan 1989.

[43] A. Matynia, M. Idir, J. Molet, C. Roche, S. De Persis, and L. Pillier. Absolute OH concentration profiles measurements in high pressure counterflow flames by coupling LIF, PLIF, and absorption techniques. *Applied Physics B: Lasers and Optics*, 108(2):393–405, 2012.

[44] Katharina Kohse-Höinghaus. Laser techniques for the quantitative detection of reactive intermediates in combustion systems. *Progress in Energy and Combustion Science*, 20(3):203–279, jan 1994.

[45] Nancy L. Garland and David R. Crosley. On the collisional quenching of electronically excited OH, NH and CH in flames. *Symposium (International) on Combustion*, 21(1):1693–1702, jan 1988.

[46] P.H. Paul. A model for temperature-dependent collisional quenching of $OHA^2\sum^+$. *Journal of Quantitative Spectroscopy and Radiative Transfer*, 51(3):511–524, mar 1994.

[47] Andreas Brockhinke, Andreas Bülter, Juan C. Rolon, and Katharina Kohse-Höinghaus. ps-LIF measurements of minor species concentration in a counterflow diffusion flame interacting with a vortex. *Applied Physics B: Lasers and Optics*, 2001.

[48] G.H. Dieke and H.M. Crosswhite. The ultraviolet bands of OH Fundamental data. *Journal of Quantitative Spectroscopy and Radiative Transfer*, 2(2):97–199, apr 1962.

[49] Sunny Karnani and Derek Dunn-Rankin. Visualizing CH* chemiluminescence in sooting flames. *Combustion and Flame*, 160(10):2275–2278, 2013.

[50] Max Hofmann, Wolfgang G Bessler, Christof Schulz, and Helga Jander. Laser-induced incandescence for soot diagnostics at high pressures. *Applied optics*, 2003.

[51] Jörg Appel, Henning Bockhorn, and Michael Frenklach. Kinetic modeling of soot formation with detailed chemistry and physics: laminar premixed flames of C_2 hydrocarbons. *Combustion and Flame*, 2000.

[52] Hrvoje Jasak, Aleksandar Jemcov, and Zeljko Tukovic. OpenFOAM : A C ++ Library for Complex Physics Simulations. *International Workshop on Coupled Methods in Numerical Dynamics*, 2007.

[53] OpenFOAM Foundation. Open∇FOAM - The Open Source CFD Toolbox - User Guide. Technical report, 2014.

[54] Hassan I. Kassem, Khalid M. Saqr, Hossam S. Aly, Mohsin M. Sies, and Mazlan Abdul Wahid. Implementation of the eddy dissipation model of turbulent non-premixed combustion in OpenFOAM. *International Communications in Heat and Mass Transfer*, 2011.

[55] A. Cuoci, A. Frassoldati, T. Faravelli, and E. Ranzi. A computational tool for the detailed kinetic modeling of laminar flames: Application to C_2H_4 CH_4 coflow flames. *Combustion and Flame*, 2013.

[56] Marc J Assael, J P Martin Trusler, and Thomas F Tsolakis. *Thermophysical Properties of Fluids*, volume 1. Imperial College press, jul 1996.

[57] Bonnie J. McBride, Sanford Gordon, and Martin A. Reno. Coefficients for Calculating Thermodynamic and Transport Properties of Individual Species. Technical report, 1993.

[58] Gregory P. Smith, David M. Golden, Michael Frenklach, Nigel W. Moriarty, Boris Eiteneer, Mikhail Goldenberg, C. Thomas Bowman, Ronald K. Hanson, Soonho Song, William C. Gardiner, Vitali V. Lissianski Jr., Qin, and Zhiwei. GRI-Mech3.0.

[59] A. Kazakov and M. Frenlack. DRM.

[60] Victor Chernov, Murray J. Thomson, Seth B. Dworkin, Nadezhda A. Slavinskaya, and Uwe Riedel. Soot formation with C_1 and C_2 fuels using an improved chemical mechanism for PAH growth. *Combustion and Flame*, 2014.

[61] Rosa Padilla. *Structure and Behavior of Water-laden Methane/Air Flames.* PhD thesis, 2016.

[62] R E Palmer. The CARSFT computer code calculating coherent anti-Stokes Raman spectra: User and programmer information. Technical report, 1989.

[63] Alan C Eckbreth. *Laser diagnostics for combustion temperature and species.* Gordon and Breach Publishers, 1996.

[64] Sukesh Roy, James R Gord, and Anil K Patnaik. Recent advances in coherent anti-Stokes Raman scattering spectroscopy: Fundamental developments and applications in reacting flows. *Prog. Energy Combust. Sci.*, 36(2), 2010.

[65] Fredrik Vestin and Per-Erik Bengtsson. Rotational CARS for simultaneous measurements of temperature and concentrations of N_2, O_2, CO, and CO_2 demonstrated in a CO/air diffusion flame. *Proc. Comb. Inst.*, 32(1), 2009.

[66] T R Meyer, S Roy, R P Lucht, and J R Gord. Dual-pump dual-broadband CARS for exhaust-gas temperature and CO_2–O_2–N_2 mole-fraction measurements in model gas-turbine combustors. *Combust. Flame*, 142(1), 2005.

[67] P Beaud, H-M Frey, T Lang, and M Motzkus. Flame thermometry by femtosecond CARS. *Chem. Phys. Lett.*, 344(3), 2001.

[68] Robert P Lucht, Sukesh Roy, Terrence R Meyer, and James R Gord. Femtosecond coherent anti-Stokes Raman scattering measurement of gas temperatures from frequency-spread dephasing of the Raman coherence. *Appl. Phys. Lett.*, 89(25), 2006.

[69] Sukesh Roy, Paul J Kinnius, Robert P Lucht, and James R Gord. Temperature measurements in reacting flows by time-resolved femtosecond coherent anti-Stokes Raman scattering (fs-CARS) spectroscopy. *Opt. Commun.*, 281(2), 2008.

[70] Sukesh Roy, Waruna D Kulatilaka, Daniel R Richardson, Robert P Lucht, and James R Gord. Gas-phase single-shot thermometry at 1 kHz using fs-CARS spectroscopy. *Opt. Lett.*, 34(24), 2009.

[71] Benjamin D Prince, Abhijit Chakraborty, Beth M Prince, and Hans U Stauffer. Development of simultaneous frequency and time-resolved coherent anti-Stokes Raman scattering for ultrafast detection of molecular Raman spectra. *J. Chem. Phys.*, 125(4), 2006.

[72] Sean P Kearney. Hybrid fs/ps rotational CARS temperature and oxygen measurements in the product gases of canonical flat flames. *Combust. Flame*, 162(5), 2015.

[73] Sean P Kearney and Daniel R Guildenbecher. Temperature measurements in metalized propellant combustion using hybrid fs/ps coherent anti-Stokes Raman scattering. *Appl. Opt.*, 55(18), 2016.

[74] Joseph D Miller, Chloe E Dedic, Sukesh Roy, James R Gord, and Terrence R Meyer. Interference-free gas-phase thermometry at elevated pressure using hybrid femtosecond/picosecond rotational coherent anti-Stokes Raman scattering. *Opt. Express*, 20(5), 2012.

[75] Alexis Bohlin and Christopher J Kliewer. Communication: Two-dimensional gas-phase coherent anti-Stokes Raman spectroscopy (2D-CARS): Simultaneous planar imaging and multiplex spectroscopy in a single laser shot. *J. Chem. Phys.*, 138(22), 2013.

[76] Alexis Bohlin and Christopher J Kliewer. Single-shot hyperspectral coherent Raman planar imaging in the range 0–4200 cm^{-1}. *Appl. Phys. Lett.*, 105(16), 2014.

[77] Joseph D Miller, Mikhail N Slipchenko, Jason G Mance, Sukesh Roy, and James R Gord. 1-kHz two-dimensional coherent anti-Stokes Raman scattering (2D-CARS) for gas-phase thermometry. *Opt. Express*, 24(22), 2016.

[78] Hans U Stauffer, Joseph D Miller, Sukesh Roy, James R Gord, and Terrence R Meyer. Communication: Hybrid fs/ps rotational coherent anti-Stokes Raman scattering thermometry using a narrowband time-asymmetric probe pulse. *J. Chem. Phys.*, 136(11), 2012.

[79] Hans U Stauffer, Joseph D Miller, Mikhail N Slipchenko, Terrence R Meyer, Benjamin D Prince, Sukesh Roy, and James R Gord. Time and frequency dependent model of time resolved coherent anti-Stokes Raman scattering (CARS) with a picosecond duration probe pulse. *J. Chem. Phys.*, 140(2), 2014.

[80] Sean P Kearney. Bandwidth optimization of femtosecond pure-rotational coherent anti-Stokes Raman scattering by pump/Stokes spectral focusing. *Applied Optics*, 2014.

[81] Michele Marrocco. Time-domain coherent anti-Stokes Raman scattering in terms of the time-delayed Yuratich equation. *Opt. Lett.*, 39(16), aug 2014.

[82] Shaul Mukamel. *Principles of nonlinear optical spectroscopy*. Oxford University Press,, 1999.

[83] Joseph D Miller, Mikhail N Slipchenko, Terrence R Meyer, Hans U Stauffer, and James R Gord. Hybrid femtosecond/picosecond coherent anti-Stokes Raman scattering for high-speed gas-phase thermometry. *Opt. Lett.*, 35(14), 2010.

[84] C. J. Kliewer, A. Bohlin, E. Nordström, B. D. Patterson, P.-E. Bengtsson, and T. B. Settersten. Time-domain measurements of S-branch N_2–N_2 Raman linewidths using picosecond pure rotational coherent anti-Stokes Raman spectroscopy. *Applied Physics B*, 2012.

[85] Joseph D. Miller, Sukesh Roy, James R. Gord, and Terrence R. Meyer. Communication: Time-domain measurement of high-pressure N_2 and O_2 self-broadened linewidths using hybrid femtosecondpicosecond coherent anti-Stokes Raman scattering. *Journal of Chemical Physics*, 2011.

[86] Sean P Kearney and Paul M Danehy. Pressure measurements using hybrid femtosecond/picosecond rotational coherent anti-Stokes Raman scattering. *Optics Letters*, 2015.

[87] Lars Martinsson, Per-Erik Bengtsson, Marcus Aldén, Stefan Kröll, and Jeanine Bonamy. A test of different rotational Raman linewidth models: Accuracy of rotational coherent anti-Stokes Raman scattering thermometry in nitrogen from 295 to 1850 K. *J. Chem. Phys.*, 99(4), 1993.

[88] P W Dooley, I V Litvinyuk, Kevin F Lee, D M Rayner, M Spanner, D M Villeneuve, and P B Corkum. Direct imaging of rotational wave-packet dynamics of diatomic molecules. *Phys. Rev. A*, 68(2), aug 2003.

[89] Paul Kumar Upputuri, Li Gong, and Haifeng Wang. Chirped time-resolved CARS microscopy with square-pulse excitation. *Opt. Express*, 22(8), 2014.

[90] I. H. Malitson. Interspecimen Comparison of the Refractive Index of Fused Silica. *Journal of the Optical Society of America*, 1965.

[91] C.Z. Tan. Determination of refractive index of silica glass for infrared wavelengths by IR spectroscopy. *Journal of Non-Crystalline Solids*, 1998.

[92] F Raoult, A C L Boscheron, D Husson, C Sauteret, A Modena, Victor Malka, F Dorchies, and A Migus. Efficient generation of narrow-bandwidth picosecond pulses by frequency doubling of femtosecond chirped pulses. *Opt. Lett.*, 23(14), 1998.

[93] Liangdong Zhu, Weimin Liu, and Chong Fang. A versatile femtosecond stimulated Raman spectroscopy setup with tunable pulses in the visible to near infrared. *Appl. Phys. Lett.*, 105(4), 2014.

Appendix A

Flowmeter calibration

Flowmeter reading$\left(\frac{ml}{min}\right)$	$t_1(s)$	$t_2(s)$	$t_3(s)$	$t_4(s)$	$t_5(s)$	Flow measured$\left(\frac{ml}{min}\right)$
20	31.64	31.39	31.6	31.73	31.43	19.09
30	18.36	18.51	18.51	18.36	18.35	32.70
40	12.92	13.06	12.91	13.07	13.01	46.12
50	10.16	10.07	10.15	10.1	10.19	58.88
60	8.37	8.31	8.37	8.26	8.38	71.60

Table A.1: Flowmeter calibration 200 *psi*

Flowmeter reading$\left(\frac{ml}{min}\right)$	$t_1(s)$	$t_2(s)$	$t_3(s)$	$t_4(s)$	$t_5(s)$	Flow measured$\left(\frac{ml}{min}\right)$
20	33.68	34.36	34.12	34.04	34.36	17.46
30	19.23	19.18	19.13	19.19	19.15	31.33
40	13.42	13.70	12.91	13.07	13.01	46.12
50	10.64	10.72	10.62	10.67	10.61	56.55
60	8.86	8.84	8.76	8.85	8.79	68.26

Table A.2: Flowmeter calibration 500 *psi*

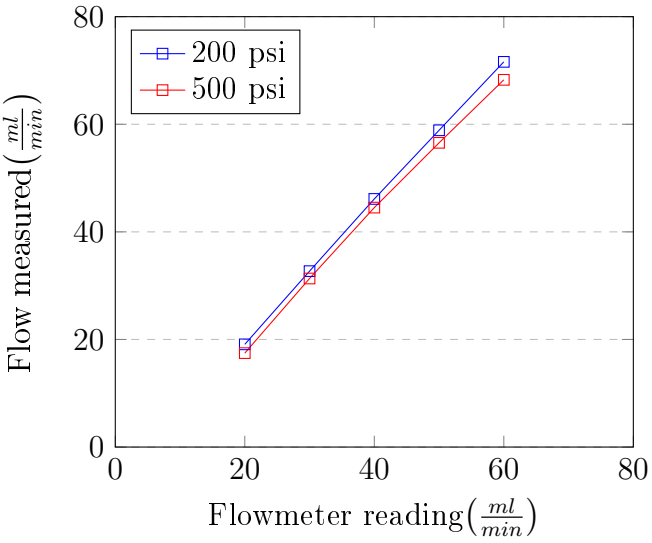
200 psi
500 psi
Flow measured($\frac{ml}{min}$)
Flowmeter reading($\frac{ml}{min}$)
0
20
40
60
80

Appendix B

2-photon CO with electric field

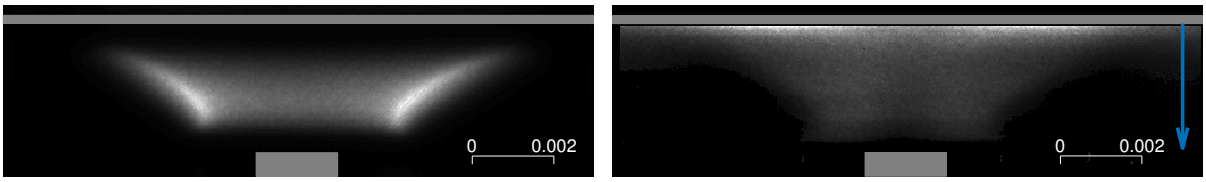

(a) CO^* chemiluminescence. (b) CO 2-photon PLIF.

Figure B.1: 3 mm burner to plate -2 kV

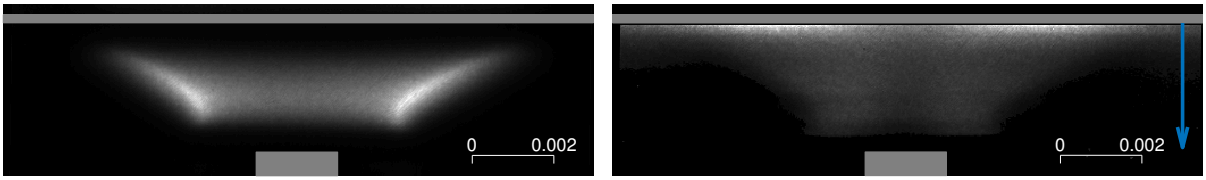

(a) CO^* chemiluminescence. (b) CO 2-photon PLIF.

Figure B.2: 3 mm burner to plate -1 kV

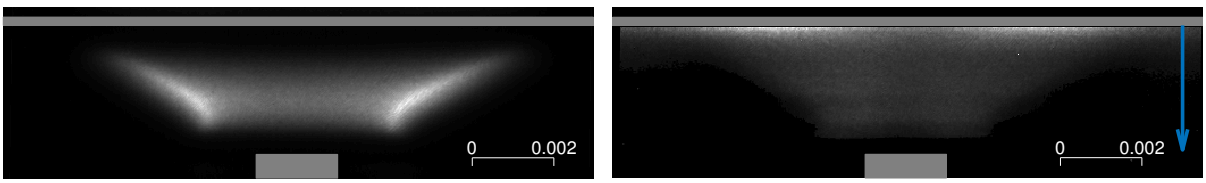

(a) CO^* chemiluminescence. (b) CO 2-photon PLIF.

Figure B.3: 3 mm burner to plate 0 kV

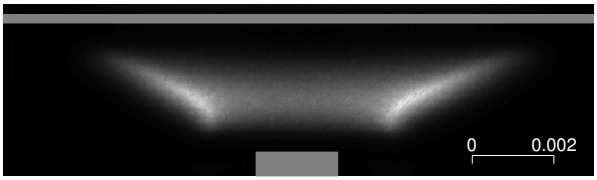

(a) CO^* chemiluminescence.

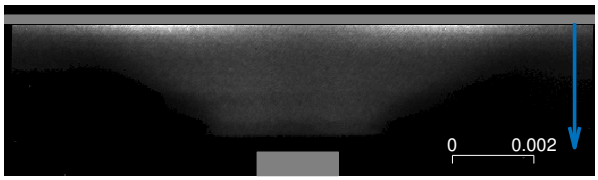

(b) CO 2-photon PLIF.

Figure B.4: 3 mm burner to plate 1 kV

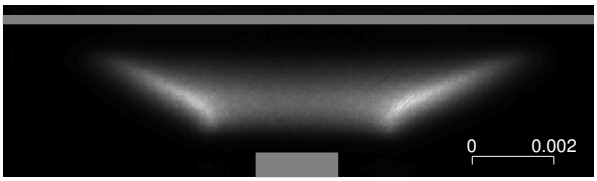

(a) CO^* chemiluminescence.

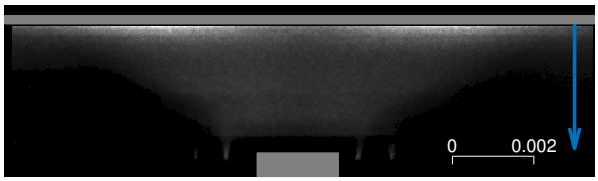

(b) CO 2-photon PLIF.

Figure B.5: 3 mm burner to plate 2 kV

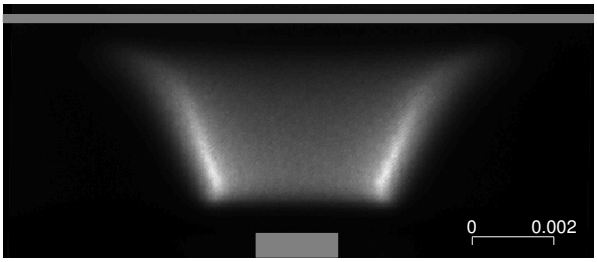

(a) CO^* chemiluminescence.

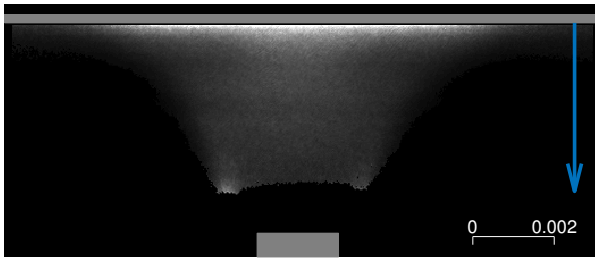

(b) CO 2-photon PLIF.

Figure B.6: 5 mm burner to plate -3 kV

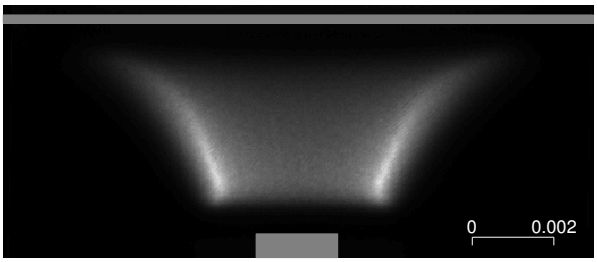

(a) CO^* chemiluminescence.

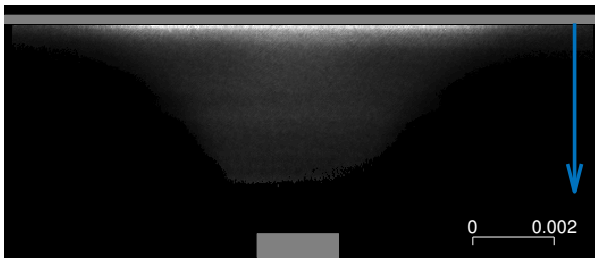

(b) CO 2-photon PLIF.

Figure B.7: 5 mm burner to plate -2 kV

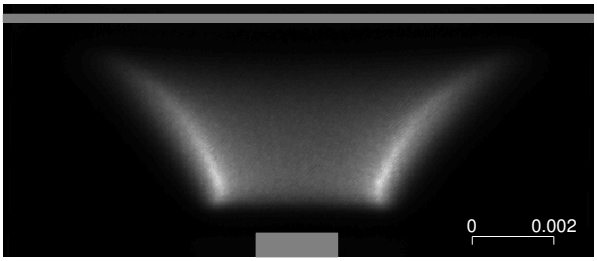

(a) CO^* chemiluminescence.

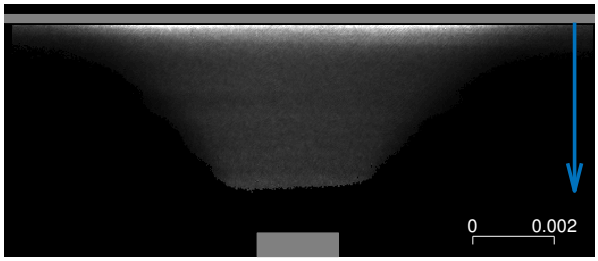

(b) CO 2-photon PLIF.

Figure B.8: 5 mm burner to plate 0 kV

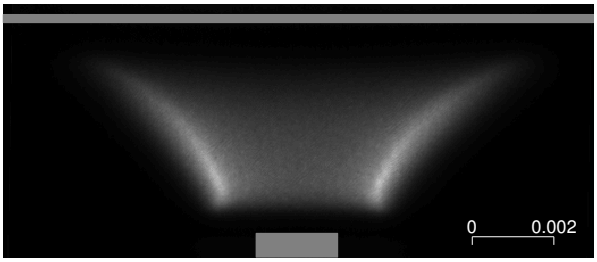

(a) CO^* chemiluminescence.

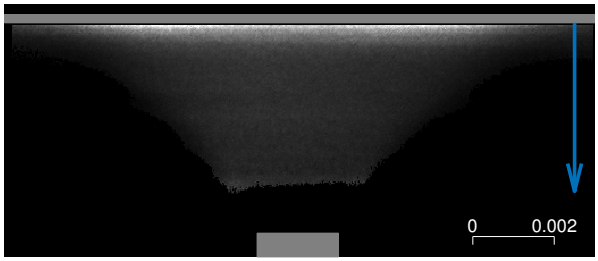

(b) CO 2-photon PLIF.

Figure B.9: 5 mm burner to plate 2 kV

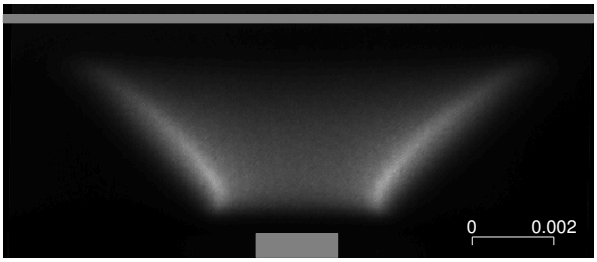

(a) CO^* chemiluminescence.

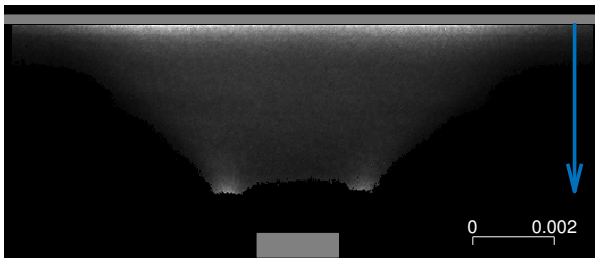

(b) CO 2-photon PLIF.

Figure B.10: 5 mm burner to plate 3 kV

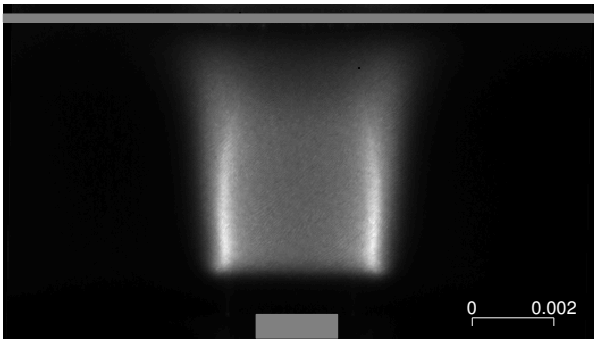

(a) CO^* chemiluminescence.

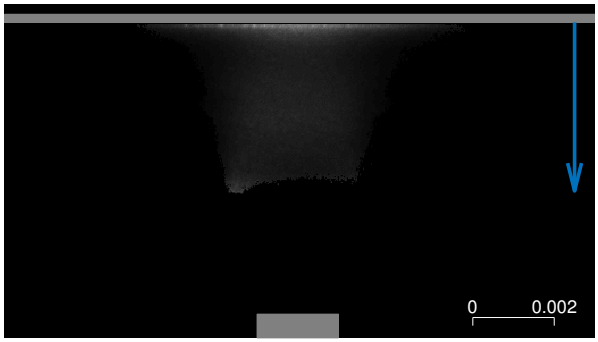

(b) CO 2-photon PLIF.

Figure B.11: 7 mm burner to plate -4 kV

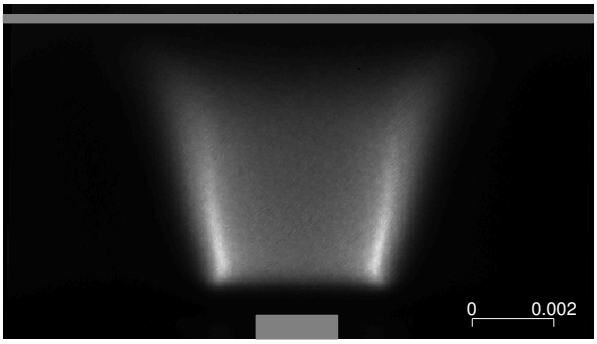

(a) CO^* chemiluminescence.

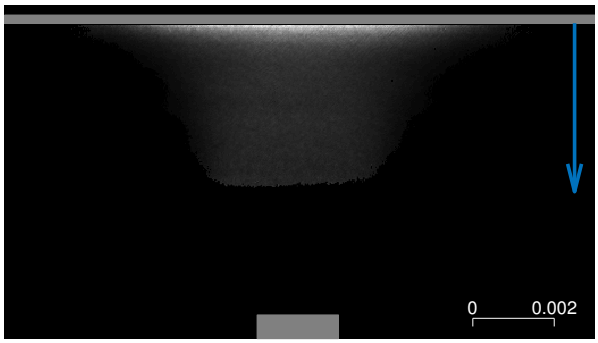

(b) CO 2-photon PLIF.

Figure B.12: 7 mm burner to plate -3 kV

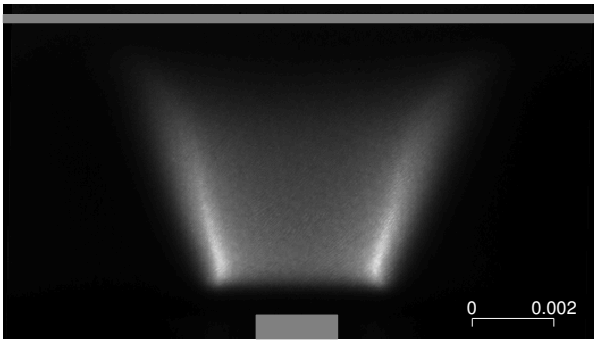

(a) CO^* chemiluminescence.

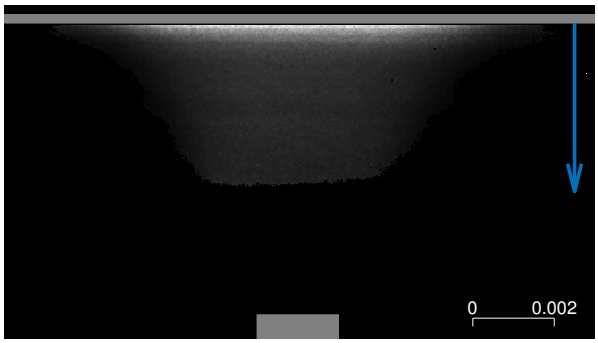

(b) CO 2-photon PLIF.

Figure B.13: 7 mm burner to plate 0 kV

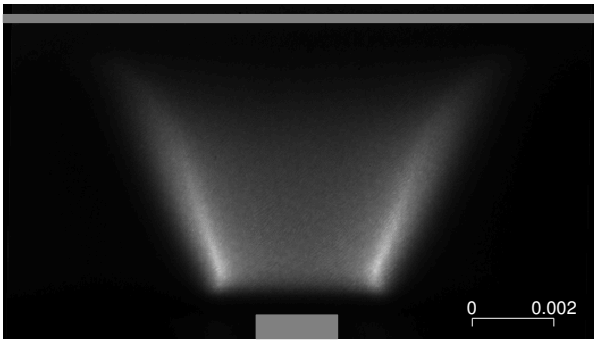

(a) CO^* chemiluminescence.

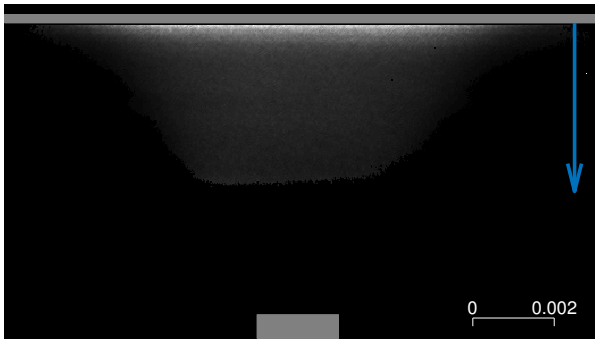

(b) CO 2-photon PLIF.

Figure B.14: 7 mm burner to plate 1 kV

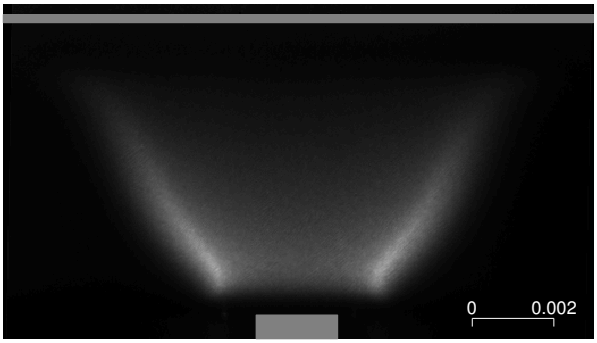

(a) CO^* chemiluminescence.

(b) CO 2-photon PLIF.

Figure B.15: 7 mm burner to plate 4 kV

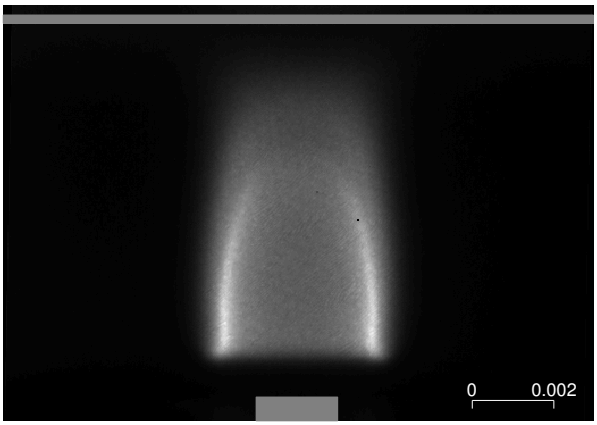

(a) CO^* chemiluminescence.

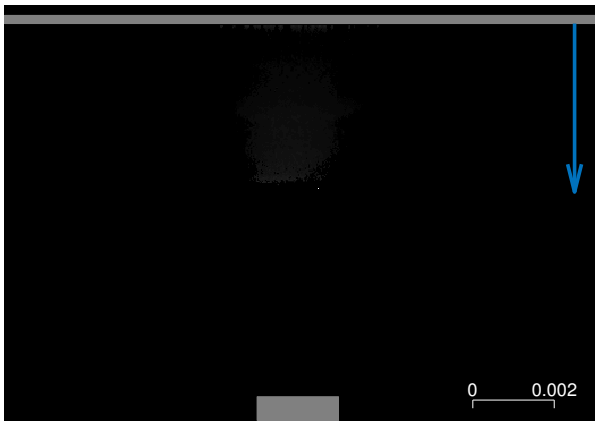

(b) CO 2-photon PLIF.

Figure B.16: 9 mm burner to plate -5 kV

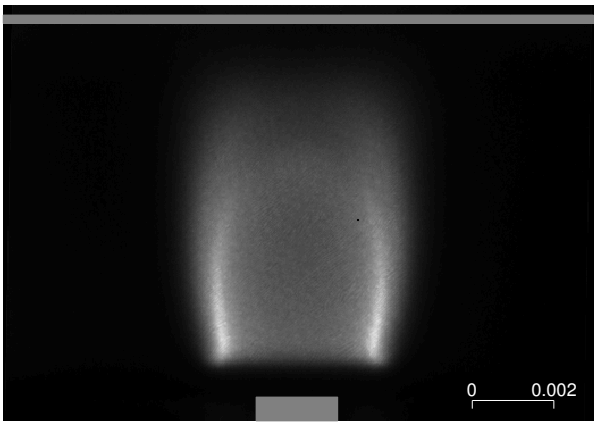

(a) CO^* chemiluminescence.

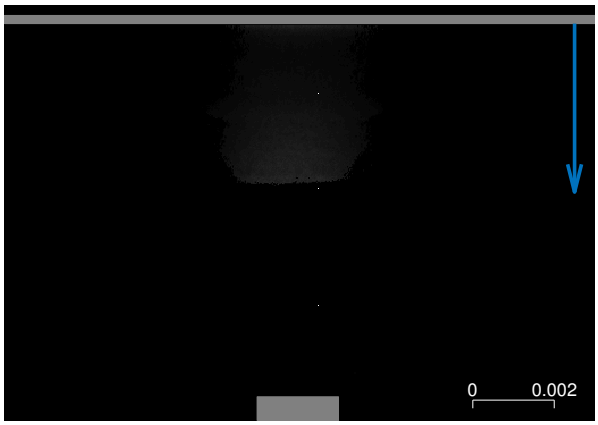

(b) CO 2-photon PLIF.

Figure B.17: 9 mm burner to plate -2 kV

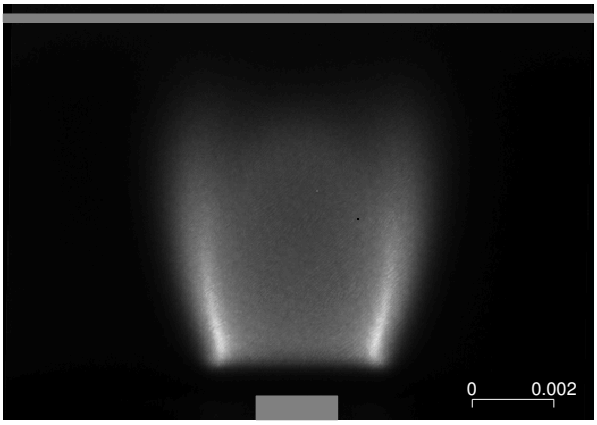

(a) CO^* chemiluminescence.

(b) CO 2-photon PLIF.

Figure B.18: 9 mm burner to plate 0 kV

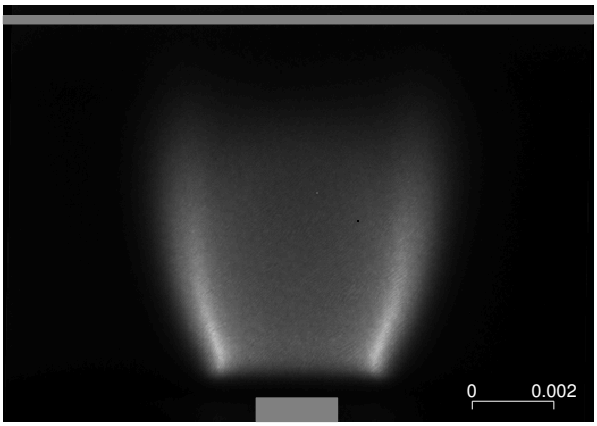

(a) CO^* chemiluminescence.

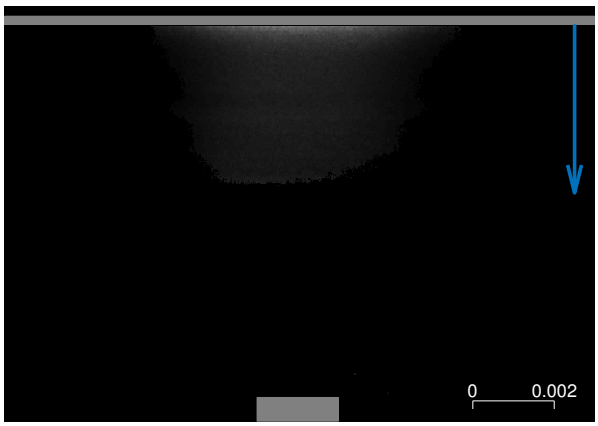

(b) CO 2-photon PLIF.

Figure B.19: 9 mm burner to plate 2 kV

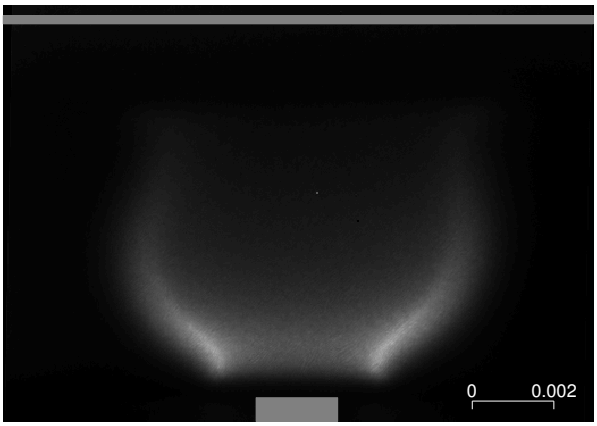

(a) CO^* chemiluminescence.

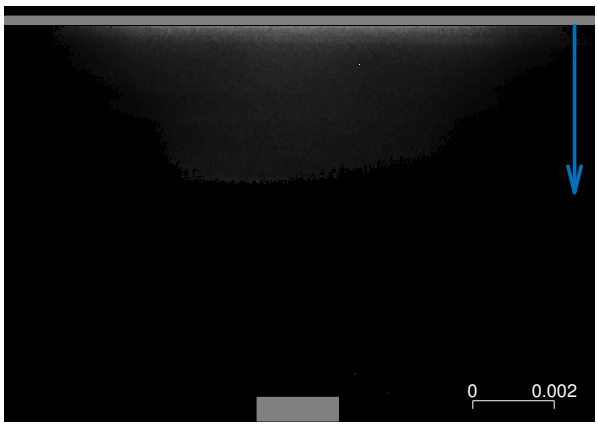

(b) CO 2-photon PLIF.

Figure B.20: 9 mm burner to plate 5 kV

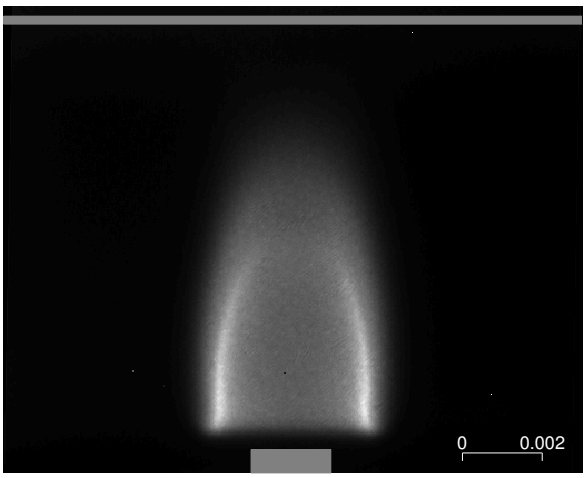

(a) CO^* chemiluminescence.

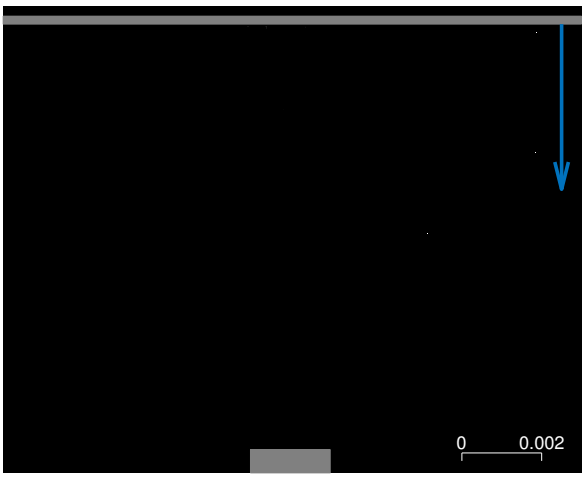

(b) CO 2-photon PLIF.

Figure B.21: 11 mm burner to plate -6 kV

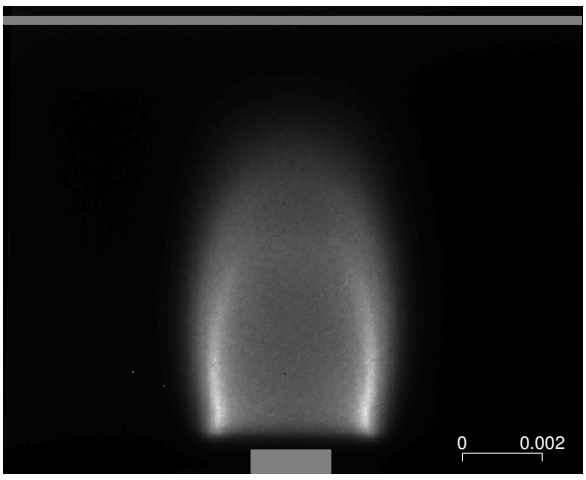

(a) CO^* chemiluminescence.

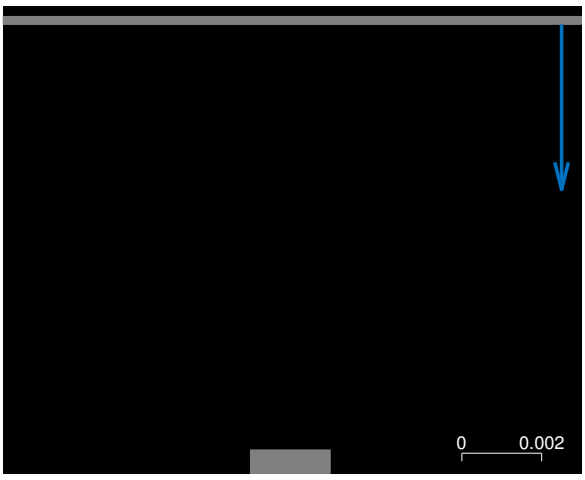

(b) CO 2-photon PLIF.

Figure B.22: 11 mm burner to plate -3 kV

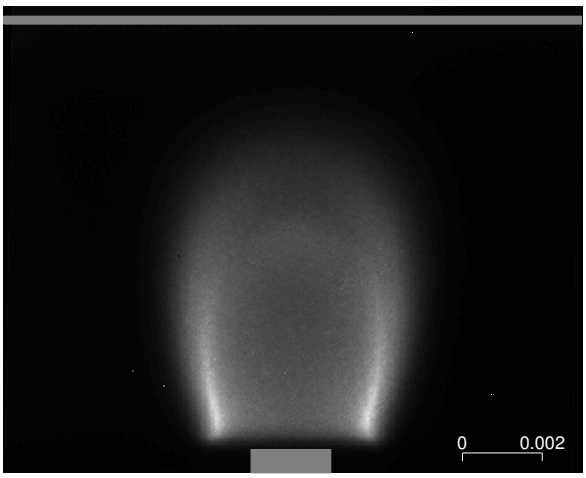

(a) CO^* chemiluminescence.

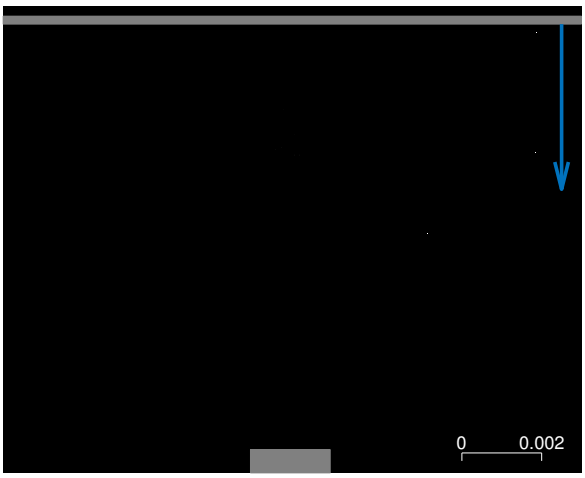

(b) CO 2-photon PLIF.

Figure B.23: 11 mm burner to plate 0 kV

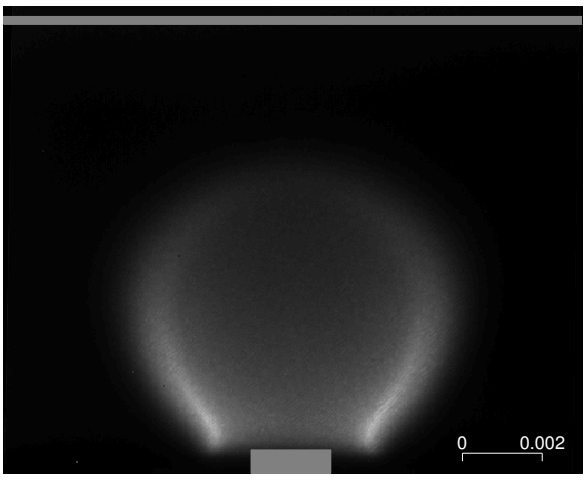

(a) CO^* chemiluminescence.

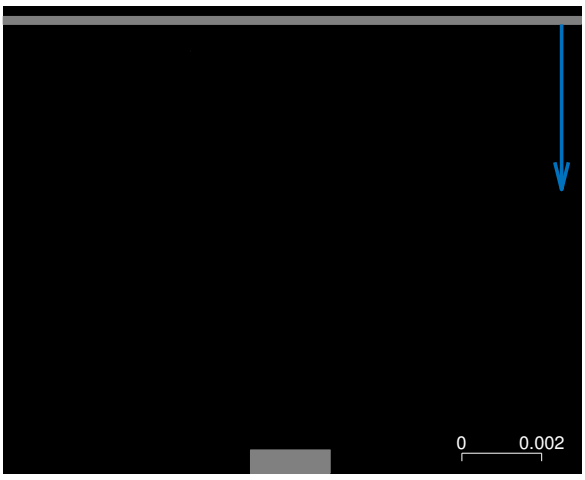

(b) CO 2-photon PLIF.

Figure B.24: 11 mm burner to plate 5 kV

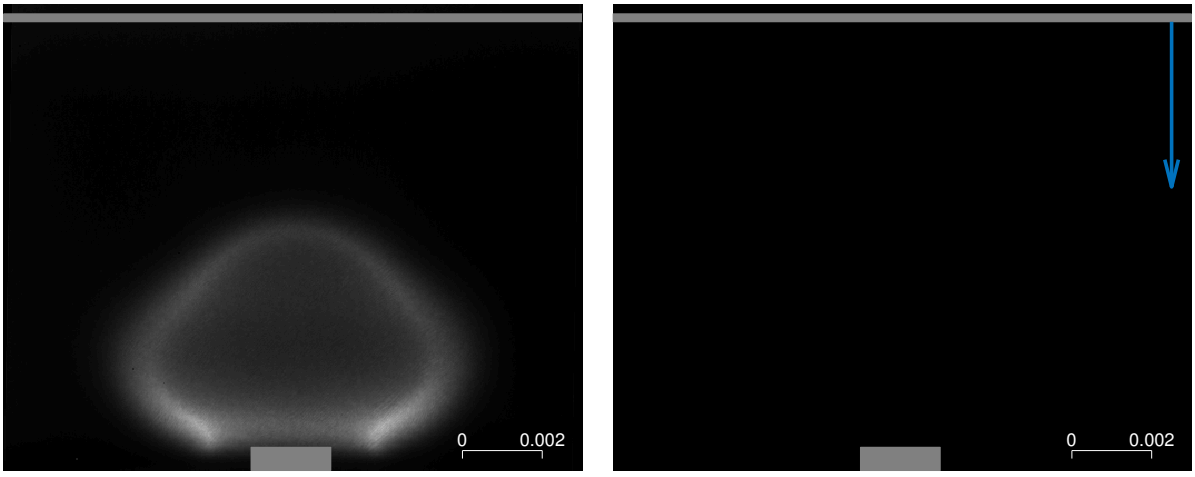

(a) COe^* chemiluminescence. (b) CO 2-photon PLIF.

Figure B.25: 11 mm burner to plate 6 kV

Appendix C

Viscosity Sutherland coefficients

Molecule	A_s ($\frac{kg}{ms\sqrt{K}}$)	T_s (K)	Residual
OH	$2.17 \cdot 10^{-6}$	170.62	$6.64 \cdot 10^{-11}$
CN	$1.37 \cdot 10^{-6}$	170.53	$2.8 \cdot 10^{-11}$
C_2H_3	$1.05 \cdot 10^{-6}$	172.10	$6.13 \cdot 10^{-11}$
N_2	$1.56 \cdot 10^{-6}$	171.67	$2.98 \cdot 10^{-11}$
$HOCN$	$1.50 \cdot 10^{-6}$	179.19	$1.52 \cdot 10^{-10}$
N	$1.39 \cdot 10^{-6}$	170.44	$2.96 \cdot 10^{-11}$
C_2H	$1.01 \cdot 10^{-6}$	172.51	$5.62 \cdot 10^{-11}$
HNO	$1.74 \cdot 10^{-6}$	170.67	$3.62 \cdot 10^{-11}$
CH_2CO	$1.20 \cdot 10^{-6}$	180.34	$6.34 \cdot 10^{-10}$
CH_3	$9.74 \cdot 10^{-7}$	171.25	$1.58 \cdot 10^{-11}$
C_2H_5	$9.60 \cdot 10^{-7}$	172.50	$9.63 \cdot 10^{-11}$
C_2H_4	$1.08 \cdot 10^{-6}$	173.94	$1.69 \cdot 10^{-10}$
C_3H_8	$8.71 \cdot 10^{-7}$	172.13	$9.59 \cdot 10^{-11}$
HCN	$1.07 \cdot 10^{-6}$	176.94	$8.89 \cdot 10^{-10}$
C_2H_6	$9.76 \cdot 10^{-7}$	172.58	$9.95 \cdot 10^{-11}$

Molecule	A_s ($\frac{kg}{ms\sqrt{K}}$)	T_s (K)	Residual
NH_3	$1.34 \cdot 10^{-6}$	184.18	$1.25 \cdot 10^{-9}$
CO_2	$1.565 \cdot 10^{-6}$	181.85	$1.86 \cdot 10^{-10}$
C_2H_2	$1.03 \cdot 10^{-6}$	172.24	$5.89 \cdot 10^{-11}$
CH_2OH	$1.19 \cdot 10^{-6}$	177.31	$6.97 \cdot 10^{-10}$
H_2CN	$1.09 \cdot 10^{-6}$	177.24	$9.21 \cdot 10^{-10}$
$HCCOH$	$1.20 \cdot 10^{-6}$	180.34	$6.34 \cdot 10^{-10}$
H_2O_2	$1.85 \cdot 10^{-6}$	172.68	$3.99 \cdot 10^{-11}$
HCO	$1.18 \cdot 10^{-6}$	177.98	$8.3 \cdot 10^{-10}$
NNH	$1.51 \cdot 10^{-6}$	170.27	$3.49 \cdot 10^{-11}$
N_2O	$1.52 \cdot 10^{-6}$	180.01	$1.53 \cdot 10^{-10}$
$CH_2(s)$	$9.41 \cdot 10^{-7}$	171.20	$1.47 \cdot 10^{-11}$
O_2	$1.80 \cdot 10^{-6}$	173.10	$3.73 \cdot 10^{-11}$
CH_2CHO	$1.22 \cdot 10^{-6}$	177.79	$6.64 \cdot 10^{-10}$
$HNCO$	$1.5 \cdot 10^{-6}$	179.19	$1.52 \cdot 10^{-10}$
$HCCO$	$3.69 \cdot 10^{-6}$	171.83	$2.47 \cdot 10^{-10}$
H_2	$7.37 \cdot 10^{-7}$	170.55	$1.07 \cdot 10^{-11}$
NO_2	$1.91 \cdot 10^{-6}$	176.92	$1.49 \cdot 10^{-10}$
CH_4	$1.037 \cdot 10^{-6}$	171.24	$1.71 \cdot 10^{-11}$
C	$1.28 \cdot 10^{-6}$	170.50	$2.54 \cdot 10^{-11}$
HO_2	$1.82 \cdot 10^{-6}$	172.75	$3.87 \cdot 10^{-11}$
CH_3OH	$1.23 \cdot 10^{-6}$	177.27	$6.83 \cdot 10^{-10}$
C_3H_7	$8.62 \cdot 10^{-7}$	172.27	$9.35 \cdot 10^{-11}$
CH_3OH	$1.23 \cdot 10^{-6}$	181.59	$8.1 \cdot 10^{-10}$
CH_2O	$1.19 \cdot 10^{-6}$	178.04	$8.58 \cdot 10^{-10}$
CO	$1.53 \cdot 10^{-6}$	171.43	$2.87 \cdot 10^{-11}$

Molecule	A_s ($\frac{kg}{ms\sqrt{K}}$)	T_s (K)	Residual
CH_3O	$1.19 \cdot 10^{-6}$	177.31	$6.97 \cdot 10^{-10}$
O	$2.10 \cdot 10^{-6}$	170.61	$6.25 \cdot 10^{-11}$
$HCNN$	$3.69 \cdot 10^{-6}$	171.83	$2.47 \cdot 10^{-10}$
NCO	$1.49 \cdot 10^{-6}$	180.43	$1.45 \cdot 10^{-10}$
CH_2	$9.41 \cdot 10^{-7}$	171.22	$1.47 \cdot 10^{-11}$
$HCNO$	$1.50 \cdot 10^{-6}$	179.19	$1.52 \cdot 10^{-10}$
NH_2	$2.26 \cdot 10^{-6}$	170.62	$7.26 \cdot 10^{-11}$
H_2O	$1.51 \cdot 10^{-6}$	199.76	$3.19 \cdot 10^{-9}$
NH	$2.19 \cdot 10^{-6}$	170.62	$6.80 \cdot 10^{-11}$
H	$8.66 \cdot 10^{-6}$	171.18	$1.27 \cdot 10^{-11}$
AR	$2.09 \cdot 10^{-6}$	172.49	$6.13 \cdot 10^{-11}$
NO	$1.61 \cdot 10^{-6}$	170.62	$3.22 \cdot 10^{-11}$
CH	$1.89 \cdot 10^{-6}$	170.58	$5.09 \cdot 10^{-11}$

Table C.1: Sutherland coefficients